AN EXPERIMENTAL AND ANALYTICAL INVESTIGATION OF DYNAMIC FLOW RESPONSE OF A FAN ROTOR WITH DISTORTED INLET FLOW

by

Jeffrey R. Schwartz

Thesis submitted to the Faculty of the

Virginia Polytechnic Institute and State University

in partial fulfillment of the requirements for the degree of

MASTER OF SCIENCE
in
Mechanical Engineering

APPROVED:

____

W.F. O'Brien, Chairman

__________________ __________________

P. S. King C.L. Dancey

August, 1999

Blacksburg, Virginia

Key Words: Compressor, Dynamic, Modeling, Distortion, Wake, Response, Pressure, Rotor, 'Frequency Response Function'

An Experimental and Analytical Investigation of Dynamic Flow Response of a Fan Rotor with Distorted Inlet Flow

by

Jeffrey R. Schwartz

Committee Chairman: Walter F. O'Brien

Mechanical Engineering

(ABSTRACT)

An experimental and analytical investigation was conducted to gain insight and ultimately predict the dynamic flow response of a fan rotor with inlet flow distortion. Rotor exit total pressure circumferential profiles were accurately predicted using frequency response functions derived from experimental rotor response data. Using these predicted profiles, an initial attempt was made at predicting the dynamic (distorted) stage characteristics of the test machine with promising results.

The first step of this research was an experimental investigation to gather unsteady rotor response data. The steady three-dimensional inlet flow of an isolated rotor subjected to inlet distortion was obtained using a five-hole pneumatic prism probe. Exit flow dynamic wake data were obtained using a piggyback steady/unsteady total pressure probe in non-nulling mode. Inlet and exit data were collected for eighteen different combinations of distortion level, operating point, and measurement span.

Frequency response functions were generated and then averaged for each operating regime, span, and distortion intensity, assuming the data to be stationary and ergodic. These 'generalized' FRF's were used to predict the rotor exit total pressure profile. These pressure profiles were then used in an initial attempt to predict the dynamic stage (distorted) characteristics of the test machine. Best predictions resulted when an FRF was used for individual operating regimes, defined with respect to rotor blade mean aerodynamic loading.

Acknowledgements

I want to thank the members of my advisory committee serving in this capacity. I would like to specially thank Dr. Walter F. O'Brien for his helpful guidance and knowledge. It was his turbomachinery class that spurred my interest in this area of work. I would also like to thank Dr. Peter King for his valuable help around the lab, especially in helping me obtain calibration data for the inlet probe.

Dr. Milt Davis deserves thanks for funding this project through Arnold Engineering Development Center (AEDC).

A very special thanks goes to Shaun Boller. He was always willing to help me throughout this investigation; he even devoted a couple of days, on his own time, to help me get this project started. His generosity and previous hard work have saved me a tremendous amount of time in both the data collection and report preparation of this project. I would have never been able to finish this project in such a timely manner without his help.

I would also like to thank Joe Howard for his help toward the latter stages of this project. I would like to thank Dave Donaldson, Wayne Sexton, and Drew Zima for their help. I would like to thank fellow turbo-lab members Scott Gallimore, Mac Chiu, and Maj. Keith Boyer (USAF) for their friendship.

I would like to thank all of my friends, especially John, Marko, Kevin, Scott, and my girlfriend, Jocelyn. They made my graduate school experience a very enjoyable one. A very special thanks goes to my parents. Their emphasis on education and learning from day one, has allowed me to be where I am today. They always have and always will support me in whatever I do in life.

Table of Contents

List of Figures

Nomenclature

AOA	angle of attack
C	chord length
FF	forcing function
RF	response function
FRF	frequency response function
h	specific enthalpy
i	incidence angle
M	magnitude
Φ	phase
$\dot{m}$	mass flow rate
A	area
A	amperes
mA	milli-amperes
U	blade velocity
V	absolute flow velocity
C_z, V_z	axial flow velocity
W	relative flow velocity
α	absolute flow angle
β	relative flow angle
β'	blade metal angle
ρ	fluid density
ξ	stagger angle
θ'	camber angle
η	efficiency
w_c	compressor work
τ	torque
AC	alternating current
DC	direct current
FM	frequency modulation

Subscripts

θ	circumferential direction
m	meridional
1	rotor inlet
2	rotor exit
t	total (pressure)
ann	annulus
atm	atmospheric
ave	average

dB	decibels
Hp	horsepower
H_2O	water
I/O	input/output
IGV	inlet guide vanes
d	wire diameter
m	meters
cm	centimeters
ft	feet
P	pressure
R	ideal gas constant
rpm	revolutions per minute
t	blade thickness
t	time
T	temperature
W	uncertainty
PSD	power spectral density
psig	pounds per square inch gauge pressure
ψ	non-dimensional pressure rise coefficient
Ω	Ohms
θ^-	circumferential extent of distortion
θ	tangential (circumferential) angle
Hz	Hertz
FFT	Fast Fourier Transform
OP	Operating Point

1 Introduction

Compressor design and performance prediction is currently based largely on steady-state theory and experimental tests. However, in reality, compressors are subjected to many non-uniform and dynamic inlet flows. These non-uniformities may originate from a number of sources including: extreme aircraft maneuvers, stealthy inlet configurations, atmospheric turbulence, and/or wakes from other aircraft (and the aircraft itself). The local flow within a machine that is subjected to these inlet distortions is not steady, and the overall performance is generally reduced. Therefore, there has been an increasing interest in the dynamics of a compressor's performance. Improved models capable of simulating these unsteady flows are needed to aid in the design of compressors. A good model can save valuable time and money in the development of a new compressor design.

Inlet distortion can have many detrimental effects including: compressor performance loss, unsteady blade forces, vibration, and losses in stall margin. Stall margin is usually defined as the difference between the pressure ratios at stall and at a particular operating point, divided by the pressure ratio at that operating point. Figure 1.1 illustrates the effects of inlet distortion on a compressor performance map.

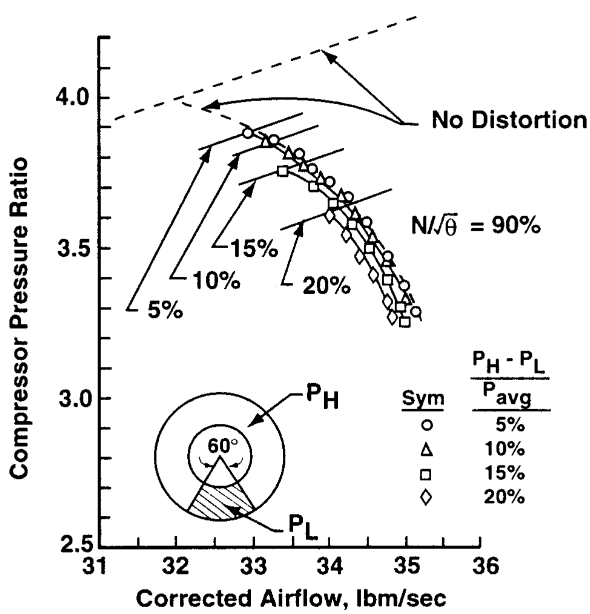

Figure 1.1: Distortion Effects on Compressor Performance Map (Kimzey, 1977)

As the intensity of the distortion increases, the loss in performance increases. This is shown as a shift in the speed lines to a lower pressure rise and corrected rotor speed.

This investigation focuses on analyzing and predicting the flow response of a fan rotor to inlet flow distortions, with the ultimate goal of successfully predicting dynamic stage characteristics. A series of data sets were collected from a single, isolated rotor that was subjected to total pressure inlet distortion by way of 'classical' mesh screens. It was assumed that the resulting wake time response data was very similar to the airfoil lift (pressure rise) response. Generalized frequency response functions, based on the data, were used to predict rotor exit total pressure circumferential profiles. These predicted profiles were then used in an initial attempt in predicting the dynamic (distorted) stage characteristics of a compressor such as that shown in Figure 1.1.

The experimental data, analysis, and the proposed prediction method are presented in the following sections of this document.

2 Literature Review

Since the present work is a combination and direct extension of both the Boller (1998) and Howard (1999) studies, the current literature review is primarily a restatement of these previous literature reviews. However, this review will extend further into the development of the critical angle of distortion theory.

2.1 Review of Experimental Studies

The literature pertaining to experimental studies is limited here to steady-state circumferential pressure distortion in axial-flow fans and compressors due to the vast number of documents associated with experimental research into improving compressor response to distorted inlet flows.

2.1.1 Pressure Distortion Simulation Techniques

The two major forms of pressure distortion are circumferential and radial with respect to the machine axis as shown below in Figure 2.1.

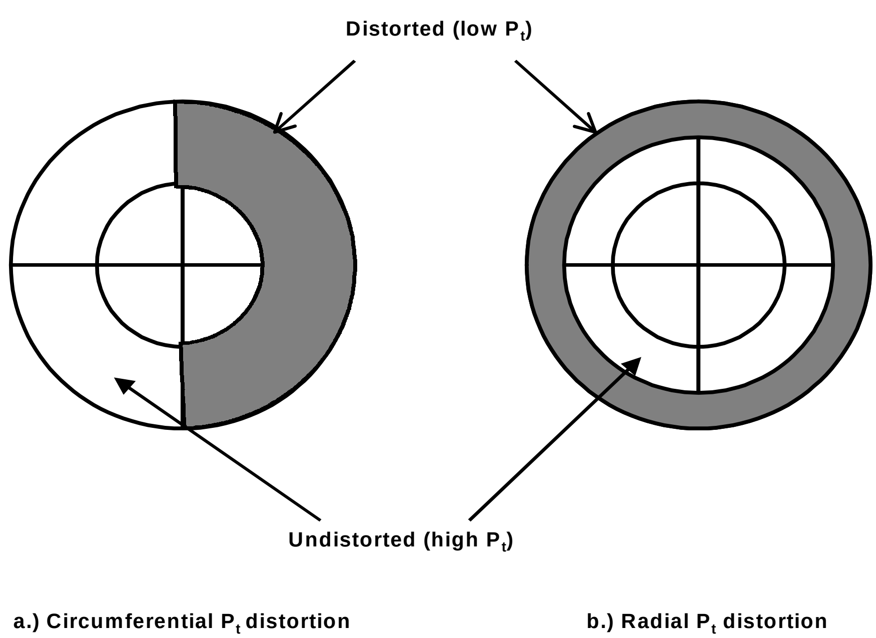

Figure 2.1: Circumferential and Radial Distortion Patterns (Boller, 1998)

Circumferential distortions have a greater effect on the performance of a machine since the resulting disturbance is normal to the airfoil motion, thus having a greater effect on angle of attack and stall margin.

Screens are the 'classical' method for imposing steady-state total pressure distortions on fans and compressors due to their simplicity and cost-effectiveness. These screens produce a viscous static pressure drop across the screen mesh while deflecting the streamlines of the flow toward the outer edges of the screen-induced distorted region (McCarthy, 1964).

Ideally these distortion screens will produce a 'square wave' pressure profile. However, in reality, there are transition regions at the edges of the screen. This is due to the upstream fluid communication between the rotor and the screen. Therefore, the distorted pressure profile that the rotor sees is not a complete 'square wave', but rather a continuous variation in pressure as the blade passes downstream of the screen. This is especially true for lower speed machines since the slower flow allows more time for this upstream 'communication' to occur.

To characterize a steady circumferential total pressure inlet distortion, three basic parameters are used: (1) the circumferential extent (θ^{-}), (2) the distortion intensity (level) or magnitude of total pressure loss (sometimes represented as a percentage of maximum variation in pressure in the circumferential direction as caused by the screen), and (3) the number of distortions (multiples) per revolution of the rotor (i.e. 4/rev). These three descriptors are defined in the Society of Automotive Engineers document ARP 1420 issued in 1978.

2.1.2 Distortion and Wake Testing in Axial Flow Fans and Compressors

Many studies have been conducted in both the stationary and relative frames to investigate how fluid flow through a fan or compressor varies due to circumferential total pressure inlet distortion. Boller (1998) divided these into five categories: (1) papers concerning inlet flow condition and blade lift response to distortion, (2) papers concerning blade response to a transient blade incidence angle above the steady-state stalling angle, (3) wake analysis with respect to variations in incidence angle or operating point on the performance map, (4) papers discussing the phenomena of a suction side total pressure profile appearing as a jet or pressure excess in the stationary frame of reference, and finally (5) one paper discussing the effect of inlet total pressure distortion on inlet flow conditions and three-dimensional wake response.

As previously stated, a number of fan and compressor studies have been performed with regard to variations in inlet flow conditions due to distortion. Soeder and Bobula (1979) investigated the effect of steady circumferential total pressure distortion on flow characteristics entering an aircraft engine using classical screens. They found that for a transonic turbofan engine, maximum and minimum flow yaw angles in the absolute frame occurred within the constant intensity distortion sector of the flowfield rather than at the screen edges. They also found the yaw angle is usually the largest in the hub region for the screen configurations they tested. This yaw angle variation increased in magnitude as the flow approached the engine inlet. Increasing the screen blockage increased the yaw angle variation. They also discovered that the inlet pitch angle variation in the plane of the distortion is much smaller than the yaw angle variation, as would be expected for purely circumferential distortions.

Cousins (1979) analyzed the unsteady blade surface pressures due to circumferential inlet total pressure distortion in a low-speed axial-flow compressor rig using on-rotor pressure transducers and a telemetry system. Stationary high-response probes were employed to capture wake pressure variations during rotating stall. He showed that it was feasible to develop a frequency domain function describing the dynamic blade response using data from on-rotor pressure measurements and Fourier transform techniques.

Gauden (1977) investigated the performance and stalling behavior of a low-speed axial-flow compressor subjected to three different circumferential inlet distortion levels. He used steady-state instrumentation in the stationary frame of reference and high-response pressure transducers mounted on the blades. He discovered that distortion screens reduced the mass flow rate through the compressor due to their low porosity and precipitated stall at a more open throttle valve setting than for undistorted operation.

Gauden found that with respect to the direction of rotor motion, a sharp increase in axial velocity was observed as the distorted segment was approached, implying a decreased angle of attack at the blade leading edge. This was due to flow blockage created by the distortion screens. As the blades passed circumferentially through the distorted flow region behind the screens, the axial velocity was reduced until the angle of attack was maximized, and then returned to its undistorted value at the trailing edge of the screen. The shape of the circumferential velocity profile remained roughly the same as the flow rate was decreased using a throttle valve.

Dancy (1976) tested the performance and stalling behavior of a low-speed axial-flow compressor with circumferential inlet flow distortion. Similar to the results of Gauden for the same test rig, he discovered that the axial velocity increased nearly 10 % as the leading edge of the screen was approached, then fell off sharply and leveled out. An opposite effect occurred at the trailing edge of the screen with respect to rotor rotation. He found that velocities in the undistorted segments of a partially-distorted inlet were higher than the constant flow velocity for a clean inlet. Although the compressor was set to produce the same volumetric flow rate in both cases, the flow rate increase in the undistorted region was insufficient to return the compressor to its original, undistorted volumetric flow rate. As a result, the undistorted compressor always had a higher flow rate. As the back pressure was increased, the flow rates for the distorted and undistorted compressors approached the same value due to a decreased axial velocity and, subsequently, a decreased total pressure drop across the screen. He also found rotating stall to originate at the hub of the RAF-6 airfoils (blades) of the test machine.

The second literature category is blade response to an unsteady incidence that exceeds the steady-state stalling angle. Sexton (1980) investigated the dynamic stalling characteristics of low-speed axial-flow compressor blades using blade-mounted transducers and a multi-channel radio telemetry system. High incidence angles and stalling were induced using a distortion screen mounted in front of the IGV. This screen had a sufficiently low porosity mesh to insure incidence angles greater than the steady-state stalling angle. This allowed separation of the blade boundary layer behind the distorted region and reattachment in the undistorted region during each revolution. Sexton then developed a transfer function between the quasi-steady total pressure loss forcing function and the dynamic pressure loss response function. This transfer function in turn described the dynamic response of the rotor blade row flow and made possible the prediction of response to a given inlet distortion for a rotating stall model.

Neal (1975) used a multi-channel FM telemetry system in conjunction with miniature blade-mounted transducers to investigate low-speed rotor blade lift response due to circumferential inlet flow distortions. He found that normalized lift for an undistorted compressor decreases as the volumetric flow rate is decreased and angle of attack is correspondingly increased. He explained this unusual behavior by noting that although the coefficient of lift increases with an increase in angle of attack, the decrease in volumetric flow rate causes a decrease in absolute lift. The normalized lift of the distorted compressor first increased and then decreased as flow rate was decreased. He explained this as being due to competing effects of changes in angle of attack, changes in volumetric flow rate, and changes in the level of distortion as the back pressure was increased by closing a downstream discharge valve. He presented an analysis of rotor blade lift and rotor inlet dynamic pressure for a rotor cycle during which the blade experienced a far greater incidence than the steady-state stalling angle.

Neal found that although the blade did eventually stall as it passed well into a distortion, the delay in the inception of stall was significant, with partial stalling of the instrumented rotor blade just prior to the blade's exit from the distorted region. This corresponded closely to the highest angle of attack on the rotor blade during the rotor cycle. The dynamic stall event was typically characterized by a lift overshoot, which then collapsed and returned to the undistorted lift value after passing the trailing edge of the screen. This indicated boundary layer reattachment. The phenomenon of a blade experiencing an incidence angle beyond the steady-state stalling angle without stalling was also observed by Melick (1973) and Henderson and Horlock (1972), and was postulated to be a function of the rotor blade lift response.

The third literature category centers on wake analysis with respect to variations in incidence or operating point on the map. The wake of a rotor blade may be defined as the downstream region of pressure and momentum defect due to boundary layer separation in an adverse pressure gradient (Fox and McDonald, 1992). In addition, in viscous flows over a body a wake exists even if the flow is not separated or has a favorable pressure gradient. The wake defect may be defined as the difference between the local velocity in the wake and the freestream velocity between the blade passages. The near wake is the region where the defect is of the same order of magnitude as the freestream velocity and the far wake is defined as where the defect is an order of magnitude less than the freestream mean velocity (Reynolds and Lakshminarayana, 1979).

Lakshminarayana, et al. (1981) studied the effects of rotation and blade incidence on the properties of a low-speed fan rotor wake. They defined a wake semi-width at half the depth on both the pressure and suction sides of the wake and non-dimensionalized them by the rotor blade spacing in the circumferential direction. They found that the wake defect was reduced as rotor rotational speed increased and that the axial velocity wake defect was highest at the hub. Higher rotor speed gave lower axial velocity defect, and higher loading increased the axial velocity defect (or decreased the downstream decay rate of the axial velocity defect). The wake semi-width at a fixed loading did not change with an increase in rotor rotational speed. In addition, they found that wake semi-width was lower at lower loading and the growth was less rapid.

Shreeve and Neuhoff (1984) found the wake of a small, transonic single-stage axial compressor to broaden at reduced throttle settings and increased blade speed. Henderson and Shen (1981) investigated the influence of unsteady rotor response on a distorted flow field in a low speed axial flow rotor. They found that as the rotor was loaded by decreasing the flow coefficient, the boundary layer thickness, wake defect magnitude, and wake width all increased.

Reynolds, et al. (1978) found the wake of an isolated low-speed rotor to be three-dimensional in nature with an appreciable radial velocity due to an imbalance in the radial pressure gradient and centrifugal forces. They defined wake semi-widths on the rotor pressure and suction surfaces to obtain a width parameter which was non-dimensionalized by blade spacing.

Ravindranath and Lakshminarayana (1980) performed an experimental study of the three-dimensional characteristics of the mean relative frame velocity in the wake of a moderately loaded compressor rotor blade. They defined a non-dimensional semi-width parameter as the sum of the characteristic widths on the pressure and suction surfaces normalized by the semi-blade spacing. They found the effect of blade loading was to sustain the wake asymmetry to a much larger extent downstream of the blade trailing edge. Increased loading also increased the velocity defect magnitude, slowed the decay rate, and induced higher radial velocities. They found the wake width to vary considerably in the radial direction. The width increased towards the hub- and annulus-walls, which was attributed to the complex interaction of the wake, hub-, or annulus-wall boundary layers, and secondary flows (tip vortex in the case of the annulus-wall). They found the static pressure to vary across the wake as well as in the wake near the blade trailing edge due to inviscid effects, which is not reflected in total pressure plots. The static pressure was highest at the center of the wake. They compared the variation of the first two Fourier coefficients of velocity with downstream distance and studied the averaged Fourier coefficients and scatter of the harmonic content in the rotor wake.

Reynolds and Lakshminarayana (1979) studied the three-dimensional relative flow characteristics of a lightly loaded low-speed rotor wake. They found that increased loading slowed the decay rates of the axial and tangential mean velocity components and radial velocities in the wake. They found that wake width increased with loading, and that only in the far wake was it acceptable to assume a negligible static pressure variation. Also, the axial and tangential components of mean velocity were highly asymmetric about the wake centerline, a trait which was more pronounced for increased loading. They found the wake width to increase with radial position about mid-radius and speculated that this may have resulted from large radial transport of mass, momentum, and energy.

Muhlemann (1946) performed experiments that showed strong radial variation of the wake with the largest mean velocity defects and wake widths near the hub and tip regions. He also found a more rapid decay of wake width as blade loading was increased, a result verified by Ufer (1968).

Kerrebrock, et al. (1974) found considerable randomness in absolute exit flow angle at several radii in the wake of a blowdown transonic rotor, even when wake pressure and velocity profiles were quite sharp. They suggested the source of time dependence as random effects from the hub and tip regions influencing the entire blade span.

The fourth category contains discussions of the phenomena of the suction side (of the blade) total pressure profile appearing as a jet, or pressure excess, in the wake. Shreeve, et al. (1978, 1978) found impact pressures to be a jet on the suction side of the blades in the wake of a transonic rotor. Shreeve and Neuhoff (1984) found the absolute velocity in the wake of a transonic rotor to have a larger magnitude on the suction side of the blades, a phenomena which was more evident at the hub where blade and flow velocities were subsonic. Schmidt and Okiishi (1977) found a higher axial velocity downstream of the suction side of the blade when measured in the stationary frame, a phenomena which was, again, more pronounced at the hub region. Lakshminarayana, et al. (1981) found the axial velocity to be higher on the suction side of the wake of a low-speed fan rotor blade when measured in the stationary frame of reference. Ravindrath and Lakshminarayana (1980) found higher total relative velocity and stagnation pressure profiles downstream of the suction side of a low-speed rotor blade, indicating that the phenomena of a suction side jet is not limited to stationary measurements. Ng and Epstein (1985) also discovered the presence of a suction side jet during total pressure measurements in the wake of an axial-flow transonic fan.

Cherrett and Bryce (1995) studied the unsteady three-dimensional exit flow fields in the stationary frame of a single-stage transonic fan, comparing random stagnation pressure unsteadiness to ensemble-averaged stagnation pressure unsteadiness. They found that in the stationary frame it is possible for stagnation pressures to be higher on the suction, rather than the pressure, surface side of the passage, and for a wake in the relative frame to appear as a jet (pressure excess) in the stationary frame. In the wake region, the stagnation pressure rose rapidly from a pressure trough on the pressure surface side of the rotor wake, to a pressure peak on the suction surface side of the wake. The magnitude of the suction side peak relative to the mean level was two to three times that of the pressure trough. The point in the wake region where the stagnation pressure rose above time-averaged values corresponded approximately to the position of maximum random unsteadiness. A second stagnation pressure trough occurred on the suction surface side of the wake followed by a peak comparable to the strength of that attained within the suction surface side of the rotor wake. Wake unsteadiness was found to be three to four times that elsewhere in the blade passage, with peak unsteadiness at mid-pitch. Ensemble-averaged wake stagnation pressures indicated little change in amplitude with increased compressor loading at the same speed, with the exception of the lower blade spans toward the hub where rotor inlet Mach numbers approached unity.

The fifth category is limited to one paper discussing the effect of inlet total pressure distortion on blade inlet flow conditions and three-dimensional wake response. Colpin and Kool (1978) studied the propagation of a non-uniform upstream flow field through a low-speed axial-flow compressor stage rotor. Circumferential total pressure distortion was created using a grid which was rotatable with respect to the stationary instrumentation. They found that the distortion was indicated more strongly in flow angles than velocities downstream of the rotor. They found that as a blade passed into a distortion the boundary layer on the suction side thickened due to the increase in loading. Moving further into the distorted region, the axial velocity outside of the wake increased due to increasing blockage caused by the wake. A strong reduction in the relative outlet flow angle corresponded to stronger centrifugation, or radial flow, in the blade wakes. Moving further still into the distorted region, the blade wake reached its maximum thickness indicating boundary layer separation on the suction side while the freestream axial velocity mean value increased to compensate for the additional boundary layer blockage. When reaching the distortion trailing edge, the boundary layer on the blades tended to reattach, inducing a thinner wake. After the blade passed through the distorted region, the investigators noted a reduction in wake circumferential extent and depth, as well as a slight increase in axial velocity. Colpin and Kool also noted that the flow turbulence increased at the inlet and exit of the rotor while in the distorted region. As the suction side boundary layer separated, the turbulence level suddenly grew due to the development of a large wake.

It is interesting to note that Colpin and Kool also experienced incidence angles greater than the quasi-steady stall value. A strong decrease in wake dynamic pressure corresponding to the maximum incidence angle reinforced the observation of blade dynamic stall. The increase in inlet relative flow angle did not induce an immediate growth of the boundary layers, implying that a time lag is introduced into the boundary layer response as shown by Mazzaway (1975), Carta (1972), and Hetherington and Moritz (1975).

The limitations of the Colpin and Kool experiment with respect to the present investigation are that data was only taken at mid-span for one distortion screen and one operating point. The rotor blade row also had adjacent IGV and stator rows, and the probes were located too far from the rotor, allowing a significant circumferential flow redistribution between the probes and the blade row.

2.2 Review of Modeling Studies

Tests and experiments, such as those discussed above, are quite costly to engine companies and should be avoided when possible. The only way to avoid testing is to use a good model to predict analytically what will occur realistically. Therefore, predicting the compressor or fan response to steady and unsteady inlet distortions is of great interest to the engine community. It is much more economical to run a computer model to determine how a new compressor design will perform rather than 'bend the metal' and then find out that the design needs to be altered.

A number of documents exist that deal with analytical models created to predict the dynamic response of compressors and fans. To date, these models have been based on empirical data, steady-state performance characteristics, and first-order response functions to account for the dynamic departure from steady-state operation. Most of these models incorporate first principles and compressor geometry as well. Unfortunately, these models must be calibrated to each different compressor design in order to duplicate experimental results.

One of the most widely used concepts in distortion modeling is the parallel compressor theory. This is a simple model that can be used to predict pressure losses due to circumferential distortions, and was developed by Pearson and McKenzie (1959). The theory uses the assumptions as described by Braithwaite, Graber, and Mehalic (1973):

1. the distorted compressor (to be modeled) is assumed to consist of two or more independently operating sub-compressors,
2. all of the sub-compressors have individually uniform inlet conditions and they all operate on the undistorted compressor performance characteristic,
3. no circumferential cross-flow occurs between the isolated compressors,
4. the exit static pressures of all sub-compressors are identical, and
5. the entire compressor is assumed to stall when the pressure rise across any sub-compressor equals that of the undistorted compressor stall pressure ratio.

In using this method, the response of the original compressor to inlet distortions is assumed to be instantaneous, or quasi-steady, since the parallel compressors have uniform flow at the inlet. Figure 2.2 shows a visual representation of parallel compressor theory.

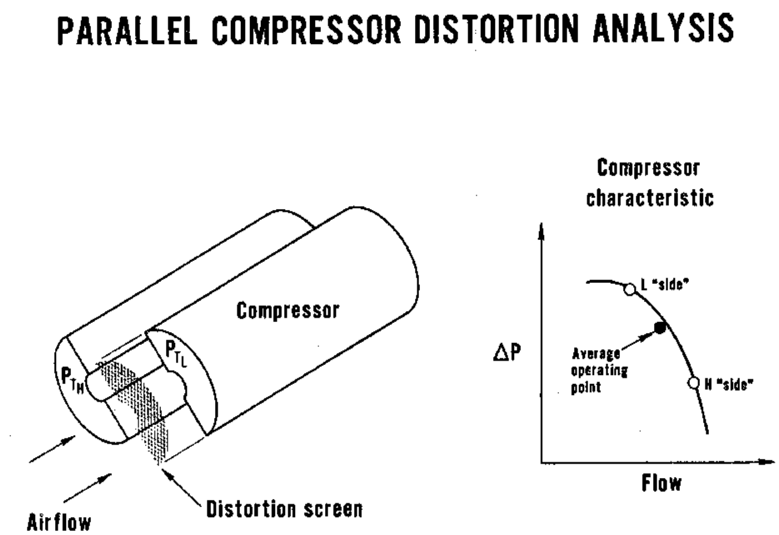

Figure 2.2: Parallel Compressor

Reid (1969) showed that the instantaneous compressor response modeled by parallel compressor code is highly inaccurate for small extent distortions. He developed the idea of a critical angle of distortion extent, which is the smallest circumferential distortion angle at which the quasi-steady assumption is accurate. (The critical angle theory will be discussed in greater detail later in the literature review.) Reid incorporated the critical angle idea into parallel compressor code, which improved its accuracy for small extent distortions. This was the first step in improving dynamic response models.

Roberts, Plourde, and Smakula (1968) took the next step when they investigated the effects of chord length of both the rotor and stator on a low speed, multistage, axial flow compressor. They correctly concluded that chord length was highly correlated to how quickly the blade responds to a circumferential distortion, in this case a 180° distortion screen. They compared experimental data to parallel compressor code results and found that as the blade length was increased the model's inaccuracy increased. They reasoned that the flow along a long chord length takes more time to adjust to the distortion. They also defined a parameter called reduced frequency. Reduced frequency was defined as a measure of the chord length to the wavelength of the unsteady disturbance, as follows:

$$k = \frac{B \cdot \Omega}{V} \qquad \textbf{Equation 2.1}$$

where

k= reduced frequency

V= average velocity of the air relative to the rotor

B= one half of the rotor chord length

Ω= Frequency of the circumferential disturbance with a window of periodicity of one revolution (rad/sec)

Mikolajczak and Pfeffer (1974) expanded the reduced frequency parameter. This representation showed that the reduced frequency is the ratio of the time a particle spends in the blade passage to the time it takes for the blade to rotate through the distorted region.

$$k = \frac{b}{r} \cdot \frac{360}{\theta} \cdot \frac{U}{Vm}$$

Equation 2.2

where

b= axial projection of the rotor chord

r= compressor radius at the blade section

θ= distortion extent in degrees

U= tangential blade speed

V_m=axial air velocity

Cousins (1997) also discussed reduced frequency and the time an axial or centrifugal compressor takes to respond to an inlet distortion. Cousins examined transonic axial and centrifugal compressors. He noted that much of the diffusion in a transonic axial blade occurs after the first 35% of the meridional distance of the blade is reached. He noted that there is a time response associated with how long it takes a blade to respond to a change in the fluid particle flow. This time response (fluid particle transport time) can be calculated by dividing the distance traveled to the throat of the passage by the relative velocity. If the fluid particle transport time is less than the time it takes for the blade to pass through the distortion, the blade response will be at a maximum. If it is greater, the blade will not fully respond. The response time of a centrifugal rotor is different because of the way the blades create a pressure rise. Cousins stated that once the fluid particle reaches the throat of an axial blade there is a chance the flow could be disrupted causing separation, and the blade could respond more quickly then if the flow did not separate. While in a centrifugal compressor the fluid particle must travel past the throat and further into the rotor before the disruption could affect the radial flow component. Centrifugal compressors have a higher reduced frequency parameter because of longer meridional distances and hence a higher tolerance to inlet distortions.

Mazzawy (1977) developed a non-linear, compressible flow model that uses the parallel compressor method without assuming a constant exit pressure. The model considers individual blade row performance to account for stage matching effects and also uses an empirical correlation to account for some circumferential cross-flow. Therefore, the model requires the determination of blade row characteristics as a function of upstream conditions. Since the dynamic pressure loss and fluid path exit angles differ from the quasi-steady values, Mazzawy incorporates a first order response function to lag the time response. His time constant was based on empirical data that was descriptive of boundary layer response.

Tesch and Steenken (1981) developed a Dynamic Digital Blade Row Compressor System Stability Model for the General Electric Company. The model was a 1-D, pitch line, row by row model using equations of conservation in a volume-averaging form. They used a time marching scheme to model the dynamic response of the compressor row. They also developed an effective incidence angle that was developed by assuming a first order time response. They defined the effective incidence angle as “the incidence angle which is equivalent to the dynamic response of the blade as it passes through the distortion.” The purpose of this effective incidence angle is to characterize the response lag of a blade to an inlet distortion. They used this angle to calculate the dynamic blade characteristic through time instead of the instantaneous incidence angle. Basically, this effective incidence angle is modeling the fluid particle transport time through the blade passage.

Adamczyk (1974) continued to further unsteady dynamic compressor rotor response by developing a new compressor code. His model predicts circumferential distortions with a method similar to parallel compressor theory, but is more advanced because it does not assume constant exit static pressure between regions. This allows for the exit static pressure fluctuations that occur in real machines. It is also more advanced than linear perturbation theory-based models because it is not restricted to small perturbations. Linear perturbation cannot account for degradation in the stability-operating limit because it is restricted to small amplitude distortions. His model divides the flow into two regions: flow in the blade passages, and flow upstream and downstream of the rotor. The flow in the blade passages is based on the time-dependent mechanical energy equation and includes the effects of cascade loss and turning. The flow upstream and downstream is modeled as non-linear, 2-D, time dependent flow fields. Even though the flow field calculations and base assumptions are more advanced, Adamczyk still uses first order lag functions to calculate the blade row dynamic response.

Melick and Simpkin (1972) developed a global dynamic compressor model that related inlet total pressure and temperature distortions to losses in stall margin. They derived an effective angle of attack which was based on a first-order response function. The time constant they used for this equation was proportional to blade chord length. They also arrived at the conclusion that stall and recovery responses are different phenomena and have different response functions. They were able to predict loss in stall margin as a function of the distortion intensity and the reduced frequency parameter. Melick (1973) later improved the accuracy of the model by using a second order response function in deriving the effective angle of attack. He determined the two time constants from experimental test data.

Work has also been done on developing models that will predict the rotating stall characteristic of a compressor. These works have been reviewed by Mokelke (1974). Early models used linearized equations of motion and were therefore only accurate for small perturbations. The compressor stages were modeled as semi-actuator disks where work and rotation are added instantaneously. Nagano and Takata (1970) expanded on these models by using non-linear equations of motion. They also used first order response functions to model the unsteady characteristic.

Sexton (1980) furthered the work of Nagano and Takata in his model. He modeled the blade response using frequency response functions derived from experimental data. He used instrumented blades to measure the dynamic pressure forces.

He then derived the frequency response function between the quasi-steady and the dynamic total pressure loss distributions. The quasi-steady total pressure loss was the forcing function while the dynamic total pressure loss was the response function. This use of a frequency response function has higher accuracy than a simple first order response function. This response function was only developed for rotating stall, however, and not the pre-stall region of operation. In addition, this work only dealt with one blade design and chord length.

Cousins and O'Brien (1985) developed a post-stall model using the experimentally determined dynamic loss response function described by Sexton and O'Brien (1980). This new model interactively coupled the upstream and downstream fields with a semi-actuator disk, which represents the compressor rotor. The dynamic loss response is calculated by determining the quasi-steady variations in total pressure loss and multiplying it by a transfer function based on on-blade experimental measurements. This model is capable of defining a compressor characteristic map with pre-stall and post-stall operating lines.

2.2.1 Critical Angle Theory

As mentioned, Reid (1969) developed the idea of a critical angle of distortion to account for the fact that the parallel compressor theory is highly inaccurate for small extents of distortion. If the extent of the distortion screen is less than the critical angle, the compressor row does not respond to the distortion in a quasi-steady manner. He describes the critical angle as 'the minimum area of spoiling which will induce the maximum loss of surge pressure ratio.' Figure 2.3 shows this graphically.

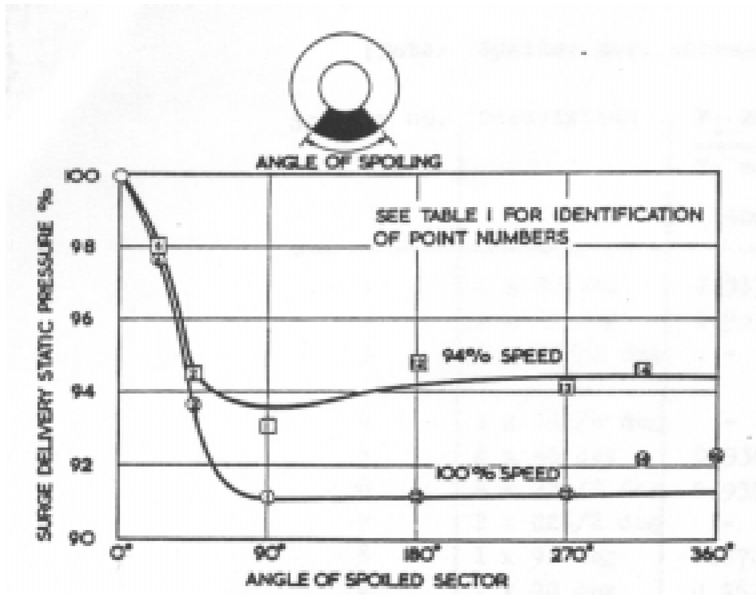

Figure 2.3: Critical Angle Theory (Reid, 1969)

Reid stated that the critical angle is usually in the range of 60° to 90°; critical angles of 60° have been obtained by others including Reid (1969), Gauden (1977), and Calogeras, Mehalic, and Burstadt (1971) on three different compressors. However, the critical angle of a particular compressor often depends on the compressor geometry.

Reid also showed that dividing a distorted region into smaller regions (all adding up to the same total angle of distortion) has a less detrimental effect on the compressor surge margin. Figure 2.4 shows this concept graphically.

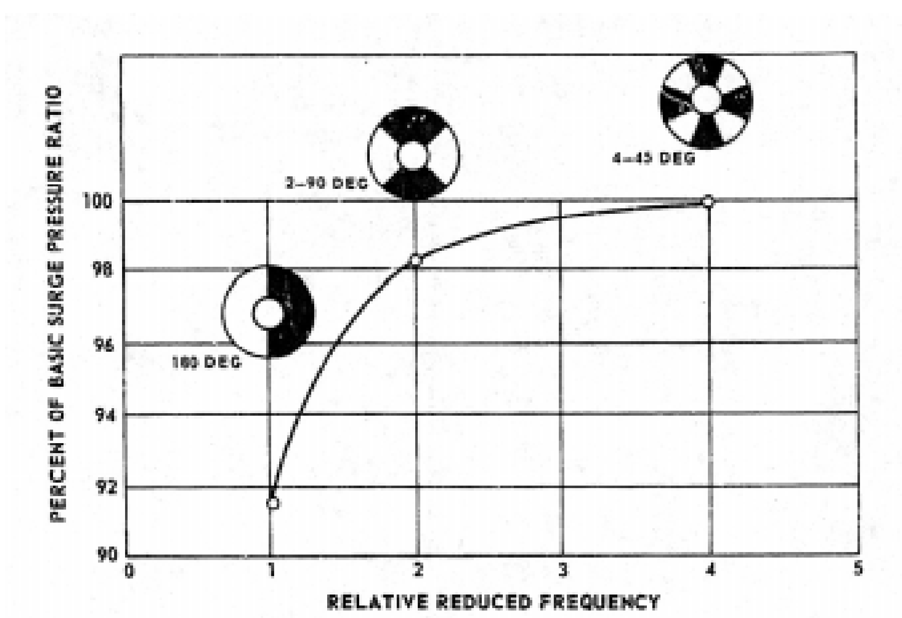

Figure 2.4: Effect of Dividing the Distorted Region (Carta, 1972)

Therefore, it is possible that a two-per-rev 40° (80° total) circumferential distortion can have less effect on a compressor than a single-per-rev 60° distortion since the rotor will not have time to fully respond to distortions smaller than the critical angle. It was also discovered by Reid that at the critical angle, the surge margin was directly proportional to the index, $\Delta P_{inlet}/P_{inlet\ avg}$.

Gauden (1977) showed that for his particular test rig, the intensity of the distortion does not effect the critical angle value. He obtained a critical angle of 60° for three different screen intensities.

The critical angle theory is related to the response time that Cousins (1997) discussed. Figure 2.5 shows visually what was stated earlier about Cousins' fluid particle transport time.

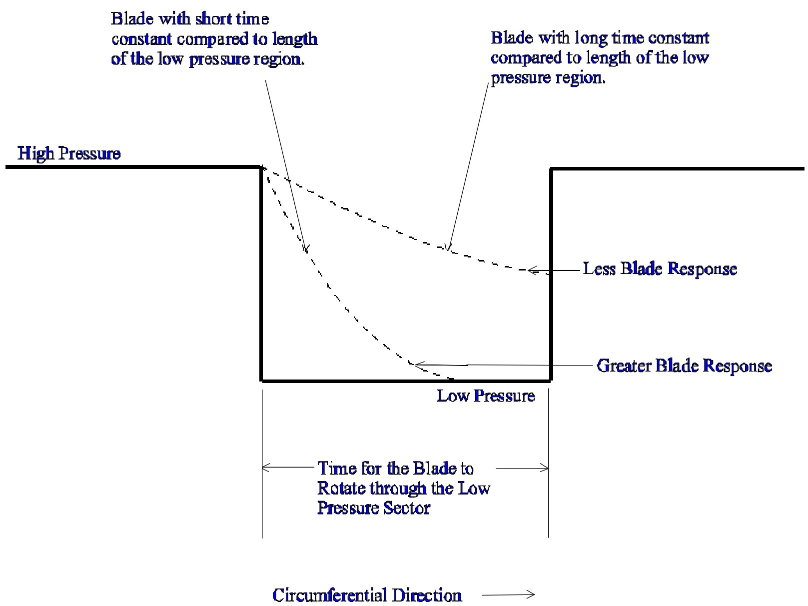

Figure 2.5: Blade Response Based on Fluid Transport Time (Howard, 1999)

The critical angle of distortion corresponds to the critical 'dwell' time where the rotor is behind the distortion for just enough time to see the 'low pressure' region of Figure 2.5. The response of a blade exposed to a critical angle of distortion would pass through the bottom right corner of the square wave pressure profile of Figure 2.5.

2.3 Conclusions from Literature Review

With the exception of Boller's (1998) experiments, there is a lack of fundamental wake data where an isolated rotor experiences dynamic distortion. Another comprehensive study of the dynamic wake response for a variety of intensities, operating points, and measurement spans is needed. In addition, there is a need for an improved method for modeling dynamic compressor behavior.

The following sections present some background in compressor analysis, the experimental setup, and data acquisition. The new data and relevant trends are presented and then compared to that of the Boller work. Then the results of the FRF analysis and compressor characteristic prediction are discussed, as well as conclusions and recommendations.

3 Steady-State Compressor Analysis

The objective of this section is to describe steady-state compressor analysis and to establish terminology, definitions, notation, and sign convention. Yocum (1988) described the following convention for use in two-dimensional linear cascade analysis.

3.1 Two-dimensional Compressor Convention

Figure 3.1 illustrates the absolute and relative flow velocities in the analysis.

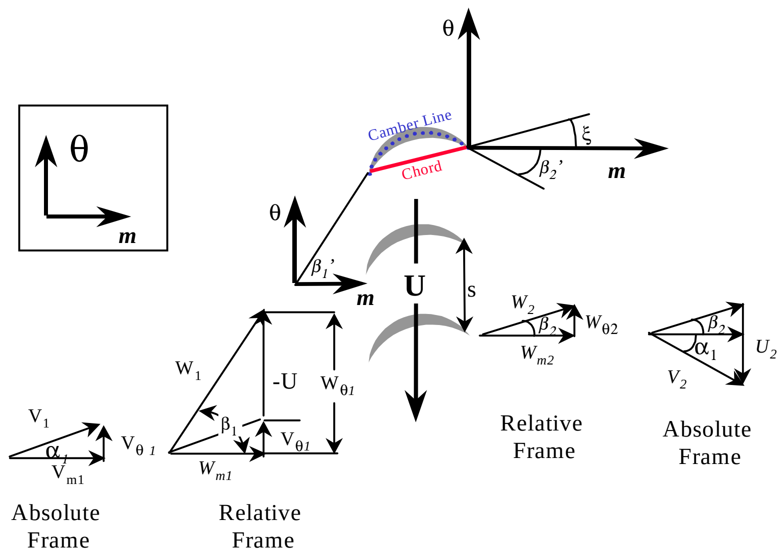

Figure 3.1: Axial-flow Compressor Cascade Geometry and Velocity Triangles (Boller, 1998)

As the blades are rotating with velocity U in the $-\theta$ direction, it is useful to view the fluid velocity from the perspective of a cascade blade in order to simplify blade row performance evaluation. This is known as the relative frame of reference, as opposed to the absolute frame. The data collected in this study were obtained in the absolute frame of reference with respect to laboratory coordinates.

The absolute velocities and flow angles are expressed as V_i and α_i, respectively, and the relative velocities and flow angles are expressed as W_i and β_i, respectively. To relate absolute to relative reference frames and vice versa, the vector addition shown in Equation 3.1 is used.

$$W = \overline{V} - \overline{U} \qquad \textbf{Equation 3.1}$$

Other important terms include the camber line. This is the line representing the mid-point of the blade between its pressure and suction sides at every point along the airfoil. The length of the camber line is often referred to as the camber length. The chord line is the straight line connecting the leading edge to the trailing edge of the airfoil. The blade metal angles β'_1 and β'_2 are those between the meridional axis (m) and the line tangent to the camber line at the blade leading and trailing edges, respectively. The angle formed between the chord line and the meridional axis is referred to as the stagger angle (ξ). It is important to note that the flow angles are not always equal to the metal angles especially at the leading edge. From these definitions, some other important angles are derived.

$$i = \beta_1 - \beta'_1 \qquad \textbf{Equation 3.2}$$

$$\alpha = \beta_1 - \xi \qquad \textbf{Equation 3.3}$$

$$\theta' = \beta'_1 - \beta'_2 \qquad \textbf{Equation 3.4}$$

Equation 3.2 is the incidence angle representing the difference between the actual flow angle and the metal angle at the leading edge of the airfoil. Angle of attack, α, is the angle between the relative velocity, W_1, and the chord line as shown in Equation 3.3. Equation 3.4 determines the camber angle, θ', which is the ideal amount of turning a cascade would impose on a flow if the flow entered tangent to the camber line (Boller, 1998).

3.2 Steady-State Compressor Performance Analysis

Compressors put work into a flow to ultimately create a desired pressure rise. An axial compressor accomplishes this by turning the flow in the tangential direction (θ) in the blade passages. The rotor increases the angular momentum by increasing the tangential component of the absolute velocity (V_θ), resulting in a decrease in relative velocity, W. This is evident in the velocity triangles of Figure 3.1. Since the flow along the blade is decreasing in velocity, the blade passage acts as a diffuser, hence creating pressure rise through the blade row. For a control volume at radius r, the torque, or angular momentum, acting on the fluid in the blade passage can be written as

$$\tau = \dot{m} \cdot ((rV_\theta)_2 - (rV_\theta)_1)$$ **Equation 3.5**

The work done on the fluid by the rotor can be expressed as

$$w_c = U(V_{\theta 2} - V_{\theta 1})$$ **Equation 3.6**

This equation can also be written in terms of the stagnation enthalpy using the first law of thermodynamics resulting in Equation 3.7.

$$h_{02} - h_{01} = U(V_{\theta 2} - V_{\theta 1})$$ **Equation 3.7**

The entire process for a compressor stage is shown on the enthalpy-entropy diagram in Figure 3.2 (Cousins, 1997).

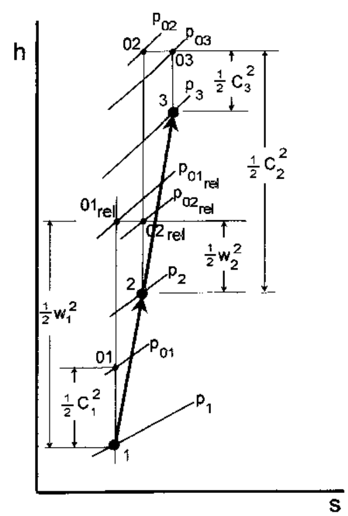

Figure 3.2: Enthalpy-entropy Diagram for an Axial Compressor Stage (Howard, 1999)

The total-to-total stage efficiency is defined by

$$\eta_{st} = \frac{h_{03s} - h_{01}}{h_{03} - h_{01}}$$ **Equation 3.8**

By using this equation and isentropic pressure-temperature relationship the stage pressure ratio may be found by

$$\frac{p_{03}}{p_{01}} = \left[1 + \eta_{st}\,\frac{\Delta T_0}{T_{01}}\right]^{\gamma/(\gamma-1)}$$ **Equation 3.9**

The absence of time dependent terms indicates that these equations are applicable to steady-state analysis only. They assume that any changes in the inlet conditions are carried through the blade instantaneously, immediately resulting in the new steady state properties and a new operating point on the steady-state performance characteristic.

However, in reality, these changes are not instantaneous; there is a response time associated with every compressor blade row. By viewing the blade loading as a function of distance along the chord, it is evident how the blade creates the pressure rise by diffusing the fluid flow. Figure 3.3 shows the blade loading of a current technology blade.

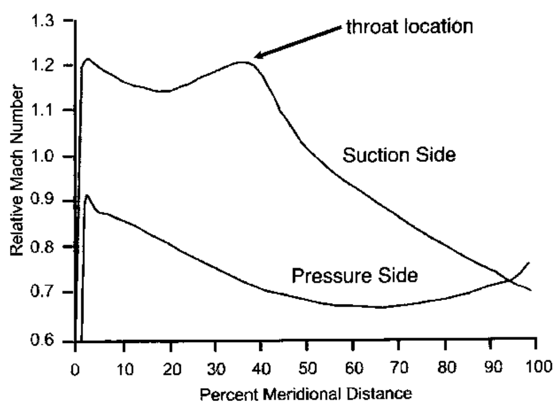

Figure 3.3: Typical Axial Rotor Loading Distribution (Howard, 1999)

A finite amount of time is required for the fluid particle to advance the length of the compressor blade. This time is called the fluid transport time as mentioned in the literature review, as described by Cousins (1997). Because of this time, the blade will not instantly respond to a change in flow properties upstream of the blade.

A better understanding of how the compressor rotor blade creates a pressure rise allows for the basis of understanding of how a blade will respond dynamically to non-uniform or unsteady inlet flow.

4 Experimental Setup and Data Acquisition

The present experimental investigation is identical to the Boller (1998) study with a few exceptions. It was desired that the machine speed be the only variable between the two studies. However, data acquisition was improved upon where deemed appropriate as detailed in this section. This chapter is presented as described by Boller (1998) with minor changes in content and format, as appropriate, to suit the present investigation.

4.1 Test Rig

4.1.1 Test Cell

The test cell is located at the Virginia Tech Airport with a layout as shown below in Figure 4.1. Its overall dimensions are 25.0 ft (7.62 m) in length, 12.5 ft (3.81 m) in width, and 15.0 ft (4.57 m) in height.

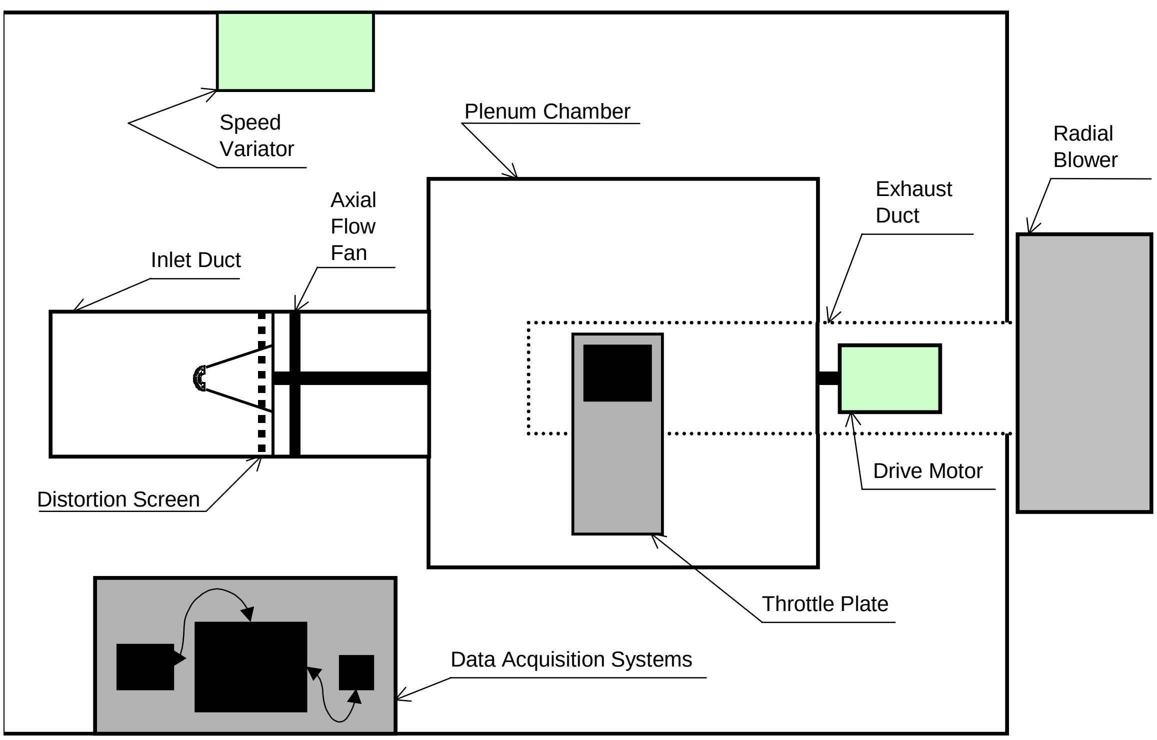

Figure 4.1: Schematic of Test Cell (Top View) (Boller, 1998)

4.1.2 Machine and Rotor

The test machine used in this experiment is an open-circuit, subsonic General Electric Company Model 5GDY34A1 axial-flow compressor. Figure 4.2 is a picture of the test machine without the inlet duct; this provides a good view of the rotor.

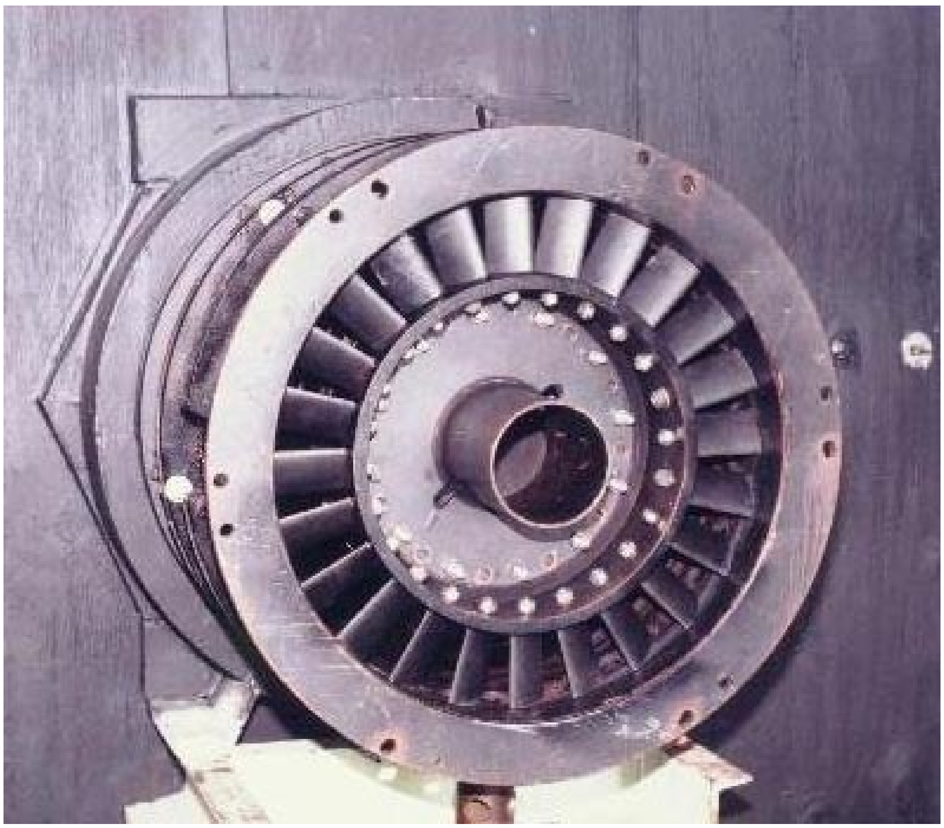

Figure 4.2: Photo of Low-speed Rotor (Boller, 1998)

The compressor can be operated in either a one-stage or two-stage configuration. However, for this investigation it was used as an isolated rotor without stators or inlet guide vanes (IGV's) to eliminate the effects of inter-stage flow interactions. The rotor shaft is driven by a 5 Hp General Electric motor with a continuously variable rotational speed. The annulus has an inner diameter of 12.375 inches (0.314 m) and an outer diameter of 18.0 inches (0.457 m). The rotor consists of 24 RAF-6 propeller sections whose profile is shown in Figure 4.3.

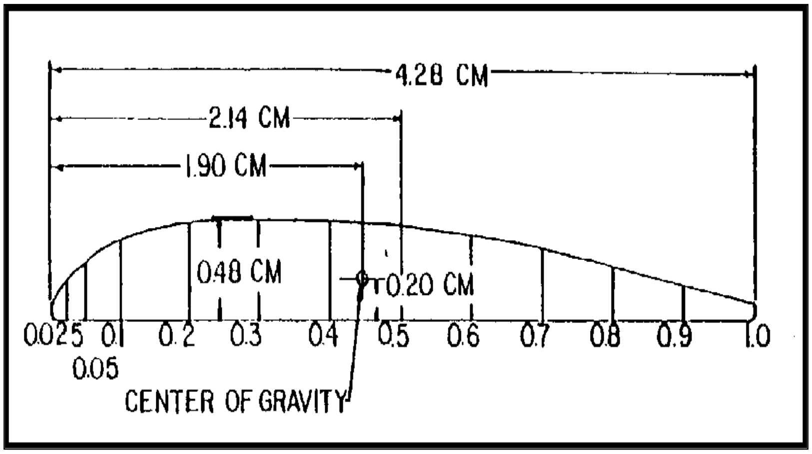

Figure 4.3: Cross Section of RAF-6 Airfoil

These blades have a span of 2.75 inches (0.070 m) and chord length of 1.67 inches (0.0424 m). A stagger angle of 55° at the mid span and 4° angle of twist result in a tip angle of 57° and a root angle of 53° from the machine axis. The nominal rotor blade casing clearance was 0.05 inches (0.0013 m). This arrangement resulted in a hub to tip ratio of 0.687, a solidity of 0.84 at the mean radius, and an aspect ratio of 1.68, producing a flow area of 0.975 ft^2 (0.091 m^2). An aluminum nosecone positioned at the rotor inlet had a base diameter of 12.375 inches (0.314 m), an axial length of 18.0 inches (0.457 m), and a tip radius of 1.5 inches (0.038 m).

4.1.3 Inlet Duct

An 18.0 inch (0.457 m) diameter, steel, circular inlet duct of 4.0 ft (1.219 m) axial length precedes the rotor inlet. An aluminum bellmouth is attached to the front of the inlet duct. The bellmouth, inlet duct, and plenum chamber are shown in Figure 4.4 as it exists during the testing.

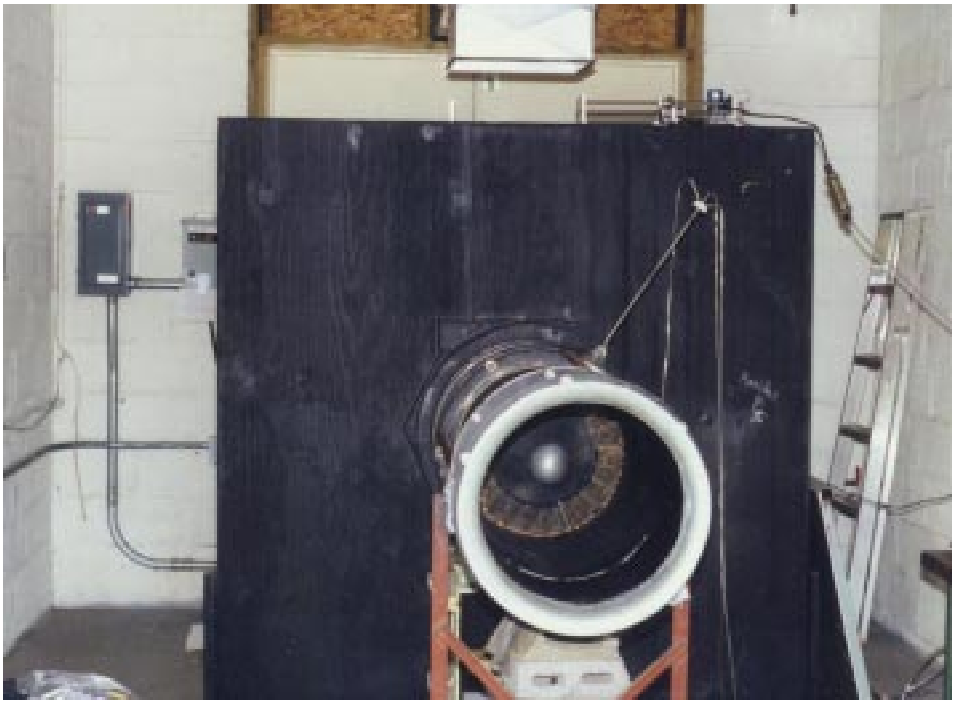

Figure 4.4: Photo of Bellmouth, Inlet Duct, and Plenum Chamber (Boller, 1998)

4.1.4 Plenum Chamber

The compressor rig forces the air into a wooden plenum chamber with dimensions of 6.0 ft x 6.0 ft x 4.0 ft (1.83 m x 1.83 m x 1.22 m) having a volume of 144.0 ft^3 (4.08 m^3). A mechanical throttle valve (metal plate) is located on the top of the plenum chamber and is driven by an electric traverse mechanism, allowing throttling of the rotor by decreasing the plenum flow discharge area. The top of the plenum chamber and the throttle valve are shown in Figure 4.5. Due to difficulty in stabilizing the performance of an isolated rotor, the throttle plate was controlled using a feedback control loop which reduced the plenum total pressure and inlet five-hole probe port measurement unsteadiness to $\pm$ 5% for normal unstalled operation.

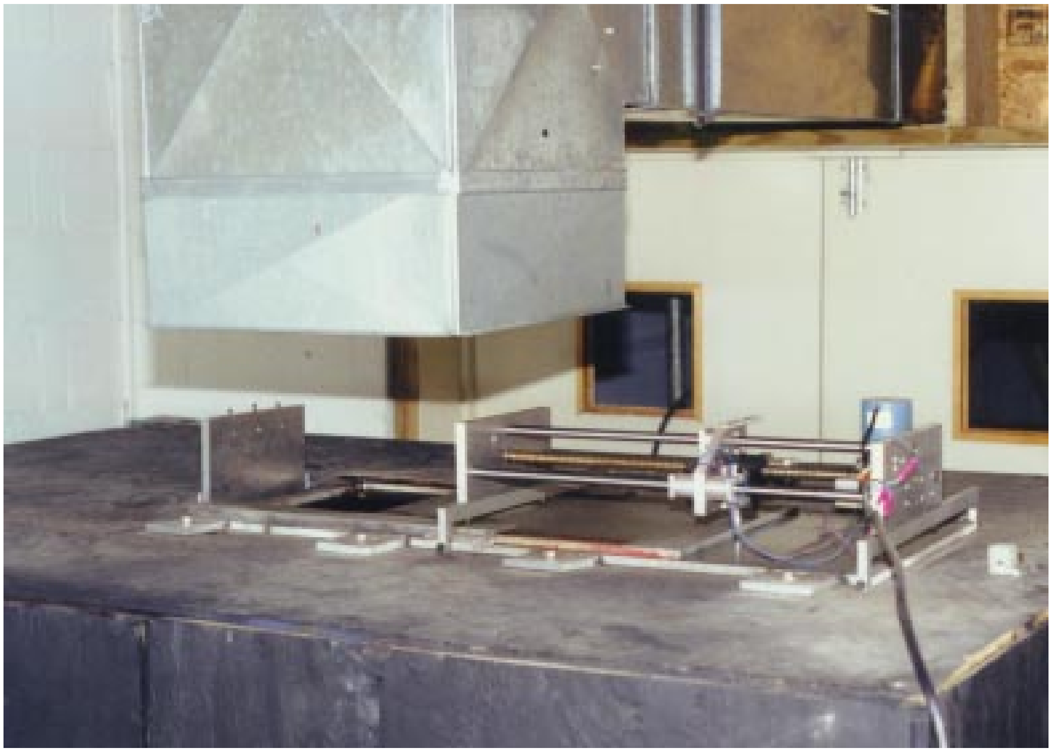

Figure 4.5: Photo of Plenum Chamber and Throttle Valve (Boller, 1998)

4.2 Circumferential Total Pressure Distortions

The distortion screens used in this experiment are identical to those used by Boller (1998). The screens were 110° in circumferential extent to generate the desired inlet circumferential total pressure distortion. Each screen was mounted on a rotatable support mesh assembly located approximately 0.8 chords or 1.375 inches (3.493 cm) upstream of the rotor. The support mesh covered the entire 360° circumference of the inlet and consisted of stainless steel welded wire cloth with a 3 x 3 mesh of 0.047 inch (1.2 mm) wire diameter. The N x N notation below refers to the number of wires per square inch of the grid, while d refers to the wire diameter in inches. Three different screen combinations were employed to create three different intensities of distortion. Distortion 'intensity' is the amount of total pressure loss. Each intensity is referred to as a screen 'Level' of distortion herein and are presented below in order of increasing total pressure loss:

Screen (Level) 1: one 5 x 5, d = 0.041 coupled with one 3 x 3, d = 0.047.

Screen (Level) 2: one 4 x 4, d = 0.047 coupled with one 14 x 14, d = 0.020.

Screen (Level) 3: one 10 x 10 d = 0.025 coupled with one 8 x 8 d = 0.025 and one 12 x 12 d = 0.023.

Rotating the support mesh with the mounted distortion screens was equivalent to rotating the instrumentation in the stationary (absolute) frame of reference. Photos of the inlet duct and support mesh with and without a 110° distortion screen installed are shown in Figures 4.6 (a) and 4.6 (b), respectively. (Note: The support mesh is not nearly as dense as it appears in the photos below.)

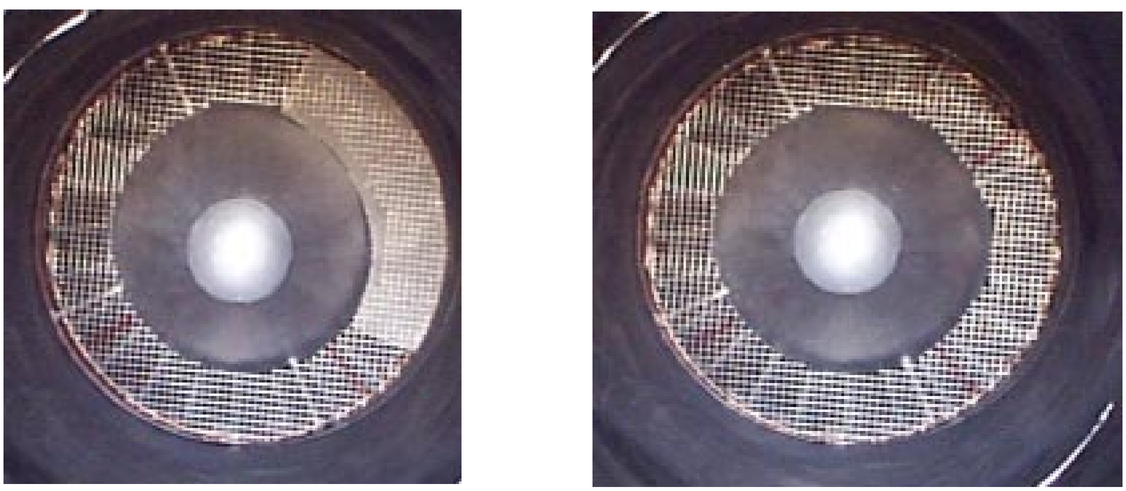

(a) (b)

Figure 4.6: Photo of Support Mesh With and Without 110° Distortion Screen (Boller, 1998)

4.3 Instrumentation

4.3.1 Mass Flow Rate

In order to create a performance map for the compressor, the mass flow rate was needed. This was measured using two United Sensor USC-N-210-A Pitot probe rakes for boundary layer regions and a Pitot-static probe measuring the inviscid core flow. The mass flow rakes were located in the inlet two machine diameters or 36.0 inches (0.914 m) upstream of the rotor as shown in Figures 4.7 and 4.8.

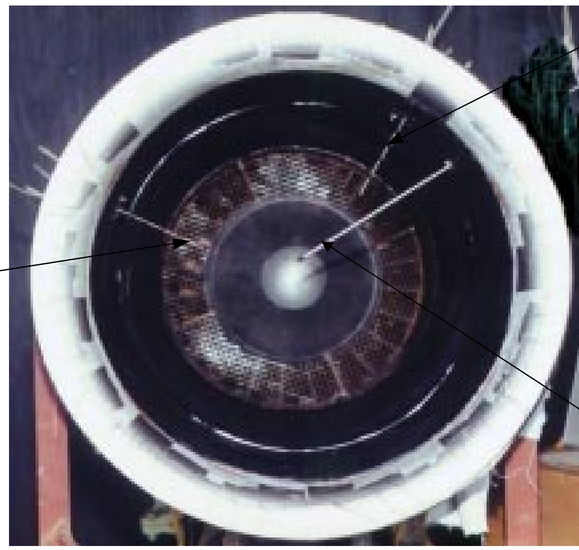

Figure 4.7: Frontal View of Probes for Mass Flow Measurement (Boller, 1998)

This distance was considered adequate in order to minimize upstream communication from the downstream rotor and screen combinations in the subsonic axial flow.

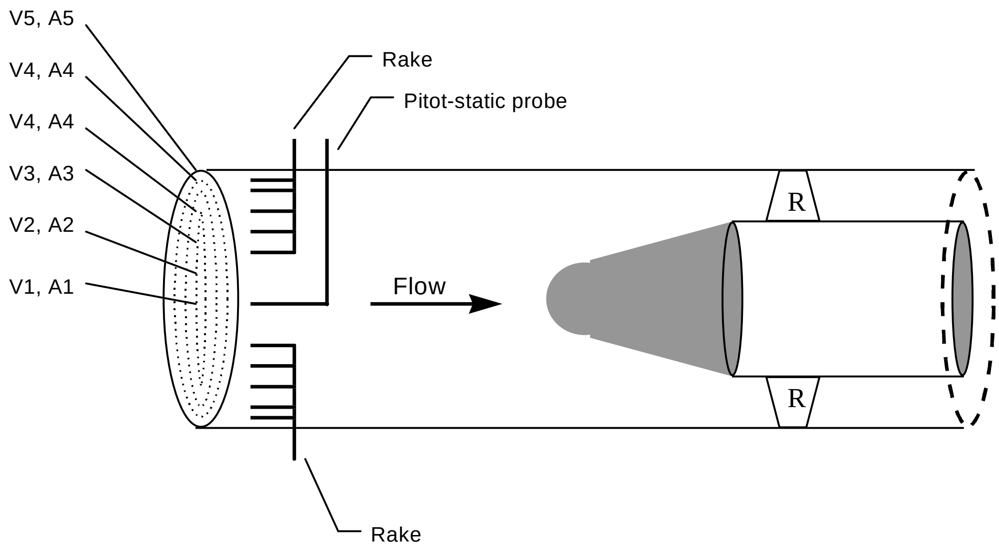

Figure 4.8: Diagram of Area-Average Mass Flow Measurement Scheme (Boller, 1998)

An area-average technique was employed to calculate the mass rate of flow, and is presented here as described by Boller (1998). The inlet static pressure P_s was obtained using the static component of the Pitot-static probe and axial velocities were obtained using the reduced Bernoulli equation with the inlet total pressure P_t

$$V = \sqrt{2(P_t - P_s)/\rho} \qquad \textbf{Equation 4.1}$$

This procedure assumes a negligible static pressure gradient in the boundary layer of the inlet measurement plane. With the inlet area discretized into concentric circles of area A_i with respect to the Pitot probe positions, the integral from the machine axis to the duct outer edge

$$V_{Ave} = \frac{1}{A} \int V(r)dA \qquad \textbf{Equation 4.2}$$

was approximated as

$$V_{Ave} = \frac{\sum V_i A_i}{\sum A_i} \qquad \textbf{Equation 4.3}$$

and the resulting average axial velocity at the duct inlet was used to obtain the mass rate of flow through the fan using conservation of mass principles.

4.3.2 Rotor Inlet Flow Measurements

A United Sensor DA 125 five-hole prism probe provided data to determine the three-dimensional velocity triangle at the inlet of the rotor. The probe was placed 0.25 chords or 0.4175 inches (0.0106 m) upstream of the rotor leading edge, where inlet flow angles were assumed steady. A schematic of this probe is shown in Figure 4.9. The probe was used in a non-nulling mode throughout the investigation in that it had a fixed orientation with respect to the machine axis. This probe had five measuring ports, one for total pressure measurement and four for pitch and yaw flow angle measurements, which correspond to stationary frame radial (pitch) and circumferential (yaw) flow angles in the turbomachine.

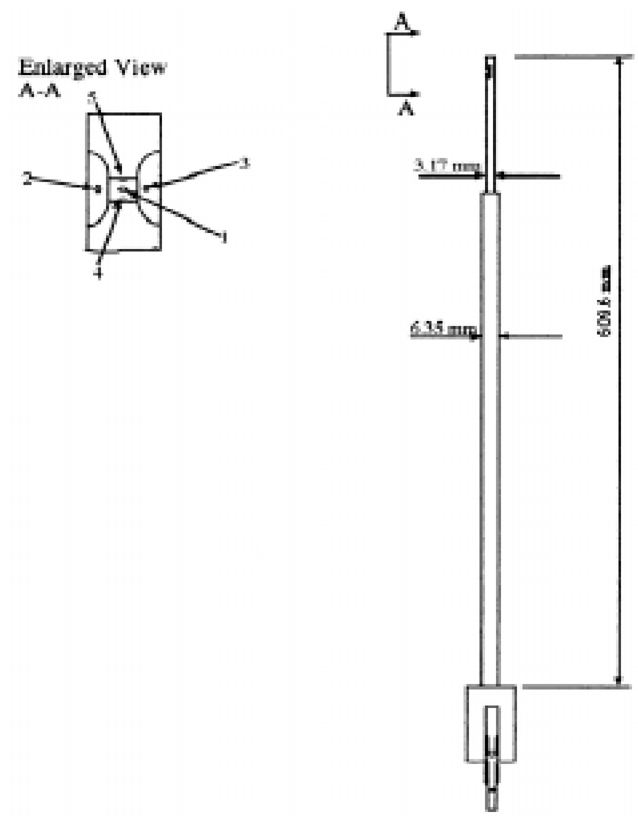

Figure 4.9: Schematic of Five-Hole Pneumatic Pressure Probe

(note: dimensions shown are not applicable to probe used in present experiment)

The procedure of Treaster and Yocum (1979) was used to process the five-hole probe data using the dimensionless pressure coefficients in Equations 4.4 as related to the indices shown in Figure 4.10. Total pressure p_1 is measured at the central probe hole, while p_2 and p_3 are measured in the yaw plane and p_4 and p_5 are measured in the pitch plane.

$$Cp_{pitch} = \frac{p_4 - p_5}{p_1 - \bar{p}}$$

$$Cp_{yaw} = \frac{p_2 - p_3}{p_1 - \bar{p}}$$

$$Cp_{total} = \frac{p_1 - p_{total}}{p_1 - \bar{p}}$$

$$Cp_{static} = \frac{\bar{p} - p_{static}}{p_1 - \bar{p}}$$

$$\bar{p} = \frac{p_2 + p_3 + p_4 + p_5}{4}$$

Equations 4.4

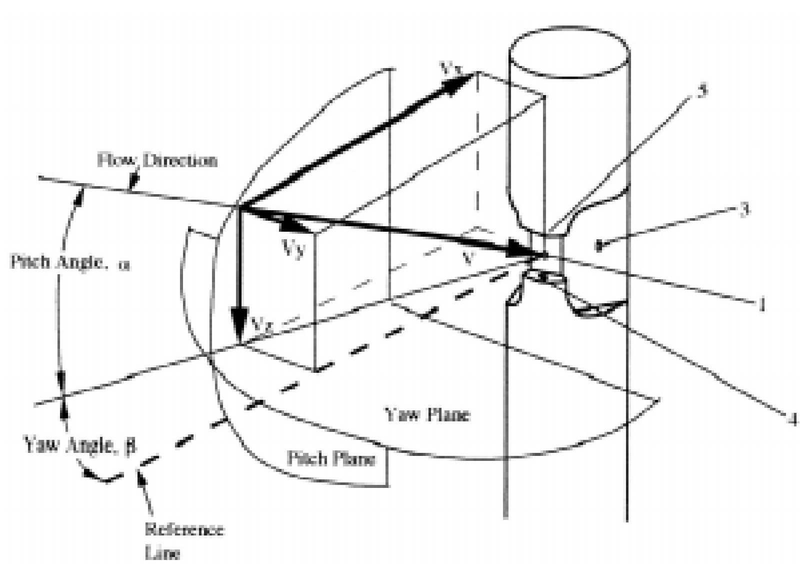

Figure 4.10: Schematic of Five-Hole Pressure Probe Tip and Flow Angles

Calibration data for this five-hole probe was obtained from Aeroprobe, Inc. The calibration data is very similar to that in Figure 4.11. The calibration range was ± 31.2° with 2.4° increments in both the yaw and pitch planes. The data was represented by cubic spline curves passed through the individual data points, a technique described in Appendix E. Wall proximity effects were neglected for the five-hole probe due to the lack of necessary measurements in this region as well as the relatively flat response of the pressure coefficients to wall proximities greater than 0.276 inches (0.007 m). Reynolds number effects were also neglected due to the pressure coefficients being weakly dependent on velocity or Reynolds number (Treaster and Yocum, 1979).

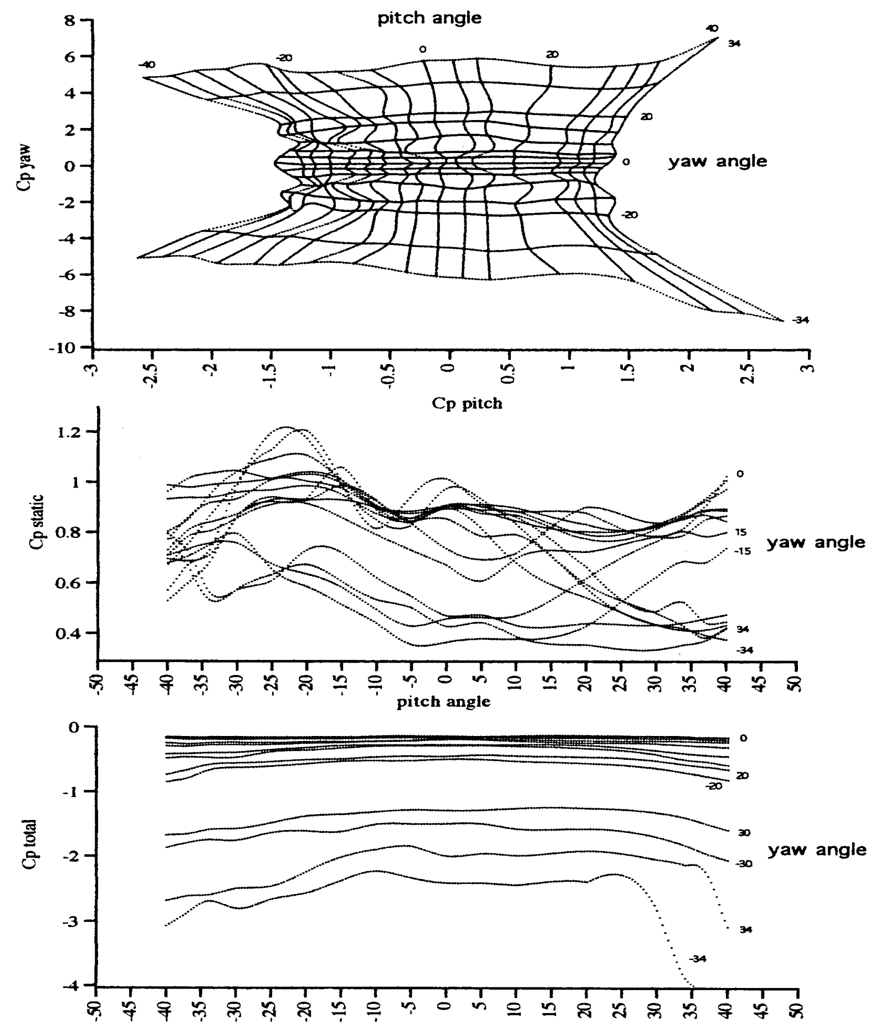

Figure 4.11: Calibration Curves for Five-Hole Pressure Probe (Treaster and Yocum, 1979)

A schematic of the inlet and total pressure ratio measurement pneumatic probes and their installation with respect to the rotor is shown in Figure 4.12. A static pressure tap from the wall of the plenum chamber was used to measure the pressure rise across the fan relative to atmospheric. Flexible Tygon tubing connected the pressure probes to a Scanivalve model W1260/12P-12T fluid switch wafer. Pressures were then measured by a Datametrics Barocel Type 590D-10W-2P1-V1X-4D Transducer and Type 1400 Electronic Manometer. This arrangement allowed pressure measurements accurate to 0.001 inches (2.54 x 10^{-3} cm) of H_20 with a differential range of 10.0 inches (25.4 cm) of H_2O. Data was read into and averaged by a LabView virtual instrument **mean.vi**.

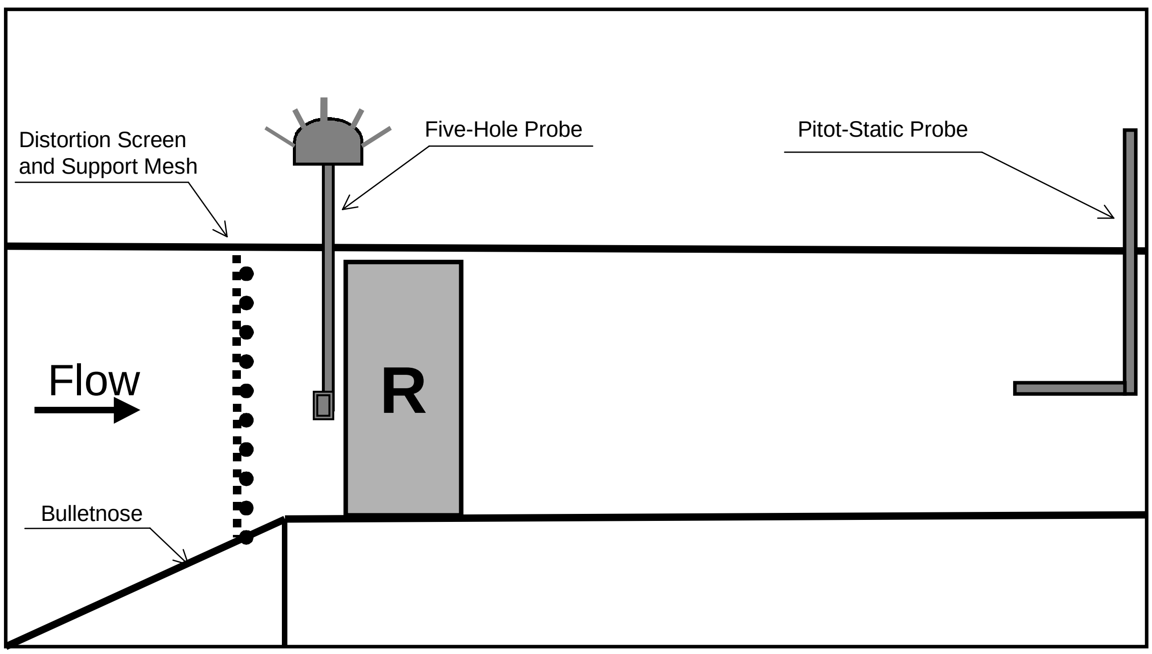

Figure 4.12: Pneumatic Probes Relative to Rotor in Meridional Plane (Boller, 1998)

4.3.3 Rotor Outlet Flow Measurements

One-dimensional wake data was obtained using a piggyback steady/unsteady total pressure probe located 0.2 C or 0.334 inches (0.848 cm) downstream of the rotor. A schematic of this probe is presented in Figure 4.13. The steady-state pressures were obtained from the pitot-tube portion of the combination probe, while the unsteady high response pressures were obtained from the Entran pressure transducer. The manufacturer's specification diagram for the Entran transducer contained in the probe is shown in Figure 4.14.

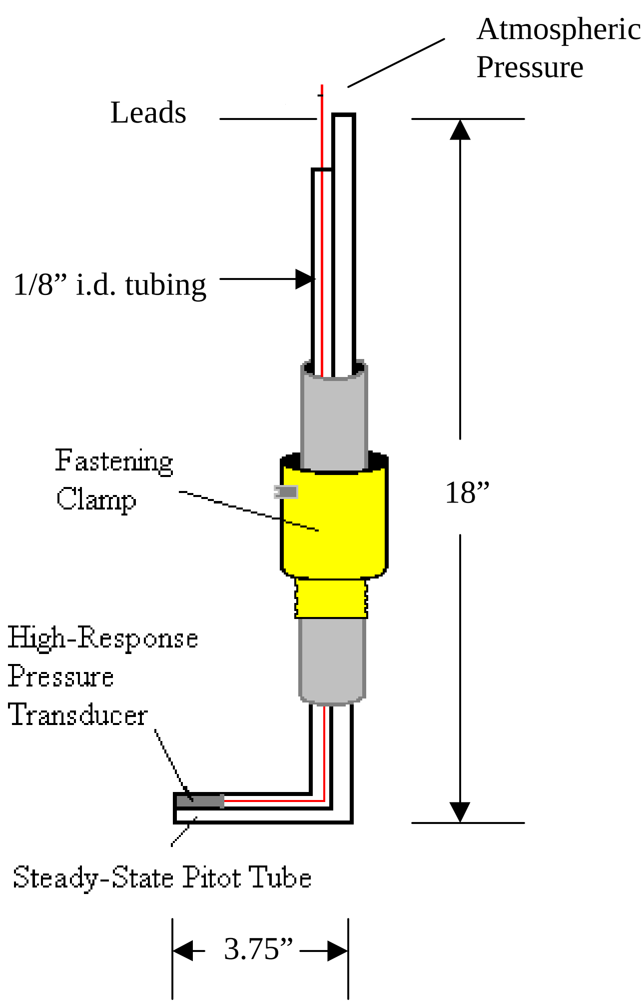

Figure 4.13: Diagram of Piggyback Steady/Unsteady Total Pressure Probe

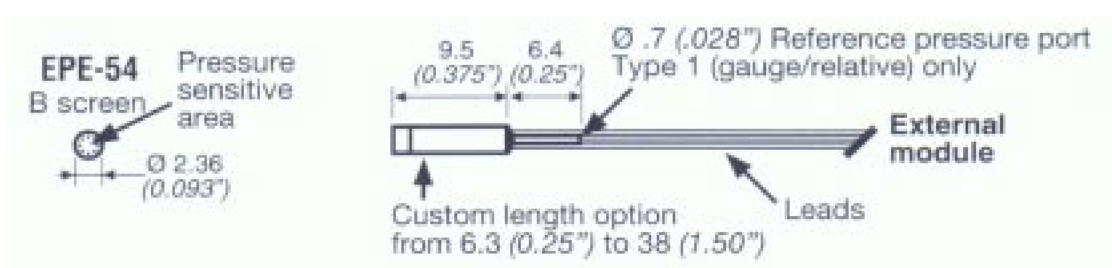

Figure 4.14: Diagram of High-Response Entran Pressure Transducer

The position of the combination probe downstream of the rotor is shown in Figure 4.15.

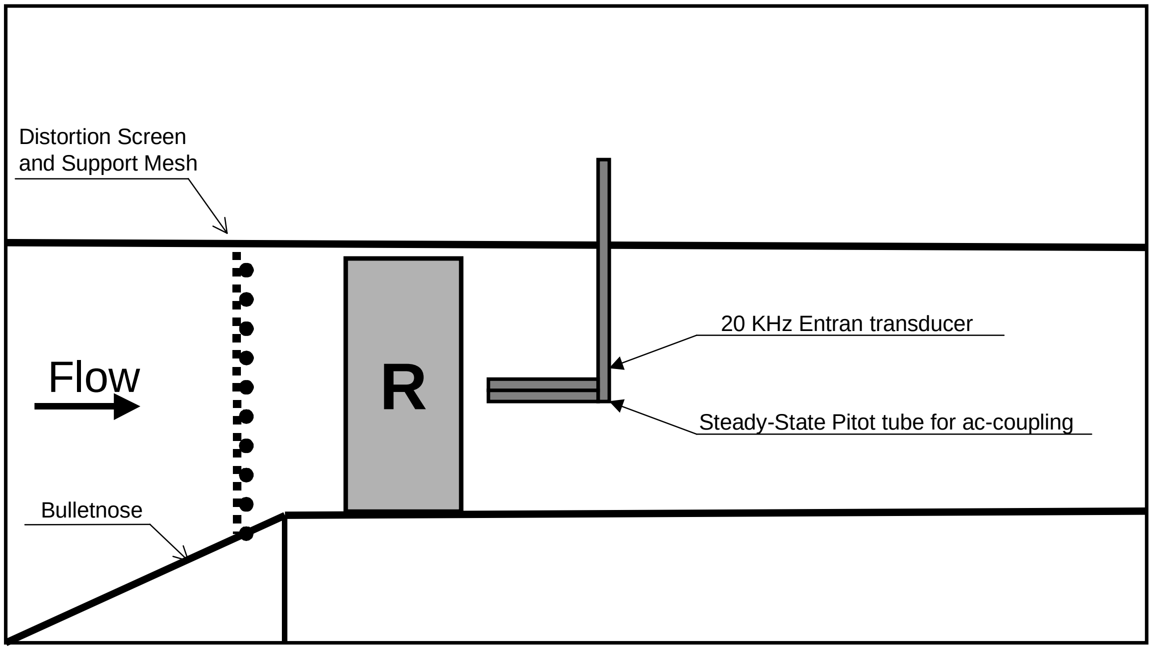

Figure 4.15: Diagram of Steady/Unsteady Probe Relative to Rotor (Boller, 1998)

A high-pass RC analog filter with –3 dB cutoff at 1.6 Hz was applied to the transducer output. Dynamic total pressure data was not low-pass filtered to eliminate aliasing about the Nyquist frequency of 15 kHz due to the rapidly decreasing energies approaching 15 kHz, as shown in Figure 4.16. The power spectrum shown in Figure 4.16 was obtained using a MATLAB zero-padding FFT sequence length of order $2^{12} = 4096$.

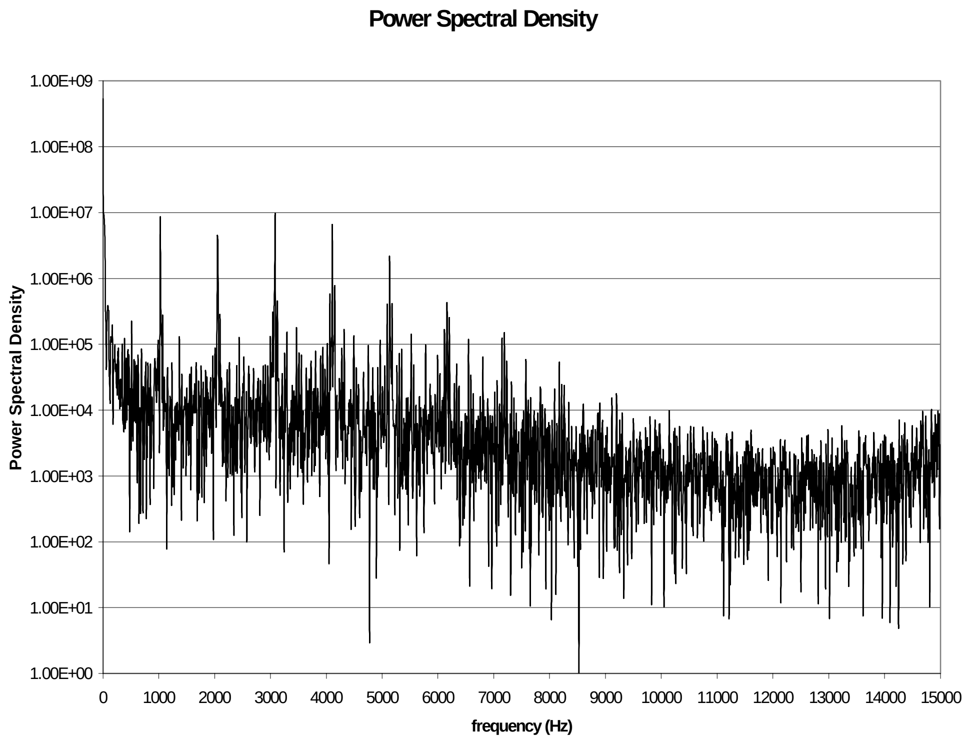

Figure 4.16: Power Spectral Density of Sample Unsteady Total Pressure

4.4 Instrumentation Calibration

The Barocel micromanometers were calibrated against an inclined manometer containing red gauge oil. A linear regression was used to obtain the line fitting of calibration data, as shown in Figure 4.17. Each of the two manometers used was calibrated periodically throughout the investigation.

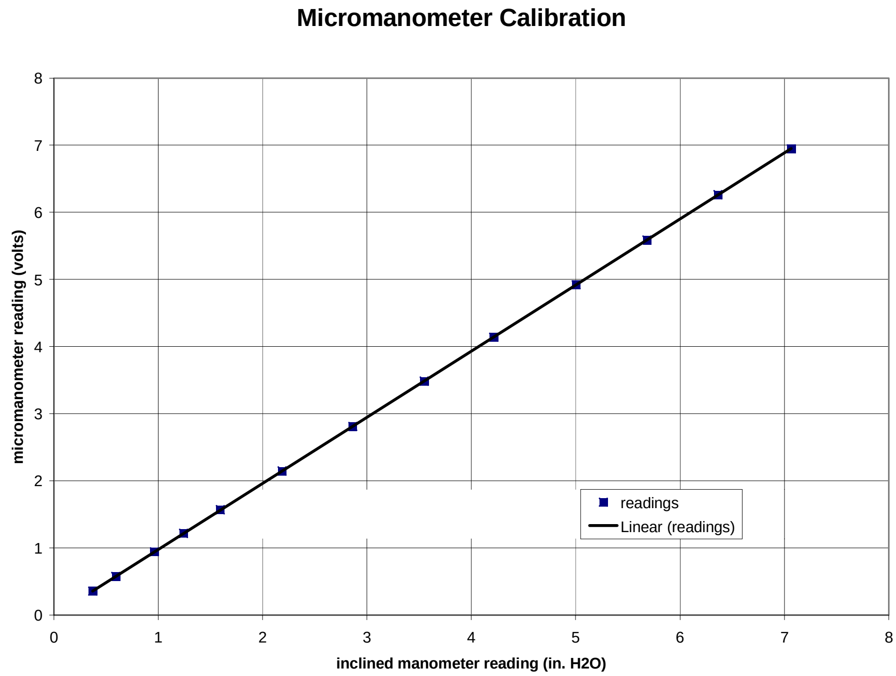

Figure 4.17: Plot of Micromanometer Calibration

The manufacturer's calibration of 77.0 mV/psig was assumed accurate for the output pressure transducer that was used for the high response wake measurements. Amplifier gain was checked by unhooking the lead from the transducer and applying a known voltage before and after the amp, then reading the corresponding output voltages on a Fluke multimeter. Again, this was done repeatedly throughout the acquisition stage of the experiments.

4.5 Summary of Experiments

As mentioned, creating a compressor (rotor) performance map was the first step in the experimental study. The machine was run at a constant speed of 2580 rpm (referred to as 2600 rpm for convenience herein) with only the support mesh installed (no distortion screen). Mass flow measurements were taken using the instrumentation and analysis previously described in Section 4.3.1, and the pressure rise was obtained from a wall tap off of the plenum. These measurements were then repeated with each of the Level 1, Level 2, and Level 3 distortion screens installed.

The rotor characteristics were obtained by plotting the non-dimensional pressure rise Ψ versus the velocity coefficient C_x/U_{tip} as shown in the resulting performance map in Figure 4.18, where the non-dimensional pressure rise coefficient, Ψ, is defined by

$$\Psi = \frac{P_{ann} - P_{atm}}{\frac{\rho \cdot U_{tip}^{\ 2}}{2}} \qquad \textbf{Equation 4.5}$$

where P_{ann}, P_{atm}, ρ, U_{tip}, and C_x are annulus total pressure, atmospheric pressure, air density, blade tip velocity, and axial velocity, respectively.

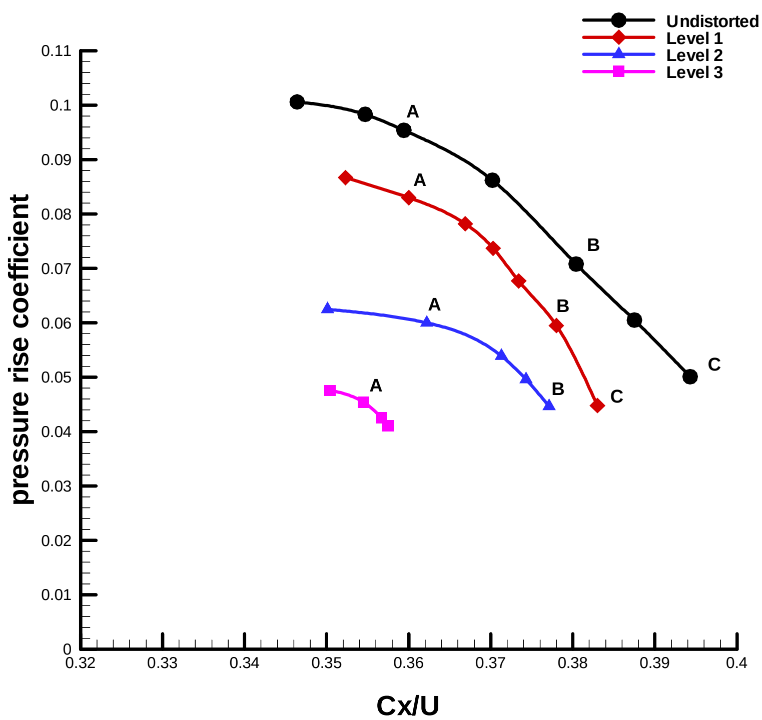

Figure 4.18: Distorted and Undistorted Performance Characteristics

The flow coefficient was varied by using the controlled throttle plate at the top of the plenum chamber. The rotor inlet total pressure was assumed to be ambient by neglecting losses through the inlet duct. Notice how the pressure rise and mass flow decrease as the intensity of the distortion increases, indicating decreased rotor performance. The operating points were chosen using stall margin as a basis; points A, B, and C correspond to stall margins of 5%, 15%, and 50% respectively.

Once the performance map was obtained, the rotor inlet flow was measured. The five-hole pneumatic pressure probe provided the inlet flow angles, in the yaw and pitch planes, and both the total and static pressures. Rotor flow data were obtained over a 270° circumferential sector with 10° resolution; this profile of 270° extent exceeded the fraction of the inlet that would experience the direct influence of the 110° distortion screens. Blade inlet data was taken at 1/3, 1/2, and 2/3 spans at operating points A, B, and C for all three screen levels as well as for the undistorted case (support mesh only). Blade loading increases as one moves up the speed line, with operating point A considered to be pre-stall. For the undistorted, case with only the support mesh installed, rotating stall inception occurred at a steady-state stalling angle of attack of 12.6º as measured by the five-hole probe at 1/2 span (Boller, 1998). This value was verified in the present study.

The final set of experiments involved the blade wake survey corresponding to the inlet flow measurements at 1/3, 1/2, 2/3 spans for operating points A, B, and C for each screen level. The five-hole inlet pressure probe was removed from the rotor inlet prior to obtaining downstream wake data to avoid flow interaction between probes. The rotor exit flow survey was also performed with 10° resolution about the 270° circumference of the annulus. The resulting inlet and exit flow data are presented in Section 5 and Appendix A.

4.6 Data Acquisition and Reduction

Measurements from the five-hole pneumatic probe for the steady inlet data were recorded at a sampling rate of 4 Hz for 40 seconds. Unsteady flow effects at the inlet were assumed negligible as compared to the rapid blade passing frequency behind the five-hole probe. This sampling rate and time were deemed adequate since they provided a value that did not vary more than 2% when taken with longer sampling times. The five-hole probe data allowed calculation of the three-dimensional inlet flow angles and magnitudes, as well as the total and static pressures at the inlet. Inlet flow angles are presented in Section 5 without modification. The inlet total and static pressures presented in Section 5, relative to the ambient, were non-dimensionalized by blade tip wheel speed as shown in Equations 4.6 and 4.7.

$$P_{static}\,Rel = (P_{static} - P_{amb}) / (\frac{1}{2}\rho \cdot U_{tip}^{2}) \qquad \textbf{Equation 4.6}$$

$$P_{total}\,Rel = (P_{total} - P_{amb}) / (\frac{1}{2}\rho \cdot U_{tip}^{2}) \qquad \textbf{Equation 4.7}$$

Unsteady wake data were obtained using the combination probe as previously described in Section 4.3.3. One-per-rev, downstream steady-state pressures, and transducer unsteady total pressures signals were sampled by the computer at 30 kHz for 0.12 seconds using a LabView virtual instrument **dynamic.vi**. Figure 4.19 depicts typical separate steady-state mean DC and unsteady AC total pressure components from the combination probe.

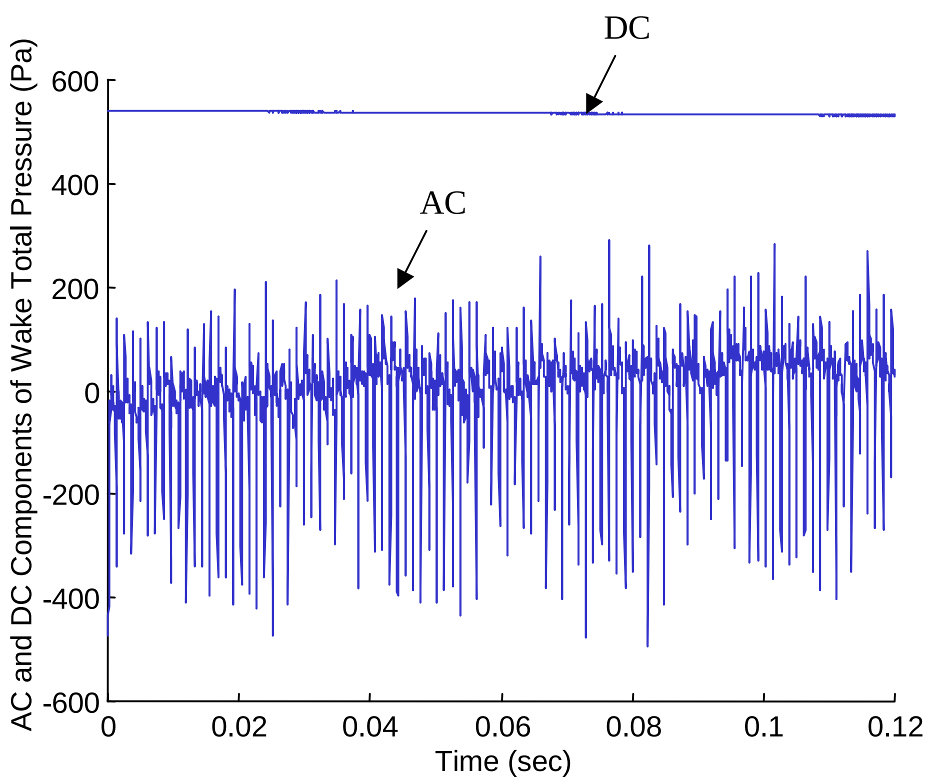

Figure 4.19: AC and DC Components of Total Pressure (Boller, 1998)

The unsteady AC and mean DC components were superimposed as shown in Figure 4.20 to obtain the complete unsteady total pressure profile downstream of the rotor. Filtering the DC component off of the unsteady signal allowed for higher resolution of the voltage measurements (maximizing dynamic range) by minimizing the channel voltage input range in the data acquisition routine **dynamic.vi** for the transducer output signal to ± 1.0 V. The data acquisition system consisted of a Gateway P166 laptop computer with a National Instruments DAQCard-AI-16E-4 I/O card as described in Appendix F. The rotor rotational speed was measured using a Hewlett Packard 5315A 100 MHz Universal Counter attached to a one-per-rev signal from the rotor shaft. Channel voltage ranges for the steady total pressure signal and the one-per-rev signal measurements were ± 5.0 V.

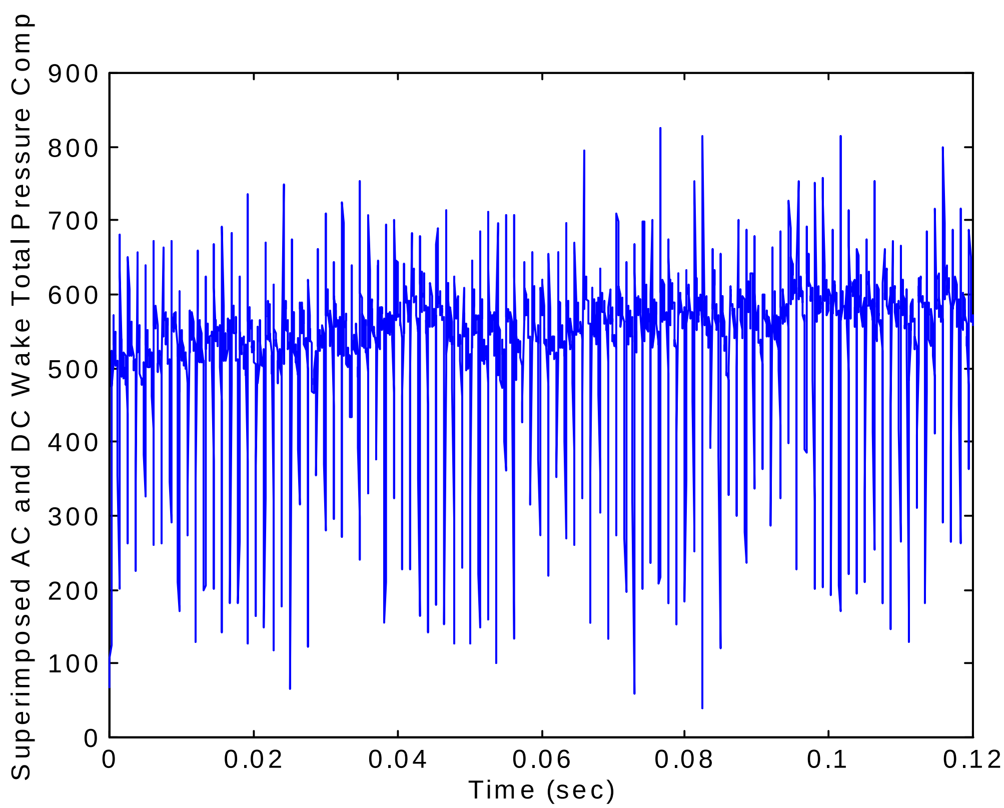

Figure 4.20: Superimposed AC and DC Components of Total Pressure (Boller, 1998)

With a blade passing time of roughly 0.97 msec and a sampling time of 0.12 seconds, the resulting data sets captured approximately 125 blade passages. This would then allow for 96 blade passages to be ensemble-averaged (assuming the data is stationary and ergodic) once the unsteady total pressure data was phase-locked with a one-per-rev signal from the rotor as described below.

Figure 4.21 displays a time series of one-per-rev voltage outputs used for phase-lock averaging. The secondary peaks are due to the presence of a balancing washer on the shaft.

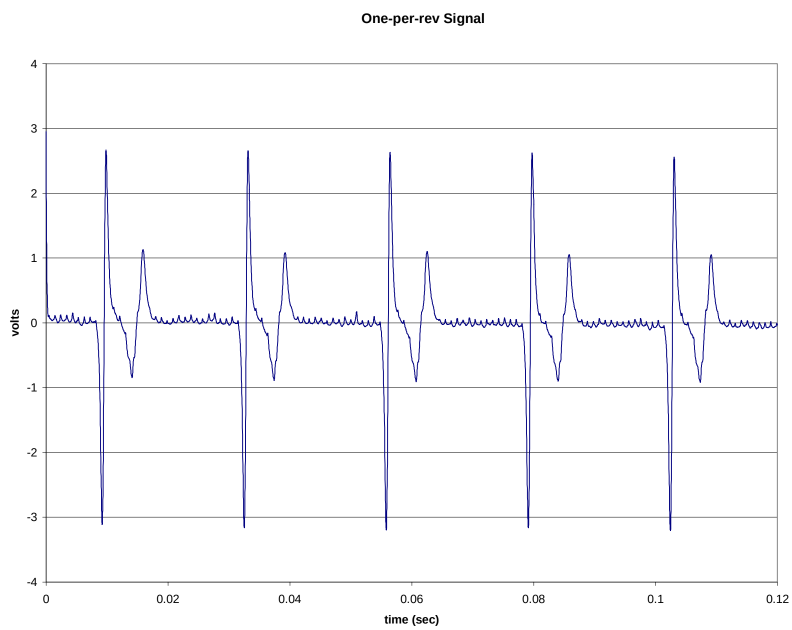

Figure 4.21: Time Series of One-per-rev Voltage Output Used for Phase-lock Averaging

Using each of the positive voltage peaks to obtain the phase, the superimposed unsteady total pressure signal was divided into data blocks corresponding to the data taken between each of the five one-per-rev peaks, the beginning of which is shown in Figure 4.22. Five one-per-rev peaks allowed for four full rotor rotations (or periods) and therefore a total of 96 blade passages as already stated. This number of blade passages provides an ensemble-average which is highly representative of the median unsteady blade exit flow.

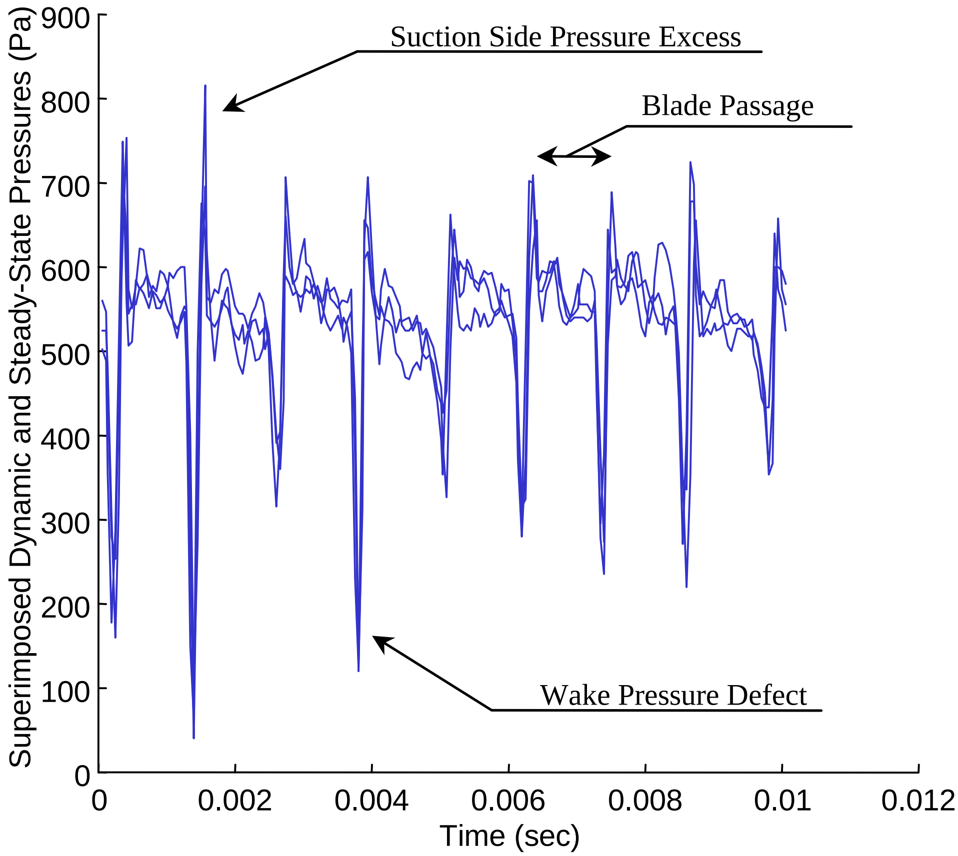

Figure 4.22: Sample of Ensemble Averaging of Three Wakes for Repeatability (Boller, 1998)

The four data blocks in Figure 4.22 were subsequently averaged to obtain a series of 24 unsteady rotor exit blade passes. This series of four passages of the same blades demonstrates excellent repeatability. It is interesting to note the considerable randomness of the suction side total pressure jets and freestream total pressures as seen in Figure 4.22. Wake characteristics such as thickness and maximum depth remain relatively constant for each individual blade passage.

Using the analysis of previous wake researchers as a foundation, a set of non-dimensional rotor exit flow parameters were calculated in order to describe the average total pressure width and depth for both the suction-side jet and the blade wake. Since there was no longer any absolute phase information in the one-dimensional rotor exit flow total pressure profiles, the non-dimensional parameters were computed for each of the 24 blade passes and then averaged once again. Figure 4.23 is a graphic of the analysis used for a sample blade passage.

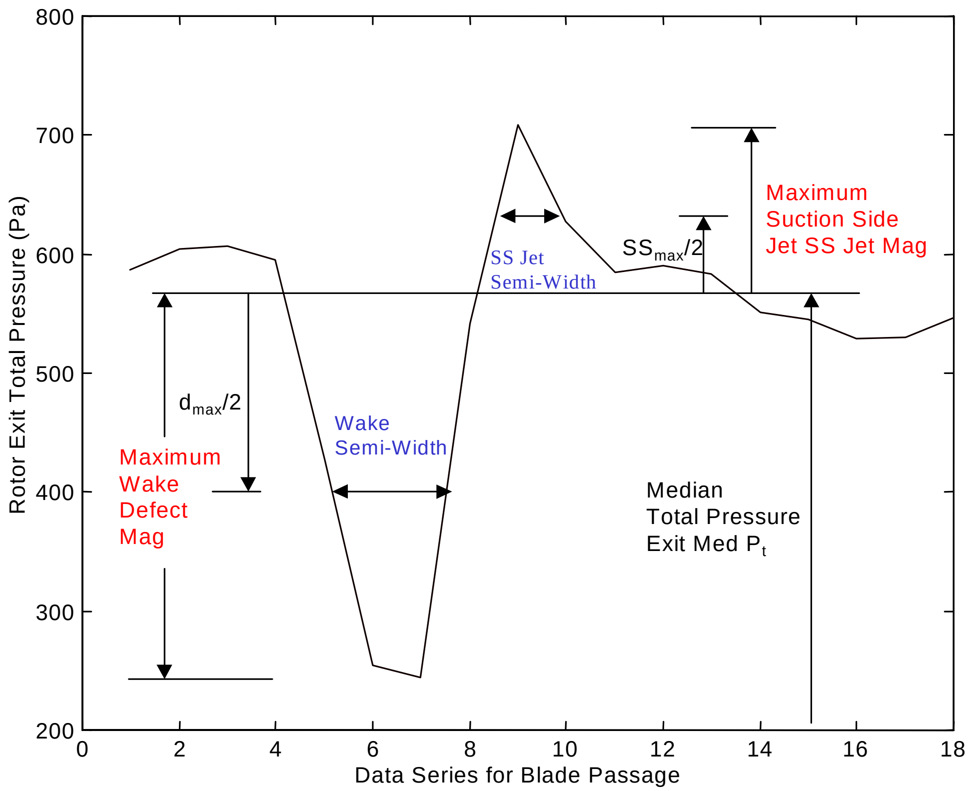

Figure 4.23: Exit Flow Parameters of Sample Blade Passage (Boller, 1998)

The total pressure suction side jet and wake defect were computed relative to the median of the superimposed total pressure signals Pt_{med}, which was judged to be a better approximation of the freestream velocity than the mean. These relative pressures for the suction side jet magnitude and wake depth were then non-dimensionalized by blade tip wheel speed as presented in Equations 4.8 and 4.9.

$$\text{SS Jet Mag} = (\text{SS Jet Max} - \text{Pt}_{\text{median}}) \;/\; (\frac{1}{2}\rho \cdot U_{tip}{}^{2})$$ **Equation 4.8**

$$\text{Wake Defect Mag} = -1 * (\text{Pt}_{\text{median}} - \text{Wake Defect}_{\text{max}}) \;/\; (\frac{1}{2}\rho \cdot U_{tip}{}^{2})$$ **Equation 4.9**

Suction side jet and wake semi-widths were converted from lengths to units of time and non-dimensionalized by the time, $\Delta t = 0.97$ msec, for a blade passage at 2580 rpm.

$$\text{SS Jet Semi-Width} = (\text{SS jet passage time} / \Delta t) \qquad \textbf{Equation 4.10}$$

$$\text{Wake Semi-Width} = (\text{Wake width passage time} / \Delta t) \qquad \textbf{Equation 4.11}$$

Linear interpolation was used to obtain the semi-widths for the suction side jet and the wake total pressure defect. The steady-state median exit total pressure was also non-dimensionalized by blade tip wheel speed as shown in Equation 4.12.

$$\text{Exit Med Pt} = (Pt_{\text{steady - state}} - P_{\text{atm}}) / \left(\frac{1}{2}\rho \cdot U_{tip}^{\ 2}\right) \qquad \textbf{Equation 4.12}$$

A Matlab program was written to reduce the outlet data sets to these non-dimensional parameters. The data presented in Section 5 and Appendix A are presented using cubic spline curve fitting techniques as described in Appendix E.

4.7 Differences Between Present Work and Previous Study

For convenience, the differences between the current project and that of Boller (1998) are listed below. It can be assumed that anything not listed is identical to that of the Boller project. The current project differs in that:

- The machine speed is roughly 25% higher (2580 rpm)
- The circumferential data resolution is increased to 10° (previously 30°)
- The outlet high response transducer was sampled at 30 kHz (previously 20 kHz) to gain better resolution
- A different inlet 5-hole probe (same model, different serial number) was used with a new, higher resolution calibration grid
- The current operating points do not directly correspond to those of previous work
- The computer code to reduce outlet data was significantly improved

5 Experimental Results and Discussion

The inlet and outlet surveys resulted in a number of data sets corresponding to a particular distortion level, operating point, and span location. All of these data sets are presented in Appendix A. There is some notation in regards to distortion level, span location, and operating point that needs to be addressed. For example, 'S1A13' represents a data set taken with distortion Level 1, at operating point A, at 1/3 span. The 'S1' (or 'S2', 'S3') refers to distortion level, the 'A' (or 'B', 'C') refers to operating point, and '13' (or '12', '23') refers to span location (1/3, 1/2 or 2/3 span respectively).

This chapter will highlight typical characteristics of both the inlet and outlet parameters of a data set as the blade passes in, through, and out of the distorted region of flow. The influence of span location, operating point (aerodynamic loading), and distortion level will be examined, as well as the time response of the exit flow parameters relative to the dynamic inlet flow conditions. Finally, the current data set will be compared to that of the Boller (1998) work to see if there are any speed dependencies (2100 vs. 2600 rpm).

Uncertainty analysis was performed and is presented in Appendix D. Also note that in all of the spline-fitted data, true data points are represented by the symbols (i.e. circle, square, etc.). Due to the nature of a spline fit, some existing peaks and troughs in the graphs are not necessarily true data points.

5.1 Characteristics of a Typical Data Set

Measurements taken at 1/2 span, with a Level 2 distortion screen, operating in the moderately loaded region of OP B, represent a typical data set for the current experiment. Figure 5.1 is a plot of the inlet parameters for this case (S2B12) as presented in Appendix A. These inlet parameters are angle of attack (AOA), pitch angle, and total and static pressure; all four parameters were calculated from the 5-hole prism probe measurements.

Plotting each of these parameters versus circumferential position provides a great way to see how they respond to the inlet distortion. The distorted region, as shown in Figure 5.1, is in the range of 0° to 110°. Looking at Figure 5.1, the angle of attack is fairly constant until the distorted region is reached. Then it increases rapidly to a fairly constant ‘distorted’ value in the distortion (due to the decreased axial velocity), often peaking at the trailing edge of the screen. The AOA then dips immediately after the trailing edge and eventually returns to its undistorted value. It is interesting to note that these higher values of AOA often exceed the steady-state stalling angle of 12.6° for an undistorted inlet (Boller, 1998). (This stalling angle was verified in this experiment as well when taking measurements for the undistorted case. These undistorted measurements are presented in Appendix A.) Dynamic stalling may be taking place in these regions of excessive angle of attack.

Typical characteristics of the pitch angle are that the value tends to be higher through the distortion and the angle dips at the screen edges. Fluctuations are much more prevalent in the pitch angle measurement. These fluctuations in pitch angle, as well as in the other parameters, may be due to the non-uniform porosity of the distortion screen and support mesh as proposed by Neal (1975). As for the inlet pressure profiles, both the total and static pressures stay constant in the undistorted region, but then drop to a lower value through the distortion due to the losses caused by the screen. The total pressure drop is much more drastic than that of the static pressure. It is not uncommon to find another slight dip in total pressure after the initial recovery at the trailing edge of the distorted region; this is evident when looking through Appendix A.

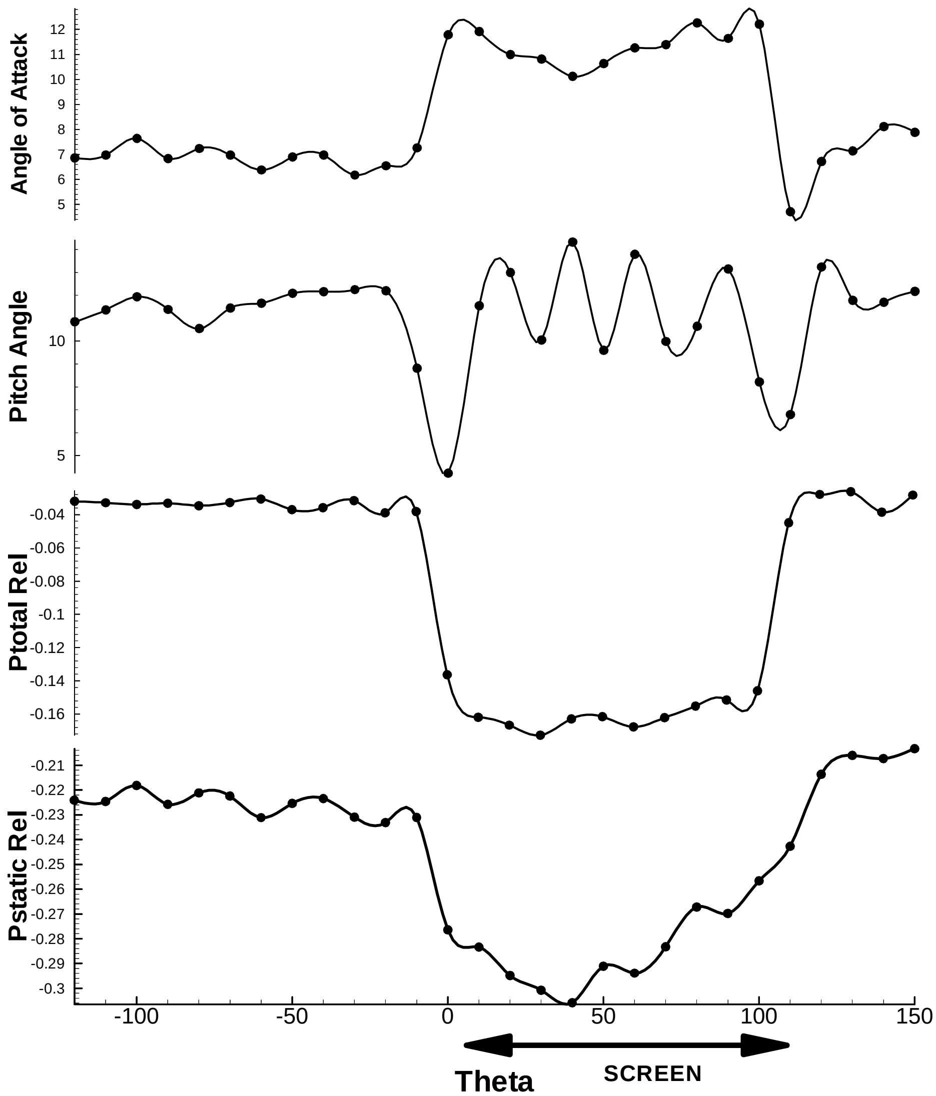

Figure 5.1 Inlet Flow Parameters for Level 2, OP B, 1/2 Span

In addition to the inlet parameters presented above, it is interesting to look at the inlet velocity profile as shown in Figure 5.2 (for the same case S2B12). The velocity slowly increases while approaching the distortion, then it drops off to its distorted value. It continues to steadily decrease to its minimum value at the trailing edge, then it recovers by peaking and eventually returns to its undistorted value. The increased velocity in the undistorted region near the screen edges is the flow's attempt to avoid the distortion screen by going around it; this more prevalent in a slow speed machine since the flow has more time to respond to the obstruction. Interestingly, the velocity in the undistorted region for this Level 2 case is greater than the velocity that results when the inlet is clean.

Dancy (1976) also noted this. In addition, it is typical to see a sharp increase in the velocity immediately before reaching the leading edge of the distortion; this was also noted by Gauden (1977).

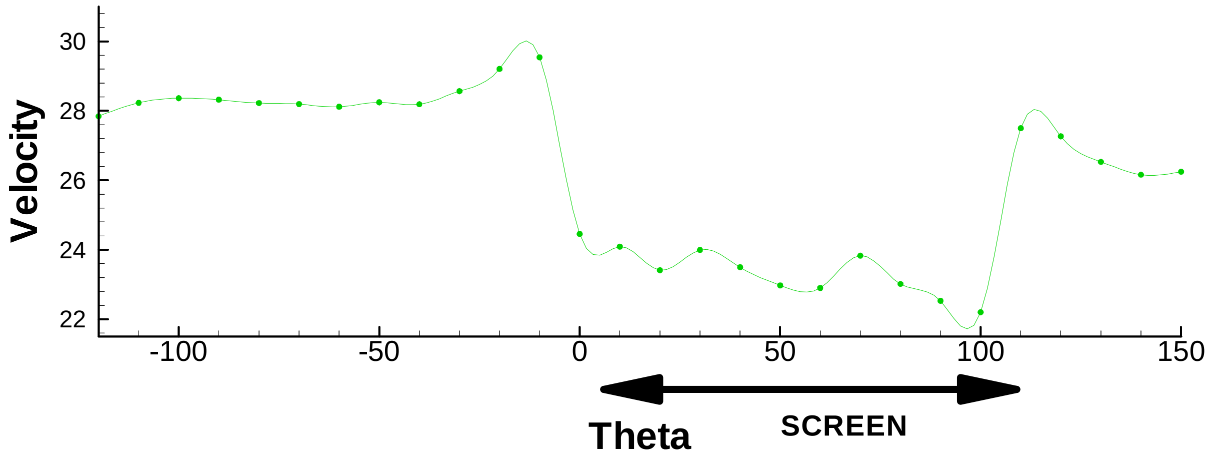

Figure 5.2: Inlet Velocity Profile for Level 2, OP B, 1/2 Span

This absolute velocity profile is almost identical to the axial velocity profile since the yaw angles are quite small, as expected in a compressor with no inlet guide vanes. Figure 5.3 shows a typical yaw angle profile. Assuming that Figure 5.2 represents the axial velocity profile as well, notice how the increased velocity at the edges of the distortion correspond to the dip in angle of attack as seen previously in Figure 5.1. This is in agreement with theory when considering the inlet velocity triangle relationships.

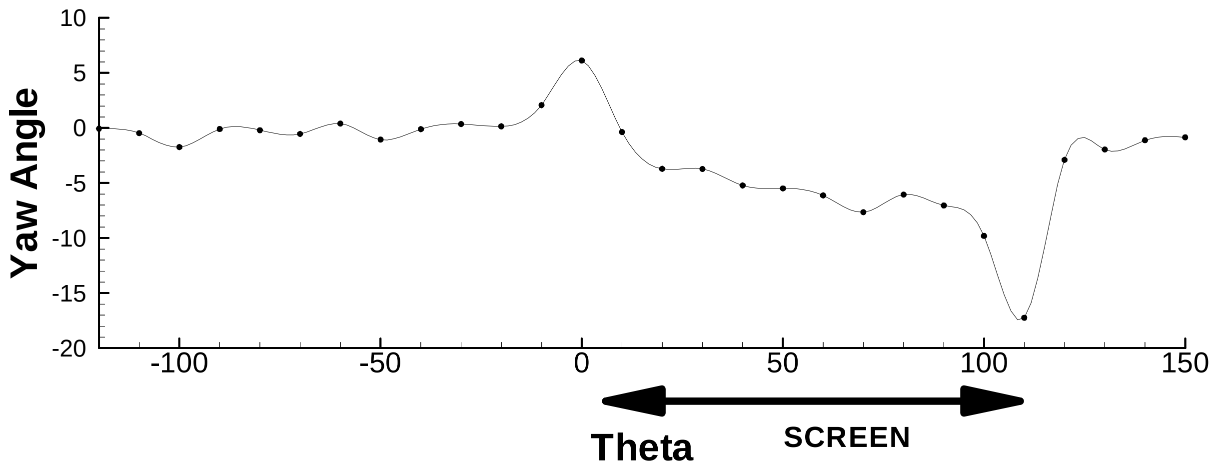

Figure 5.3: Typical Inlet Yaw Angle Profile

The exit flow was measured with the piggyback steady/unsteady probe detailed in Section 4.3.3. The exit flow parameters of this same case (S2B12) are presented in

Figure 5.4. The exit total pressure decreases as a result of the distortion. However, this drop is more gradual than the inlet profile. Typically, the pressure begins to drop ahead of the actual distorted region, however, it recovers fairly quickly right at the screen's trailing edge. The wake depth is constant until the distortion nears, then it peaks to its minimum value at the leading edge of the screen. It steadily increases in absolute magnitude to its maximum near the trailing edge of the screen, then it returns to its undistorted value. The wake width has the same behavior; it dips at the leading edge and peaks at the trailing edge. For the suction-side jet magnitude and width, there are no distinct typical characteristics except at the screen edges. It is typical for both parameters to dip at the leading edge and peak at the trailing edge while maintaining a fairly constant value elsewhere throughout the whole 270° profile.

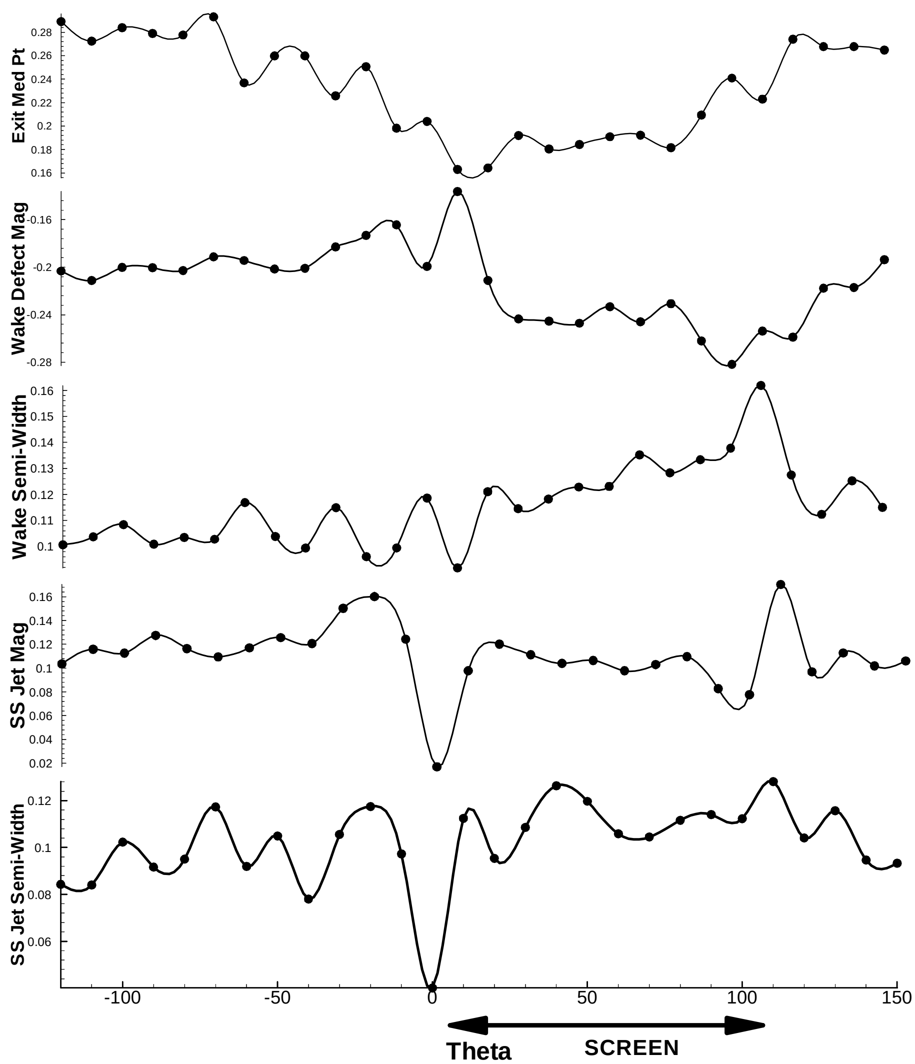

Figure 5.4: Exit Flow Parameters for Level 2, OP B, 1/2 Span

It is evident that the total pressure and wake parameters are more responsive to the change in inlet flow conditions. Therefore they will be the only outlet parameters used in the following comparisons.

5.2 Effect of Span

Span has a significant effect on both the inlet and outlet parameters as would be expected. Figure 5.5 below shows the typical effect of span on AOA, inlet velocity, and inlet total and static pressures. It is apparent that AOA increases with span both in and out of the distorted regions. The inlet velocity typically decreases going from hub to tip. The higher velocity toward the hub may be due to the bellmouth accelerating the flow outward radially as it travels from the inlet into the annulus area. Again, using the inlet velocity triangle relations, this decrease in velocity at higher span causes the increase in AOA as the span increases. Even though not shown, the pitch angle is larger at smaller radii also due to the bellmouth.

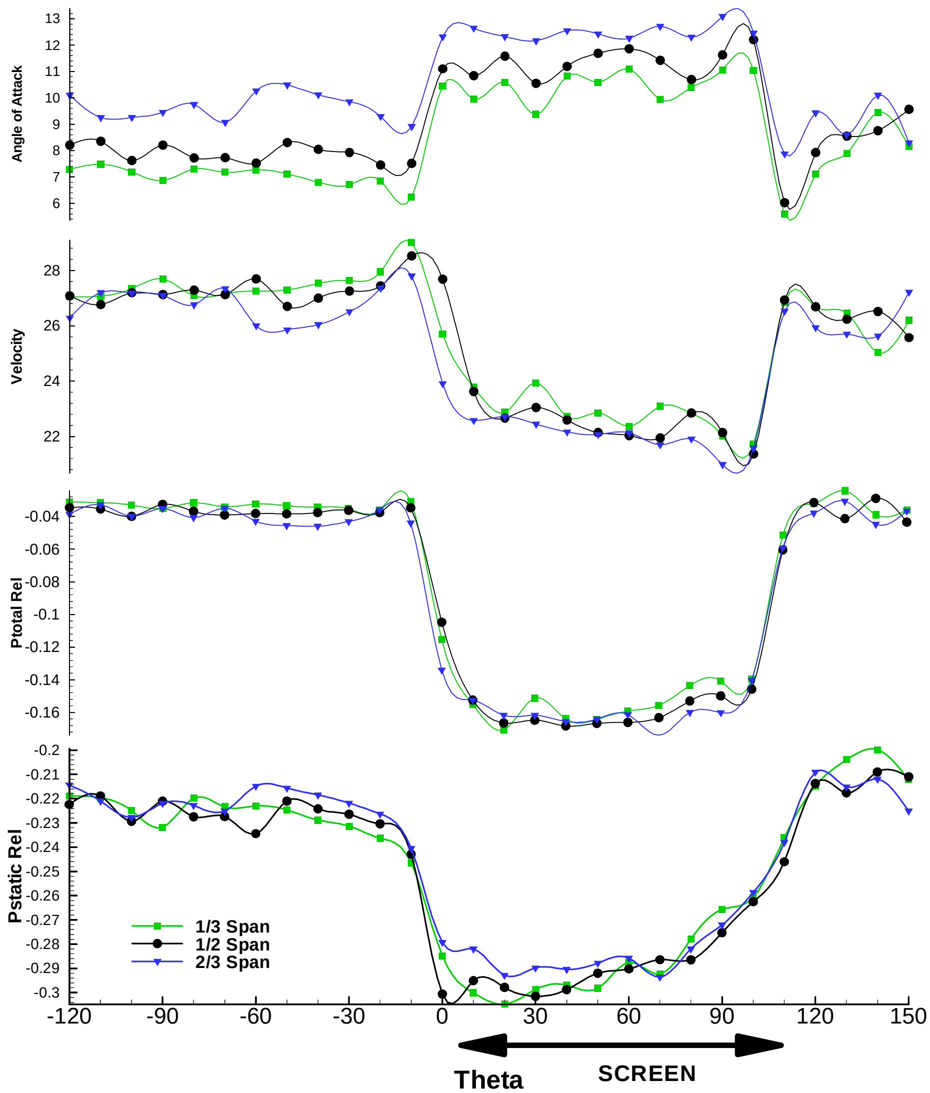

Figure 5.5: Effect of Span on Inlet Parameters (Level 2, OP A)

The inlet total and static pressure profiles tend to be unaffected by any change in span.

Of the exit flow parameters, only the total pressure and wake depth and width are compared versus span since the suction-side jet parameters do not demonstrate a strong response to the change in inlet conditions, as mentioned before. Figure 5.6 shows a typical plot comparing each of these parameters with respect to span location.

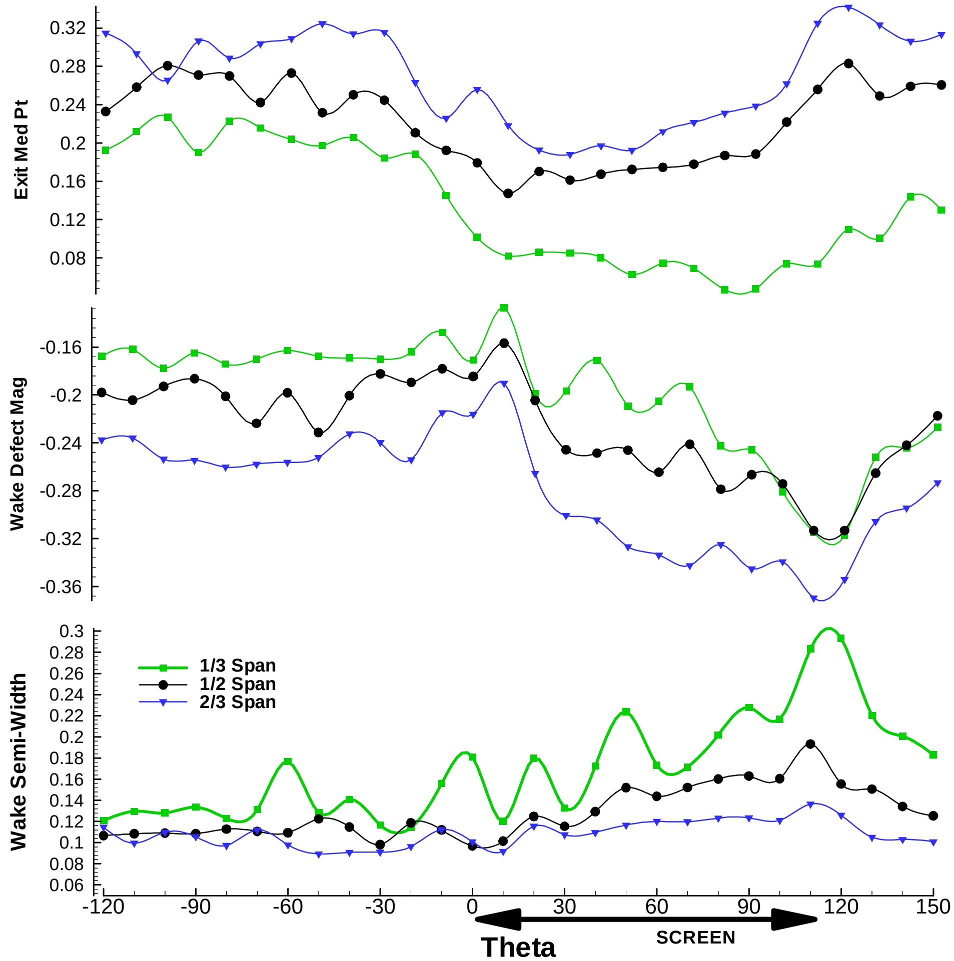

Figure 5.6: Effect of Span on Outlet Parameters (Level 3, OP A)

The exit total pressure increases as the span increases. This may indicate that the tip area puts more work into the flow. All three measurements exhibit the same magnitude of pressure change between the distorted and undistorted regions. The behavior of the wake depth is identical to that of the total pressure considering that wake depth is represented as a deficit in Figure 5.6. The wake width thickens as the span goes from tip to hub, as also seen by Boller (1998). This supports the work of Dancy (1976); he found stall to originate at the hub of these same airfoils of this same test machine. The thicker wake indicates larger, or even unattached, boundary layers. In addition, Figure 5.6 also shows that the change in wake width between the undistorted and distorted regions is greater as the span decreases.

5.3 Effect of Operating Region

The operating region (aerodynamic loading) also affects the inlet and outlet parameters. Figure 5.7 shows the same three inlet parameters plotted versus operating points A, B, and C.

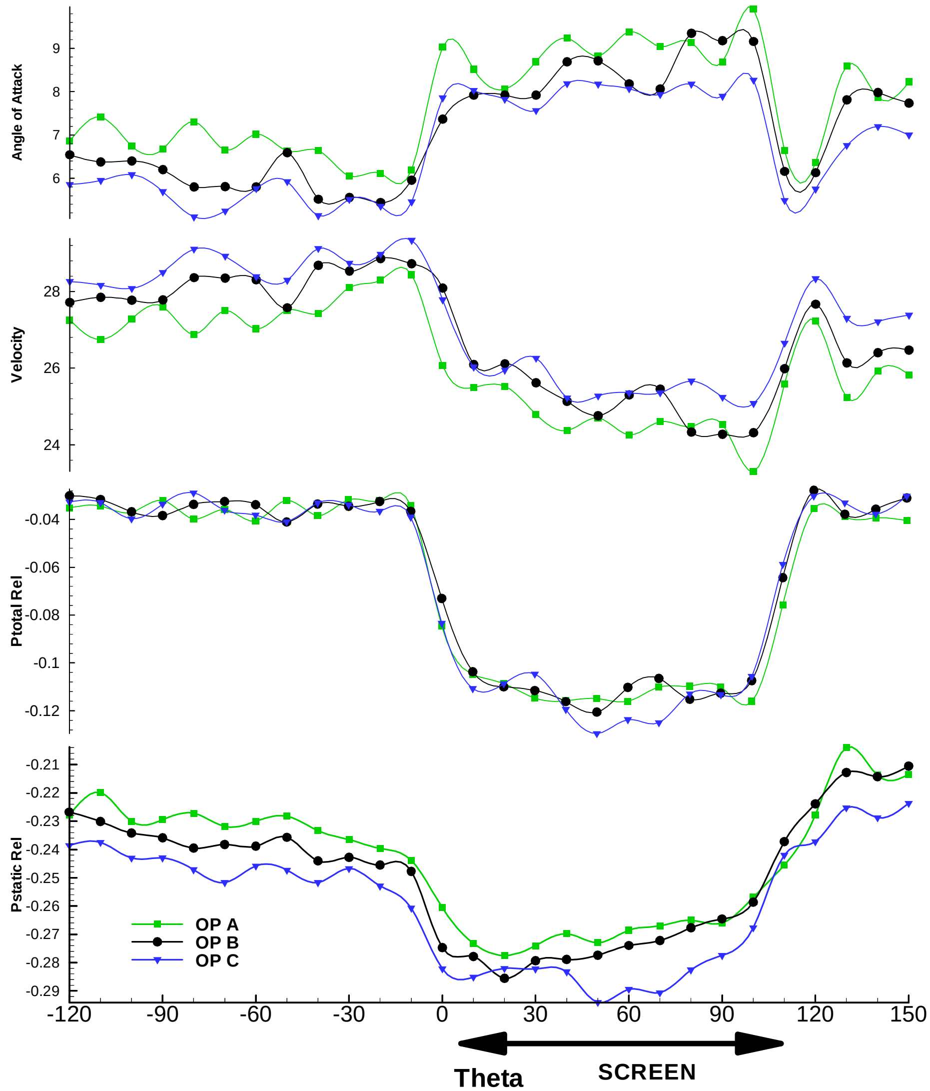

Figure 5.7: Effect of Loading on Inlet Parameters (Level 1, 1/3 Span)

These values correspond to a Level 1 distortion at 1/3 span and represent the typical behavior in regards to aerodynamic loading. The angle of attack increases at higher loading as expected. The inlet velocity decreases as the operating point nears the pre-stall operating region of OP A. This is expected (assuming that this profile is almost identical to that of the axial velocity) since the compressor is operating at a higher pressure rise and reduced mass flow, when referring to the compressor performance characteristic. The total pressure profile tends to not be affected by operating region. However, the static pressure is higher as the loading increases. This change in static pressure, along with an unchanged total pressure, accounts for velocity change when considering the definition of stagnation (total) pressure.

The rotor exit parameters measured at 1/2 span and Level 2 distortion are compared versus operating point in Figure 5.8. This case was chosen for the sake of clarity since a Level 2 distortion only allows for two different operating points.

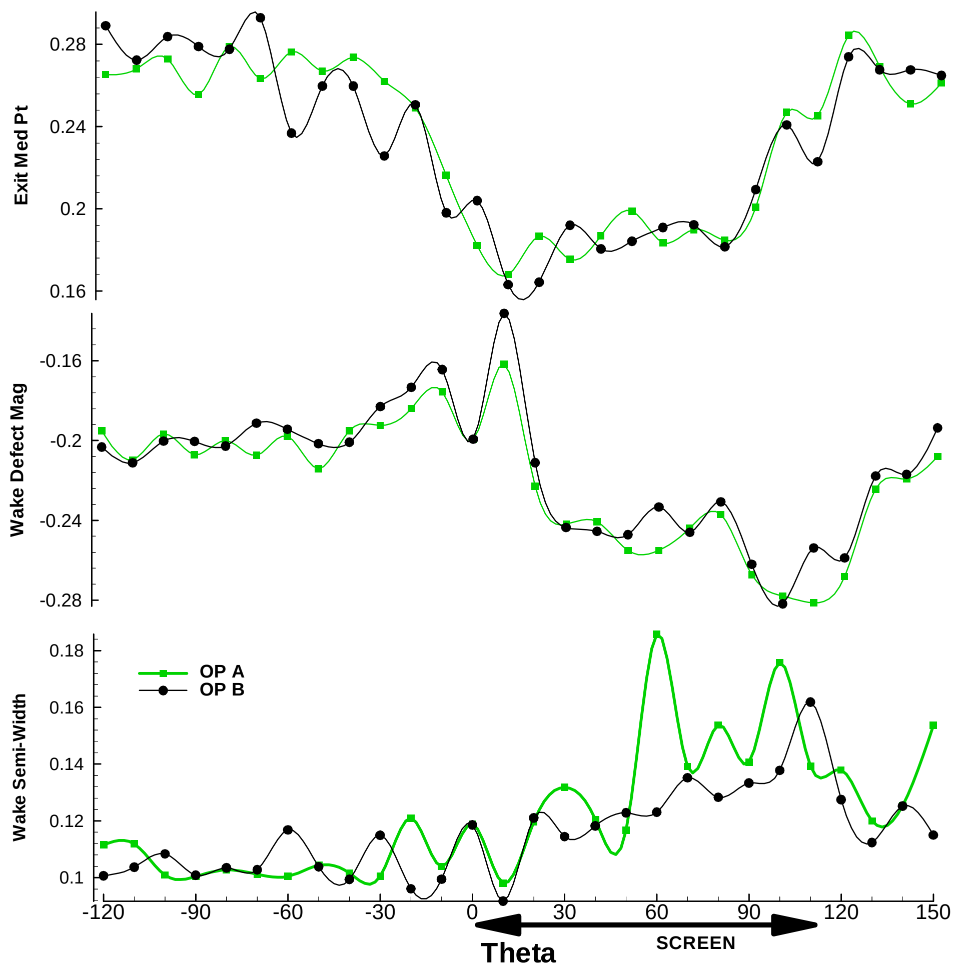

Figure 5.8: Effect of Loading on Outlet Parameters (Level 2, 1/2 Span)

Similar to the inlet total pressure, the exit total pressure is not significantly affected by loading. The wake depth is also seems unaffected. The wake width is larger at higher loadings for some of the cases, as seen above; a trend again noted by Reynolds and Lakshminarayana (1979). However, in this study, this increase in wake width as loading increases did not occur enough to be considered 'typical.' Again, the suction-side jet parameters are not compared versus loading here, since they do not consistently respond to the inlet distortion as mentioned earlier.

5.4 Effect of Distortion Level

The level of distortion has its effects, as well. The inlet parameters for operating point A at 1/2 span are presented versus distortion level in Figure 5.9 below.

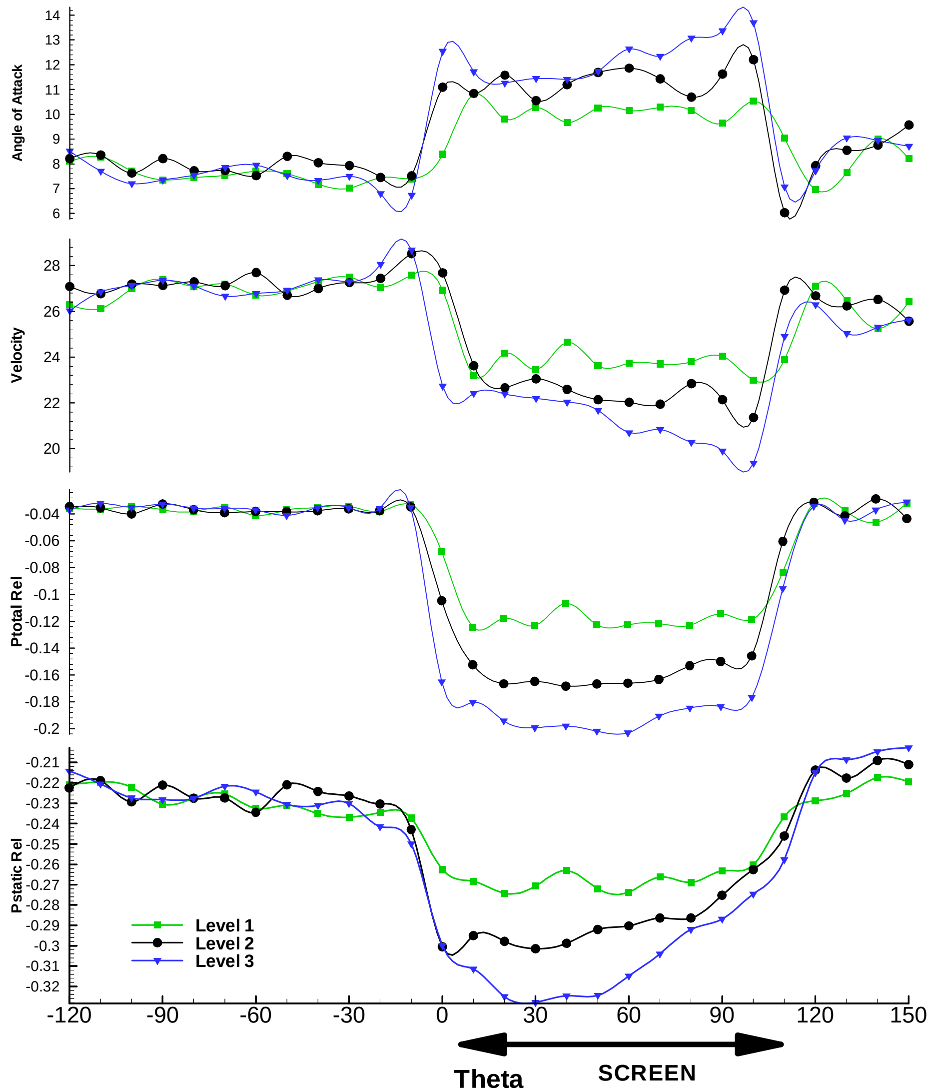

Figure 5.9: Effect of Distortion Level on Inlet Parameters (OP A, 1/2 Span)

As expected, the AOA is higher throughout the distorted region at higher distortion levels due to the decreased axial velocity resulting from the denser mesh of the more intense (higher level) distortion screen. This decrease in velocity can be seen in the graph directly below the angle of attack comparison. The inlet total pressure is much lower in the distorted region of the more intense distortion levels, but is unaffected in the undistorted region. The denser mesh causes a higher loss in total pressure behind the screen. Notice how the profile drops much quicker as the distortion level is increased, almost to the point of a 'square wave' profile. The static pressure profile is identical to that of the total pressure in a qualitative sense.

The outlet parameters for the same OP A and 1/2 span are presented in Figure 5.10.

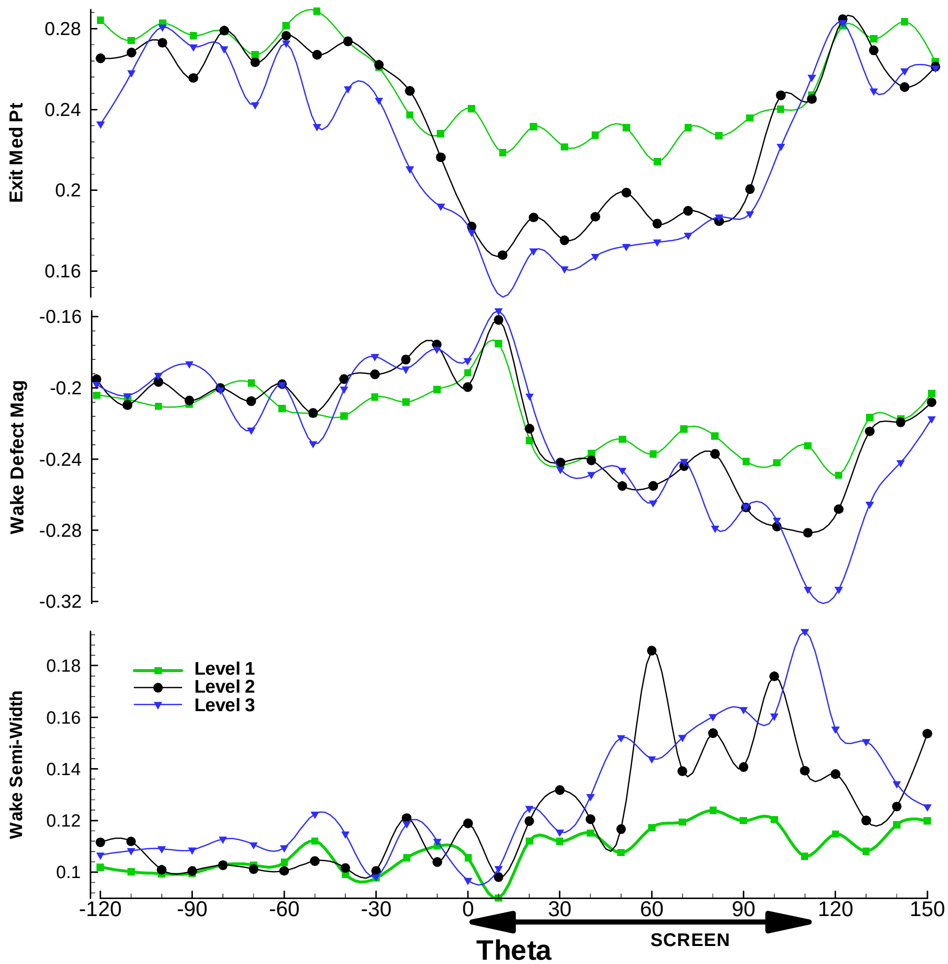

Figure 5.10: Effect of Distortion Level on Outlet Parameters (OP A, 1/2 Span)

The exit total pressure decreases as the distortion level intensifies, as expected. Again, this is due to the denser mesh of the screen. Both the wake depth and width are larger in magnitude in the second half of a higher distortion region. This is caused by the increased angle of attack resulting in a larger overall blade wake, especially in this latter part of the distortion when the exit flow has had more time to respond. Once again, the suction-side jet parameters are neglected here.

5.5 Exit Parameter Time Response

This section compares the response of the exit flow parameters to each of two input drivers (forcing functions). These two input drivers are the inlet parameters: angle of attack (AOA) and inlet total pressure. Cross-correlation coefficients were calculated between each outlet parameter profile versus the two input driver profiles for all eighteen distortion level, operating point, and span combinations. These correlation coefficients are tabulated in Figure 5.11 below.

Correlation Coefficients

Case	Pt vs Pt	Pt vs WD	Pt vs WW	Pt vs JM	Pt vs JW	AOA vs Pt	AOA vs WD	AOA vs WW	AOA vs JM	AOA vs JW
S1A13	0.7590	-0.0222	-0.2693	0.5684	-0.0400	-0.6466	-0.0442	0.2413	-0.5997	0.1012
S1A12	0.8252	0.4647	-0.4143	0.3039	0.2601	-0.7449	-0.3710	0.4216	-0.2733	-0.2522
S1A23	0.7529	0.5301	-0.1453	0.3705	-0.5221	-0.5051	-0.2869	0.1504	-0.4671	0.4818
S1B13	0.7995	0.1542	-0.4912	0.3564	0.1897	-0.6483	-0.3938	0.6408	-0.4636	-0.1969
S1B12	0.8583	0.4137	-0.6020	0.0516	-0.1046	-0.7056	-0.3653	0.6591	-0.1212	0.1432
S1B23	0.8156	0.5278	-0.6240	0.6065	-0.0169	-0.7867	-0.5440	0.6827	-0.6599	-0.0371
S1C13	0.8420	0.2976	-0.3473	0.5849	-0.2703	-0.7203	-0.4566	0.4267	-0.6615	0.1427
S1C12	0.7468	0.6847	-0.5590	0.2891	0.2201	-0.5260	-0.6909	0.6918	-0.2893	-0.2088
S1C23	0.8284	0.6815	-0.6331	0.3902	-0.0417	-0.6476	-0.6135	0.5488	-0.3811	-0.0793
S2A13	0.8734	0.3836	-0.5566	0.7229	-0.4405	-0.7565	-0.4766	0.4919	-0.8278	0.4203
S2A12	0.8844	0.4700	-0.4977	0.3755	-0.0487	-0.7720	-0.3917	0.5376	-0.5499	-0.1060
S2A23	0.8424	0.5589	-0.5623	0.3956	0.0457	-0.7318	-0.4064	0.4861	-0.5725	-0.2515
S2B13	0.9071	0.5378	-0.4009	0.5631	-0.1318	-0.7259	-0.4858	0.4784	-0.6661	0.1668
S2B12	0.8459	0.3979	-0.3467	0.4392	-0.1781	-0.7082	-0.3181	0.2417	-0.6456	0.0041
S2B23	0.8306	0.6676	-0.6185	0.4316	-0.3478	-0.7437	-0.6341	0.6234	-0.4610	0.3196
S3A13	0.8231	0.0949	-0.2122	0.5548	0.1575	-0.7831	-0.1369	0.2351	-0.6413	-0.0209
S3A12	0.8555	0.3035	-0.3726	0.4152	-0.0530	-0.7411	-0.3112	0.3541	-0.5144	0.0892
S3A23	0.8574	0.3907	-0.3831	0.4108	-0.4207	-0.7675	-0.3462	0.2560	-0.3488	0.3298
mean	0.8304	0.4187	-0.4464	0.4350	-0.0968	-0.7034	-0.4041	0.4537	-0.5080	0.0581
median	0.8420	0.4647	-0.4912	0.4108	-0.0530	-0.7318	-0.3938	0.4861	-0.5144	0.0041
std dev	0.0438	0.1977	0.1480	0.1509	0.2322	0.0810	0.1627	0.1740	0.1757	0.2268

Figure 5.11: Correlation Coefficients

The absolute value of the correlation coefficient is of interest here. An absolute value of 1 represents two data sets that are perfectly correlated whereas a value of zero means that there is little or no relation between the two parameters. A negative value usually indicates that one parameter tends to decrease as the other increases or vice versa. The table above shows each individual correlation coefficient as well as the mean, median, and standard deviation of the coefficients for each comparison (i.e. inlet $\underline{P}_t$ vs. <u>W</u>ake

Depth). These 'average' values are a good indication of how related each of the outlet parameters is to each input driver.

As expected, the inlet and outlet total pressure profiles are highly correlated. On the other hand, the suction-side jet width is minimally correlated to both inlet drivers. All other correlation coefficients fall between these two extreme cases. Using Figure 5.11 as a basis, the remainder of this section will look into the time response of each outlet parameter relative to both input drivers, with the exception of jet width and jet magnitude. The jet width is neglected due to its low correlation; the jet magnitude is neglected due to its lack of consistent response despite its relatively good correlation.

Again, plots presented here represent the 'typical' response for all experimental cases. In addition, each parameter has been normalized by its mean value; this normalizing is used later in the investigation and will then be explained further.

5.5.1 Inlet Total Pressure as Input Driver

In this section, each exit parameter will be presented in the order of increasing correlation to the input driver. Figure 5.12 shows a typical plot of outlet total pressure versus inlet total pressure.

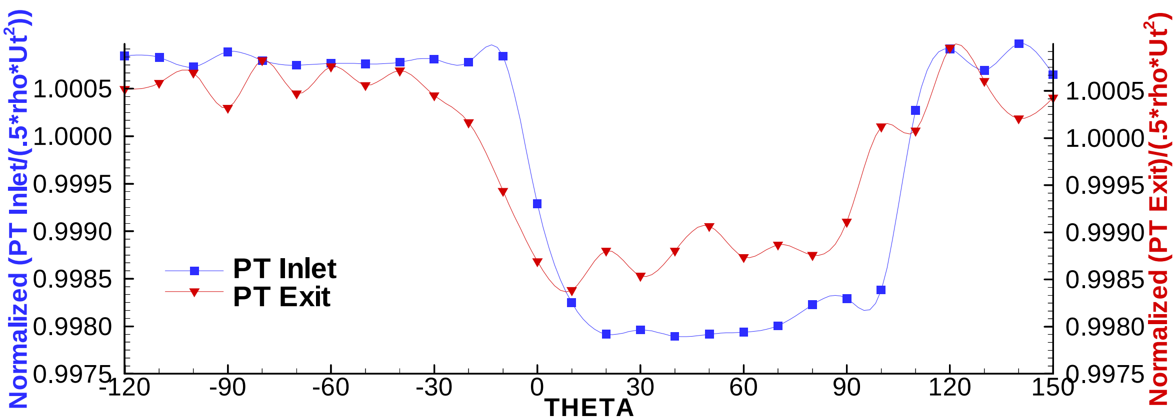

Figure 5.12: Exit Total Pressure vs. Inlet Total Pressure (S2A12)

The mean correlation coefficient for this case is 0.83, highest of all. As mentioned previously, the exit total pressure profile does not drop-off as quickly as the inlet profile. The exit profile for this case leads the inlet by about 20° at the initial drop off as well as at the trailing edge of the distortion. A typical outlet total pressure profile leads at beginning of the distortion, but is almost in phase with the inlet total pressure at the trailing edge of the distorted region.

Wake width has the next highest correlation to the inlet total pressure with an absolute mean value of 0.45. Figure 5.13 shows a response of these two parameters.

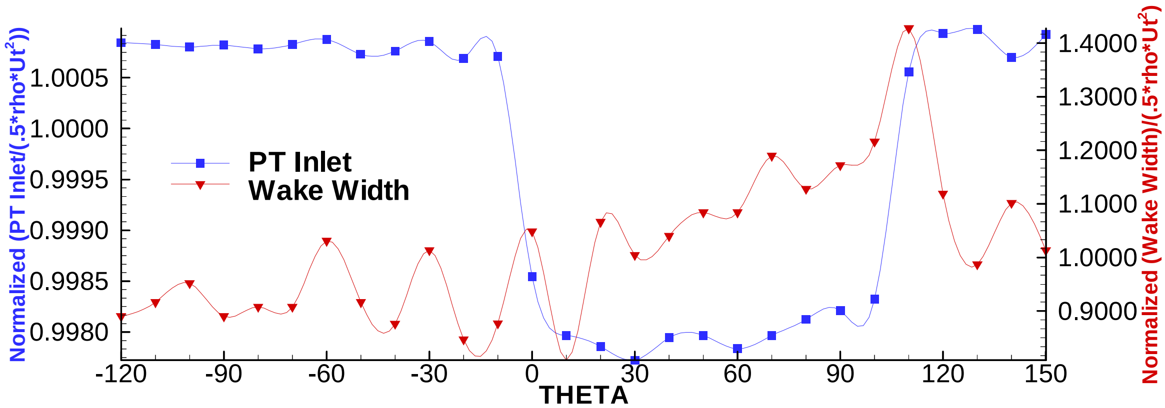

Figure 5.13: Wake Width vs. Inlet Total Pressure (S2B12)

As discussed earlier, the wake width typically dips near the leading edge of the screen and increases throughout the distortion peaking at the trailing edge. The wake width response is in phase with that of the inlet total pressure, hence the relatively high correlation.

With a mean correlation coefficient of 0.42, wake depth is the next highest correlated exit parameter. Figure 5.14 is a plot of wake depth versus inlet total pressure for a typical case.

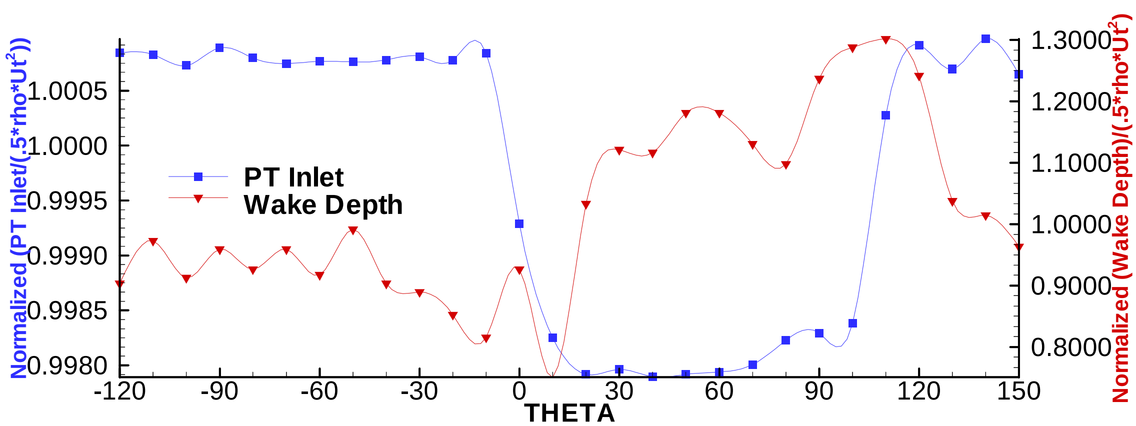

Figure 5.14: Wake Depth vs. Inlet Total Pressure (S2A12)

Notice that the wake depth is shown here as a normalized magnitude rather than a deficit (negative) as before. Similar to the wake width, the magnitude of the wake depth dips at 10°, then increases throughout the distortion ultimately returning to its undistorted value. This response, too, is in phase with the input driver of total pressure.

To summarize, both of the wake parameters increase through the distorted area as expected, and are generally in phase with the inlet total pressure profile. However, sometimes the wake parameters do lag the input driver by 10°, at most, at the leading edge of the distortion. Interestingly, the exit total pressure profile leads the inlet pressure at the leading edge of the distorted region. This may be due to the stagger angle of the blades; since the inlet and outlet instrumentation is aligned circumferentially, the measurements cannot account for the fact that flow (and pressures) travels along the blade (not strictly axial). Therefore, an inlet pressure at 0° is transported along the blade and can be seen at the exit of the rotor at a slightly different circumferential angle. For example, a fluid particle entering the rotor at a circumferential angle of 0° might exit the rotor at a circumferential angle of -10°. Thus the resulting data will show a lead in the exit measurement in the absolute reference frame.

5.5.2 Angle of Attack as Input Driver

In addition to inlet total pressure, it makes physical sense that the angle of attack will influence the exit parameters, especially the wake parameters. The exit total pressure profile was most correlated to the AOA with a mean coefficient of 0.70. Figure 5.15 is a plot of exit total pressure versus AOA.

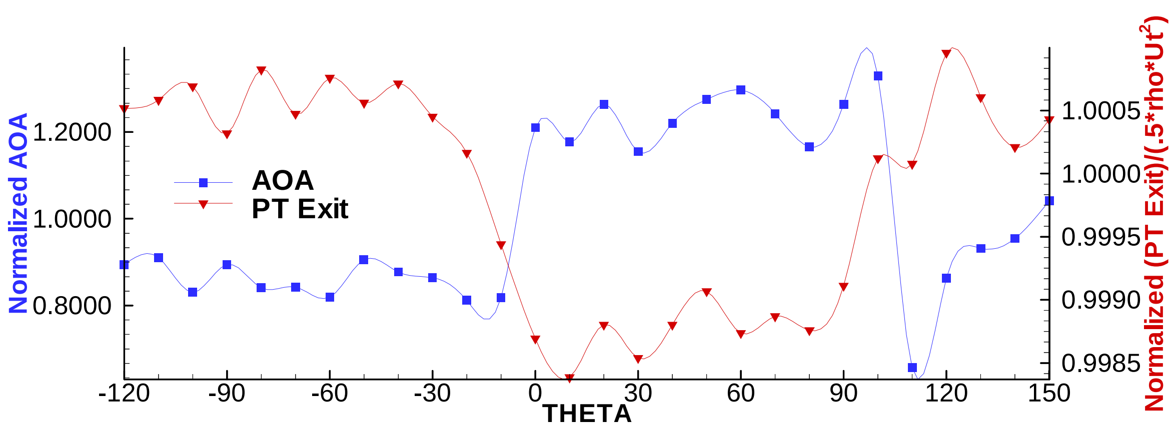

Figure 5.15: Exit Total Pressure vs. AOA (S2A12)

Typically, the exit total pressure begins to drop off ahead of any change in AOA. However, at the trailing edge, the two profiles are closer to being in phase. This is similar to its response to the inlet total pressure. Again, this is typical for all eighteen cases in this study.

The parameter with the next highest correlation to AOA is the wake width. This physically makes sense; as the AOA increases, the wake width should increase closely in phase. The mean correlation coefficient here is 0.45. Howard (1999) found the relationship of wake width versus AOA of his data set to be highly correlated as well. Figure 5.16 shows this relationship for the present data set.

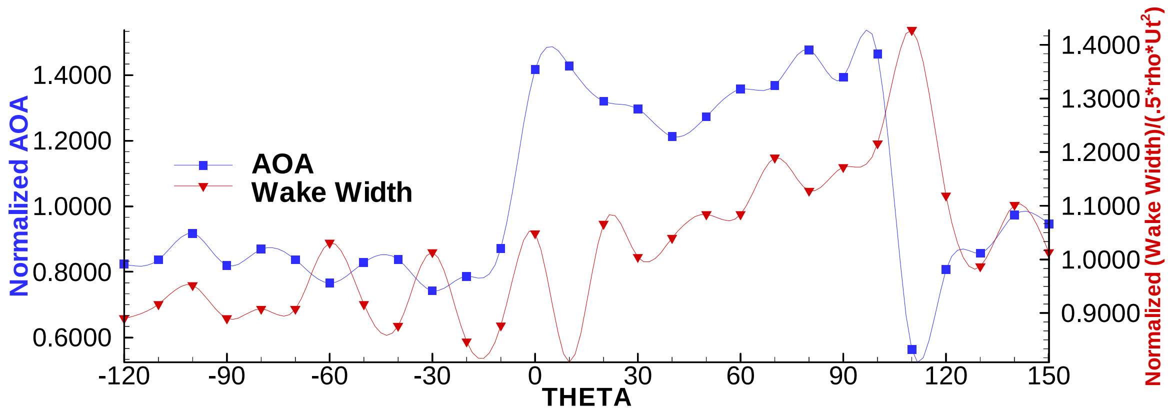

Figure 5.16: Wake Width vs. AOA (S2B12)

Again, the wake width is slightly lagging the input driver (by 10° at most), just as it does the inlet total pressure. This must represent the time needed for the blade wake to respond to the change in angle of attack. Although some cases show the two responses to be in phase, typically this lag exists.

As expected, the wake depth is not far behind the wake width as far as correlation is concerned. Its mean correlation coefficient is 0.40. Figure 5.17 shows a typical response of the wake depth relative to the angle of attack.

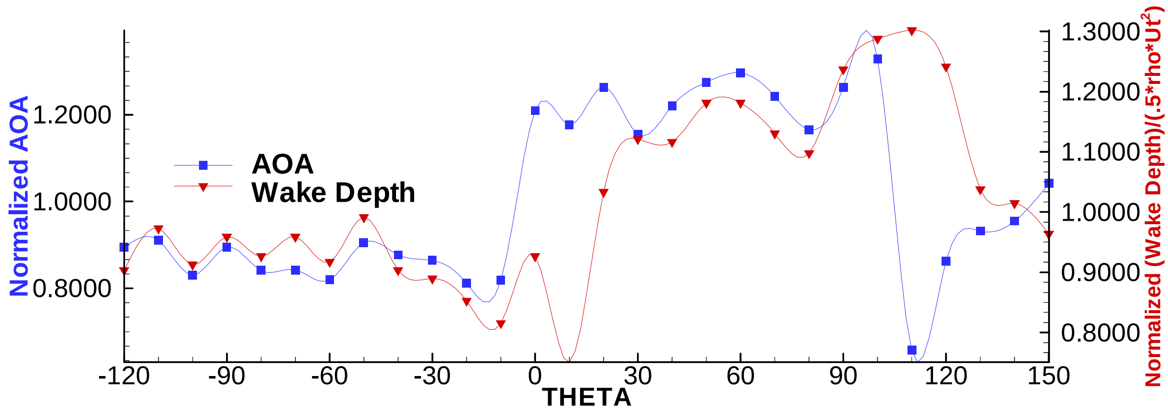

Figure 5.17: Wake Depth vs. AOA (S2A12)

Again, note that the wake depth appears as a magnitude rather than a deficit due to the normalization. As expected, the wake depth lags the AOA just as the wake width does. In this particular case, the lag is about 20°. This lag exists at both the leading a trailing edges of the distortion. A lag of 10° to 20° is typical for the entire data set. Again, this represents the time needed for the wake to respond to the change in AOA values.

To summarize, the response of these exit flow parameters to AOA is similar to the response to the inlet total pressure profile. The wake parameters lag the AOA both at the leading and trailing edges of the distorted region. The exit total pressure leads the AOA at the leading edge of the distortion, but then becomes almost in phase with the input driver near the trailing edge of the screen. However, the wake parameters tend to lag the AOA more than they do the inlet total pressure. This is due to the fact that pressure information is transported through the blade row at the speed of sound, while the AOA information moves through the blade row at the speed of convection. Therefore, the response of any exit flow parameter to a change in pressure is going to be quicker than its response to a change in AOA, as seen in the data.

5.6 Inlet and Exit Flow Parameters vs. Machine Speed

5.6.1 Inlet Flow Parameters vs. Machine Speed

Having two data sets from the same machine at different speeds allows for the comparison of the inlet and exit flow parameters versus machine speed. The machine was run at 2580 rpm (referred to as 2600 rpm for convenience) for the present investigation; this is roughly a 23% increase in speed from the 2100 rpm that Boller used.

All parameters presented in this section are non-dimensionalized as outlined in Section 4.6. It is important to keep in mind that the operating points of the present study do not necessarily correspond to those of the Boller work (i.e. the non-dimensional pressure rise and mass flow are not necessarily the same). Therefore this section will be more of a qualitative comparison than a quantitative comparison; although, quantitative relationships will be noted when possible.

First, the angle of attack profiles will be compared. Figure 5.18 shows the AOA profiles for both speeds for four different measurement cases.

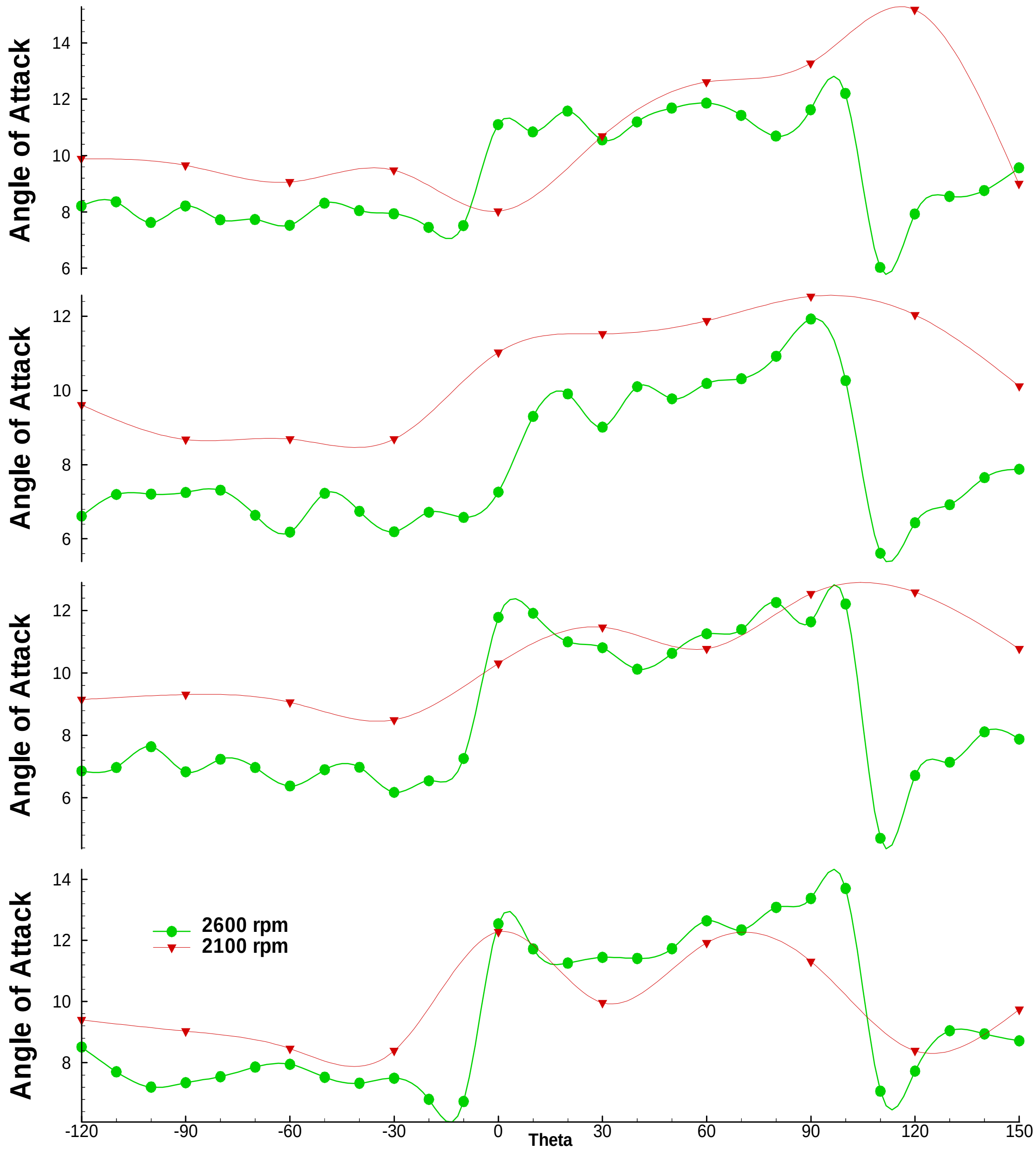

Figure 5.18: AOA vs. Machine Speed

The higher inlet measurement resolution in the circumferential direction is quite evident here. The present set of data seems to be more accurate in capturing what exactly is going on near the edges of the distortion. This is evident for all of the inlet parameters, as can be seen later in this section. The cases presented in Figure 5.18 are: (from top to bottom) S1B12, S2A12, S2B12, and S3A12. This gives a variety of different distortion levels and operating points. It is obvious that the AOA increases in the distorted region for both speeds as expected. It is evident that the AOA in the undistorted region is higher for the lower speed. This may be due to a smaller axial velocity ratio (C_z/U) therefore causing the relative flow angle to increase. The AOA values converge on each other through the distorted region, often exceeding the steady-state stalling angle as mentioned previously in this chapter. It is difficult to compare the phase of the two profiles due to the lack of resolution in the 2100 rpm inlet data.

The lack of inlet measurement resolution is also evident in the pressure profiles, especially the total pressure. Figure 5.19 shows the inlet total and static pressure profiles for both speeds (S1B12). This plot is typical for most cases although some cases show a phase shift. It is the opinion of the author that these apparent phase shifts are inaccurate due to the lack of inlet measurement resolution in the 2100 rpm data.

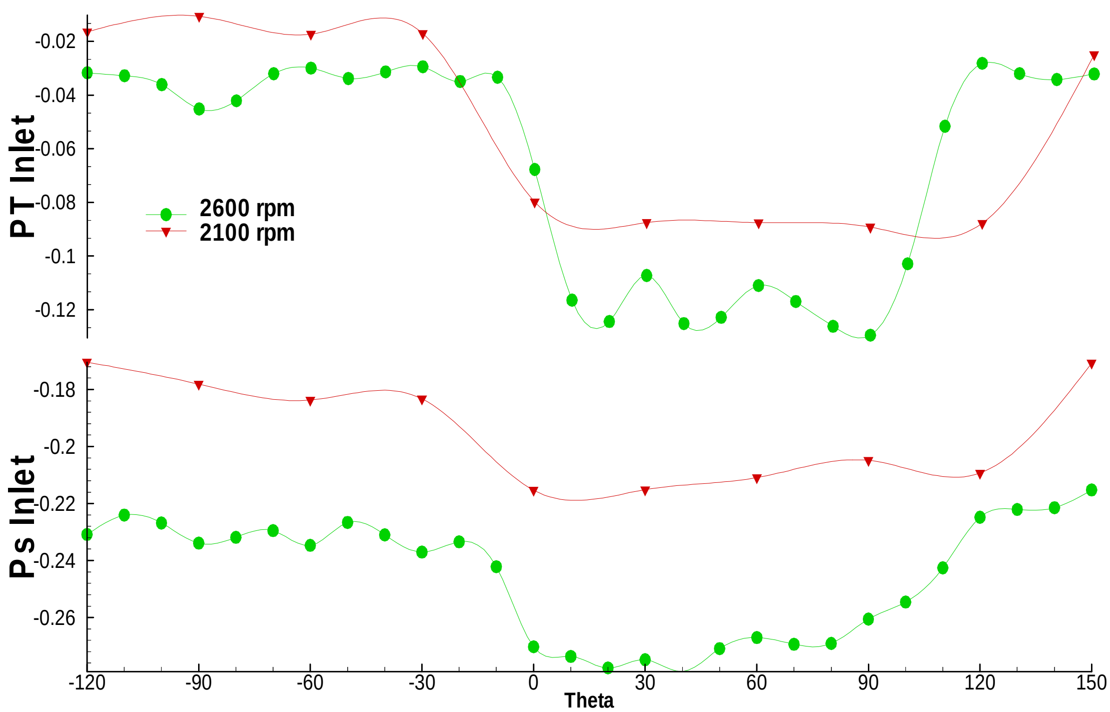

Figure 5.19: Inlet Total Pressure vs. Machine Speed (S1B12)

The total pressure loss is less at the lower speed. This is due to the lower axial velocity which results in less total pressure distortion by both the support mesh (in the undistorted region) and the distortion screen. The higher resolution of the 2600 rpm data gives a better idea as to where the screen and resulting distortion is located. Since the static pressure does not drop off as quickly, there is little difference in the static pressure profiles in regard to machine speed. The larger difference in values between the two static pressures (relative to the difference in total pressures) accounts for the larger velocity at higher machine speed (when using the definition of total pressure to find velocity). Again, it is difficult to make any phase comparisons here.

5.6.2 Exit Flow Parameters vs. Machine Speed

Figure 5.20 shows a typical case for all exit flow parameters versus machine speed. The exit total pressure profiles are very similar both qualitatively and quantitatively.

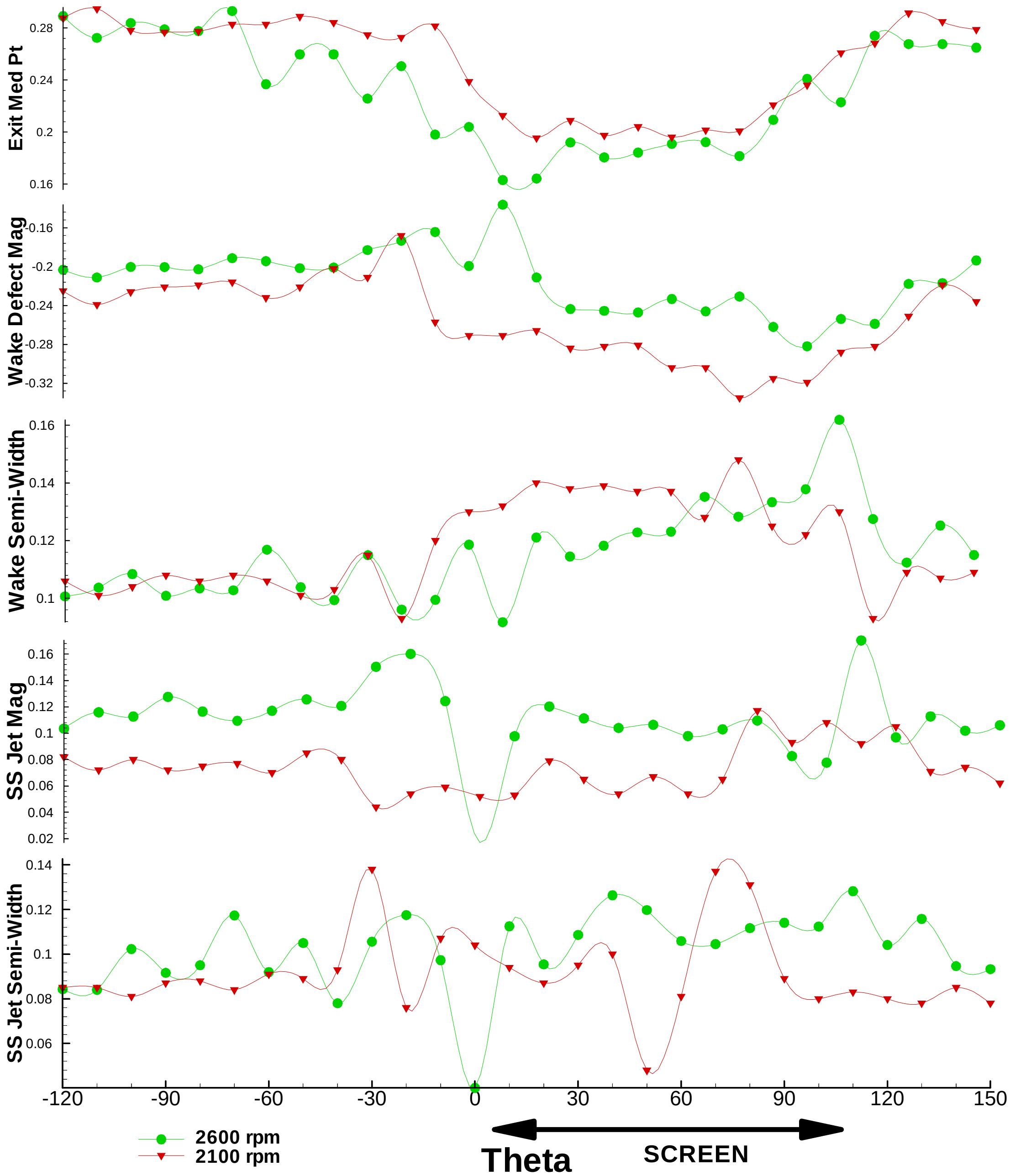

Figure 5.20: Exit Flow Parameters vs. Machine Speed (S2B12)

Total pressure is related to velocity through a square law. Therefore, a 23% increase in machine speed would ideally create about a 50% increase in pressure rise due to this relationship. Since the total pressures are non-dimensionalized by the one-half the density multiplied by the tip speed squared (also a square law), it makes sense that the two profiles lie near each other. In addition, the non-dimensionalized exit total pressure at the higher speed is expected to be smaller due to higher total pressure losses associated with higher speed flows. This is evident in Figure 5.20; the 2600 rpm profile is slightly smaller throughout. The higher speed profile also seems to lead the lower speed profile. This may be due to the stagger angle effect discussed in the previous section; now that the flow speed in higher, the lower (distorted) pressure region in front of the rotor will be seen behind the rotor in a shorter amount of time (smaller fluid transport time).

The wake depth and width for both speeds behave similarly as expected. However, the lower speed profile leads that of the higher speed for both parameters. In addition, a quantitative comparison can be made. When converting the wake parameters to absolute quantities, the wake depth is larger in magnitude at the higher speed, and the wake width is smaller for the higher speed flow. This was also noted by Lakshminarayana et al. (1981). As the flow velocity over a blade increases, the wake thins and elongates.

Only one thing can be concluded about the suction-side jet parameters besides the fact that they fluctuate greatly. The jet magnitude is greater for the higher speed flow. This may be a mass-conservation effect to make up for the longer wake associated with higher speed flow. In addition, the higher frequency data acquisition may contribute to this. The higher sampling rate captures more of the 'extreme' values of jet peaks, therefore increasing the jet magnitude calculation. This effect may also contribute slightly to the wake depth increase as the speed increases as discussed in the previous paragraph.

To summarize, there are some differences in the parameters relative to machine speed. Due to the lack of inlet measurement resolution, it is difficult to draw solid conclusions about these differences, especially in time response (phase comparisons).

For convenience, the list below highlights the differences between the data trends seen in this experiment and those seen by Boller (1998). It can be assumed that all other trends noted in the current investigation were also observed by Boller.

- Inlet total pressure was unaffected by changes in span and loading in this investigation; however, Boller found the inlet total pressure loss to be smallest at midspan and at higher loadings.
- The wake depth was unaffected by loading in this investigation; however, Boller observed a larger wake depth at higher loadings.

6 Frequency Response Function Analysis of Rotor Response Data

With this new collection of inlet distortion rotor response data, it was desired to create a better method for modeling dynamic blade row response through the use of frequency response functions; this would then lead to an initial attempt in predicting dynamic stage characteristics. This section introduces the mathematics and theory behind frequency response functions (FRF), primarily as described by Howard (1999). Then, the FRF analysis and its proposed application to predicting dynamic stage characteristics are presented. Finally, the prediction results are presented and evaluated.

6.1 Frequency Response Functions

Frequency response functions, as defined below, are only applicable to linear systems. Therefore, the dynamic blade response is assumed to be linear for small changes in operating region, thus allowing the input (forcing function) to be transformed into a Fourier series which, when multiplied by a frequency response function, gives the dynamic response. This is an over-simplification since fluid mechanics are non-linear in nature, thus making the dynamic response of a mechanical/fluid system non-linear. However, all physical systems exhibit some degree of non-linearity, but can often be approximated as linear.

The frequency response function is defined as the Fourier transform of the response function divided by the Fourier transform of the forcing function. Therefore, all that is needed to model the blade frequency response is the time-domain representations of both the forcing function and response function. Once the frequency response function is created, it can be used to predict the response of any forcing function. To do this, the forcing function must be transformed into the frequency domain, then multiplied by the FRF giving the response function in the frequency domain. An inverse Fourier transform then converts the response function from the frequency domain, back into the time domain representing the system (blade) time response. Equation 6.1 defines the FRF as

$$FRF = \frac{RF}{FF} \qquad \textbf{Equation 6.1}$$

where RF is the Fourier series of the response function and FF is the Fourier series of the forcing function.

Equation 6.2 shows a continuous Fourier series FRF as typically defined in textbooks.

$$FRF = \frac{\int_{-\infty}^{\infty} f(t)_{RF} \cdot e^{-i\omega t}\, dt}{\int_{-\infty}^{\infty} f(t)_{FF} \cdot e^{-i\omega t}\, dt}$$ **Equation 6.2**

The continuous time series can be discretized into N number of data samples resulting in the discrete Fourier transform as shown in Equation 6.3.

$$F_m = \sum_{k=0}^{N-1} f_k e^{-i(2\pi mk/N)} \qquad m = 0,1,\ldots,\frac{N}{2}$$ **Equation 6.3**

Using equation 6.3, equation 6.2 can now be written as

$$FRF = \frac{\sum_{k=0}^{N-1} f_{kRF} e^{-i(2\pi mk/N)}}{\sum_{k=0}^{N-1} f_{kFF} e^{-i(2\pi mk/N)}} \qquad m = 0,1,\ldots,\frac{N}{2}$$ **Equation 6.4**

to give an equation that can be applied to the inherently discrete experimental data.

Equation 6.4 can be broken down into real and imaginary components:

$$F_m = \sum_{k=0}^{N-1} f_k \cos\left(\frac{2\pi m}{N} k\right) - i \sum_{k=0}^{N-1} f_k \sin\left(\frac{2\pi m}{N} k\right) \qquad m = 0,1,\ldots,\frac{N}{2}$$ **Equation 6.5**

This imaginary component carries the phase information that is crucial to the time response. Equation 6.5 shows that the real and imaginary parts are the sum of all the data samples multiplied by a cosine term for the real component, and multiplied by a sine term for the imaginary component. Each sequence has a period of N/m data samples. This gives the magnitude of the real and imaginary components at each frequency. The real component is represented by a_m and the imaginary component is represented by b_m.

Equations 6.6 and 6.7 define a_m and b_m.

$$a_m = \sum_{k=0}^{N-1} f_k \cos\left(\frac{2\pi m}{N} k\right) \qquad m = 0,1,\ldots,\frac{N}{2}$$ **Equation 6.6**

$$b_m = -i\sum_{k=0}^{N-1} f_k \sin\left(\frac{2\pi m}{N} k\right) \qquad m = 0,1,\ldots,\frac{N}{2}$$ **Equation 6.7**

Now that the Fourier series is broken down into its real and imaginary components, the FRF can now be calculated using the magnitude and phase of the forcing and response functions. The real and imaginary components at each frequency are transformed from a Cartesian coordinate system into a polar coordinate system. Then a useful FRF can be created by dividing the magnitudes and subtracting the phase angles.

Magnitude $$M = \left[(a_m)^2 + (b_m)^2\right]^{\frac{1}{2}}$$ **Equation 6.8**

Phase Angle $$\Phi = \tan^{-1}\left(\frac{b_m}{a_m}\right)$$ **Equation 6.9**

$$FRF = \frac{M_{RF} \cdot \Phi_{RF}}{M_{FF} \cdot \Phi_{FF}}$$ **Equation 6.10**

$$M_{FRF} = \frac{M_{RF}}{M_{FF}}$$ **Equation 6.11**

$$\Phi_{FRF} = \Phi_{RF} - \Phi_{FF}$$ **Equation 6.12**

The FRF's used in this study are calculated by a Fortran 90 code developed by Howard (1999); the code uses Equation 6.4 and Equations 6.8 through 6.12.

As mentioned, the use of a frequency response function is only appropriate if the system behavior is linear. Therefore, the frequency response function method can only accurately describe the dynamic response if the blade response is linear or has non-linear dynamic departures that are of small magnitude.

It is assumed in this analysis that the inlet and exit parameter profiles represent responses in the time domain (due to the blade rotation) allowing them to be viewed as a forcing function and response function, respectively. Furthermore, it is assumed that the blade response is nearly linear for small changes in operating point, and that the FRF is general enough to be applied to dynamic distortions (forcing functions) other than the one from which it was derived. Howard (1999) showed that distortion frequency and intensity do not affect the resulting FRF.

6.2 Predicting Rotor Response and Dynamic Stage Characteristics

This section will outline the successful use of frequency response functions to predict the exit total pressure profile behind the rotor. Furthermore, it will be shown how these predicted rotor exit total pressure profiles were used in an attempt to predict dynamic stage characteristics.

A stage characteristic is essentially composed of a series of pressure rise and mass flow values. Each value of mass flow through the compressor results in a certain pressure rise; this pressure rise is ultimately referred to as the performance. Figure 4.18 back in Section 4.5 is an example of a type of stage characteristic. In this case, it is the characteristic for the isolated rotor used in the experimental investigation.

An ideal method for predicting dynamic stage characteristics would require nothing more than the changing of a few input parameters while yielding excellent predictions for any compressor configuration, exposed to any inlet condition/distortion. Unfortunately, a model like this is does not exist. However, the method attempted in this study is a step in the right direction.

The idea behind this proposed method of dynamic stage characteristic prediction is quite simple. Using frequency response functions developed from experimental data, the dynamic total pressure profile at the exit of the rotor can be predicted. This total pressure profile is then weighted with the corresponding mass flow to ultimately predict the mixed-out total pressure rise (plenum pressure) of the machine.

To accomplish this, minimal experimental data is required. Obviously, inlet and exit total pressure circumferential profile data is needed to create the FRF's; a unique

FRF is needed for airfoil shape and operating region. Once the required FRF's are created, dynamic (distorted) stage characteristics can be predicted by this method, given an inlet total and static pressure profile as an input. The inlet pressure profiles can be tailored to represent many different distortion patterns, thus allowing the prediction of dynamic stage characteristics for many different inlet conditions.

The present study has succeeded in accurately predicting the rotor exit total pressure profile. However, the attempt at predicting the dynamic stage characteristics of the test machine was not as successful, but does show some potential. Although not fully successful, it is believed that this attempted method can be extended further to accomplish what is described in the two preceding paragraphs with accuracy. The remainder of this section will discuss the details of the method as it exists, as well as the results.

6.2.1 Choosing the Forcing Function

To create a frequency response function, both a forcing function and a response function are needed. Since the immediate goal is to predict the exit total pressure, it obviously makes sense to use the exit total pressure as the response function when creating the FRF's. As for the forcing function, there were a couple of possible choices.

Looking at the inlet parameters discussed in Section 5, both angle of attack (AOA) and inlet total pressure seemed to be legitimate candidates when considering the physics of the blade row. The inlet total pressure circumferential profile is obviously going to have a sizable effect on the exit total pressure profile. Any relatively low or higher pressure regions are going to pass through the blade row to some degree causing corresponding low and high exit pressure regions. The AOA affects the exit total pressure also; if angle of attack becomes too high or too low, the blade row will not be able to create an appreciable pressure rise.

Referring back to the table of correlation coefficients in Figure 5.11 in Section 5.5, the mean coefficient for inlet total pressure versus exit total pressure was 0.83 while the mean coefficient for AOA versus exit total pressure was 0.70. These were the two most highly correlated relationships. Since they were so much higher than all others, it was decided to initially create frequency response functions for both relationships.

6.2.2 Typical Frequency Response Function

Frequency response functions were created for both AOA versus exit P_t and for inlet P_t versus exit P_t from the experimental data for all eighteen combinations of operating point, distortion level, and measurement span. Since the data sets only covered a 270° profile, there was an 80° extent where the data was 'padded' with a linear fit between the first (θ=-120°) and last (θ=150°) values of each parameter to provide periodicity. These fits were all within the calculated margin of error for the data. In addition, each parameter was normalized by its average value. This was done so that the calculated FRF's could be applied to any inlet or outlet parameter through the use of a scaling factor. Equation 6.13 shows this mathematically where C is the scaling factor.

$$RF(\omega) = FF(\omega) \cdot C \cdot FRF(\omega) \qquad \textbf{Equation 6.13}$$

Figure 6.1 shows a typical magnitude and phase plot for an FRF created from the AOA versus exit total pressure relationship. Please keep in mind that the peaks associated with the spline fits in these graphs do not necessarily represent real data points.

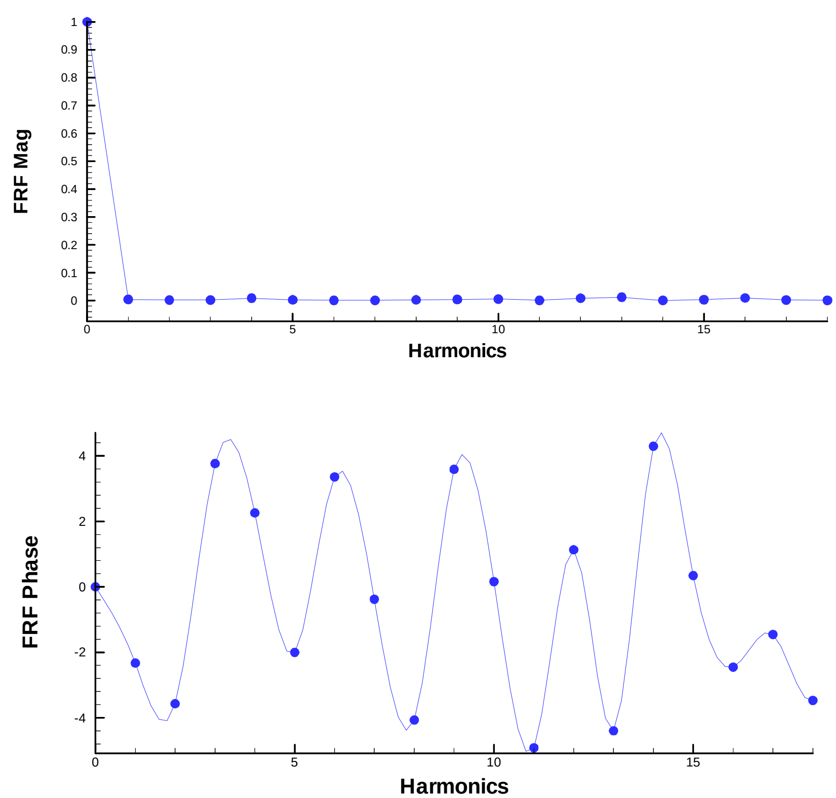

Figure 6.1: Typical FRF for AOA vs. Exit Total Pressure (S1B13)

The magnitude plot is very typical for this inlet/exit relationship; the gain is very small at all frequencies except at zero where it is equal to one, as is the case for all of these FRF's due to the normalizing. The first five or six harmonics of the phase are very typical for this case as well. At higher frequencies, the phase varies more with different data sets. Figure 6.2 shows the typical FRF for inlet total pressure versus exit total pressure.

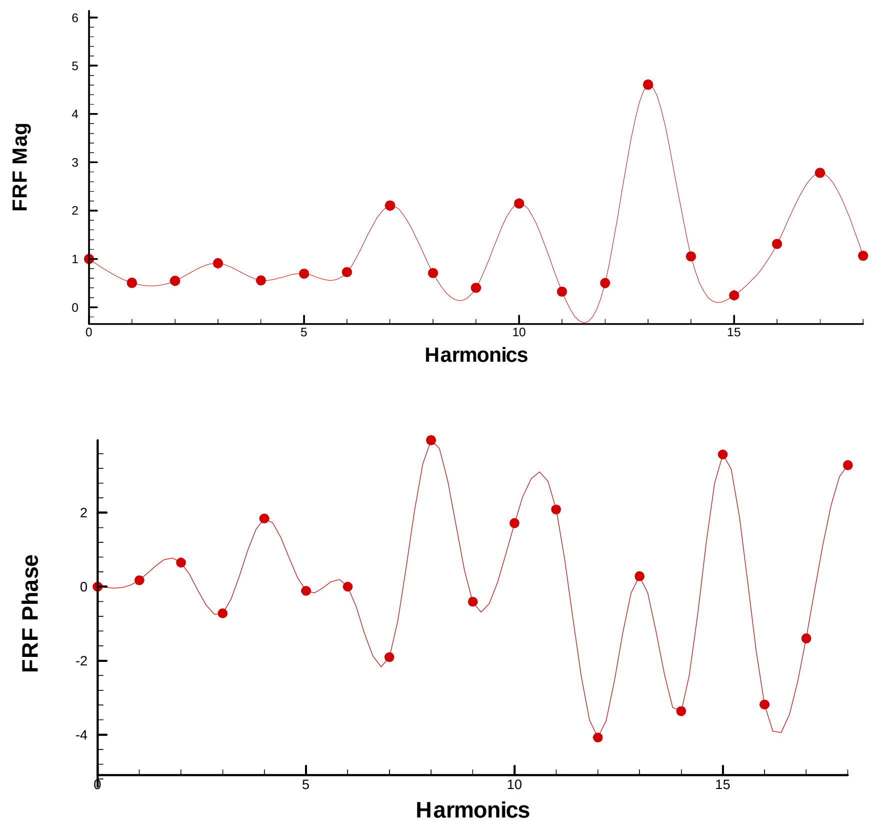

Figure 6.2: Typical FRF for Inlet P_t vs. Exit P_t (S2B23)

For these two parameters, it is common to see peaks in magnitude at harmonic 7, 10, 13, and 17 as seen in Figure 6.2. Again, the phase shown here is fairly typical for the first five or six harmonics, but then it varies more with changing data sets. The FRF's derived for this relationship are presented in Appendix B.

6.2.3 Creating the 'Generalized' Frequency Response Functions

Between these two inlet/exit parameter relationships, there resulted thirty-six different frequency response functions. This number had to be reduced in order make this new method feasible.

Ideally, there would exist one 'generalized' FRF for each inlet/exit parameter relationship that would characterize the response of the blade row for all operating points, distortion intensities, and measurement spans. A good way to create such an FRF is through averaging. At each frequency, both the magnitude and phase was arithmetically averaged to form the 'generalized' frequency response function.

In order to average in the frequency domain, the time samples of each parameter must be stationary and ergodic. A stationary process is one in which statistical quantities (i.e. mean value) computed for one sample function (data set) do not vary from data set to data set. These quantities are said to be representative of any other sample function of that particular process. Stationary processes are usually ergodic, meaning that statistical quantities, computed for a certain part a sample function (from t_1 to t_n), are representative of those computed for the whole sample function. With these definitions in mind, it was concluded that the inlet and exit parameters were both stationary and ergodic. The data is stationary, in that the screen is always located in the same place (0° to 110°) producing the same type of behavior in each parameter. The data is ergodic due to its periodicity. Therefore, averaging the frequency response functions is legitimate for the purposes of this study.

There are going to be some compromises in both magnitude and phase when averaging in the frequency domain. Therefore, it was decided to create 'generalized' FRF's for common spans, operating regions, and distortion intensities in addition to the overall averaged FRF. This was done to minimize these losses associated with the averaging process; limiting the number of cases averaged increased the chances of retaining the important magnitude and phase information. It also made sense physically; the physics of the process change slightly when the operating point, distortion intensity, and/or measurement span change.

It is interesting to see how the 'generalized' FRF's for both AOA versus exit P_t, and inlet P_t versus exit P_t, all collapse on one another independent of the averaging scheme (common span, load, etc.). Figure 6.3 shows the magnitudes of the 'common span' generalized FRF's for AOA versus exit P_t.

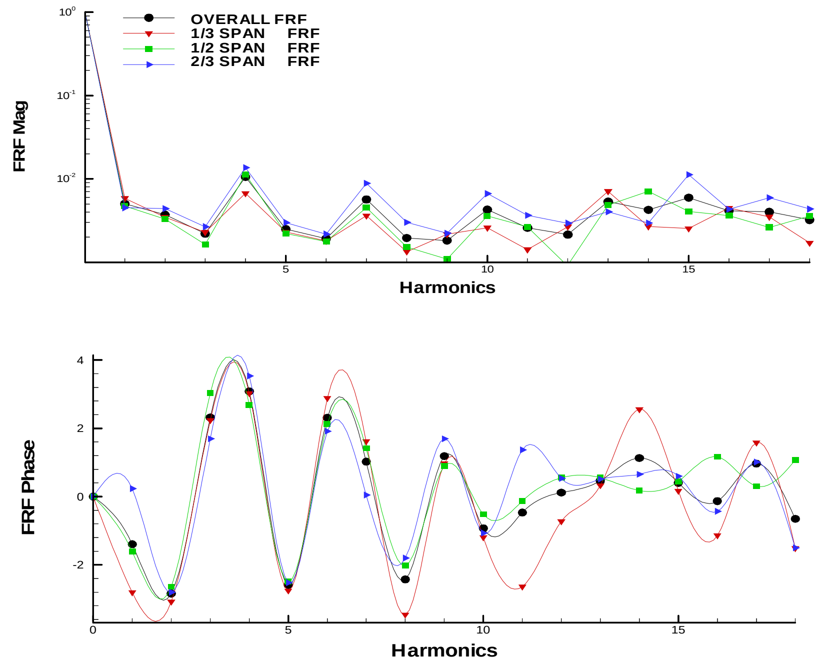

Figure 6.3: Common-Span Generalized FRF for AOA vs. Exit P_t

The magnitude here is plotted on a log scale due to the very small values. It is evident that both the magnitude and phase collapsed on each other, especially for the first ten or so harmonics. This is also evident for the 'common loading' FRF's as shown in Figure 6.4. The same effect is evident in the 'common level' FRF's, which are not shown.

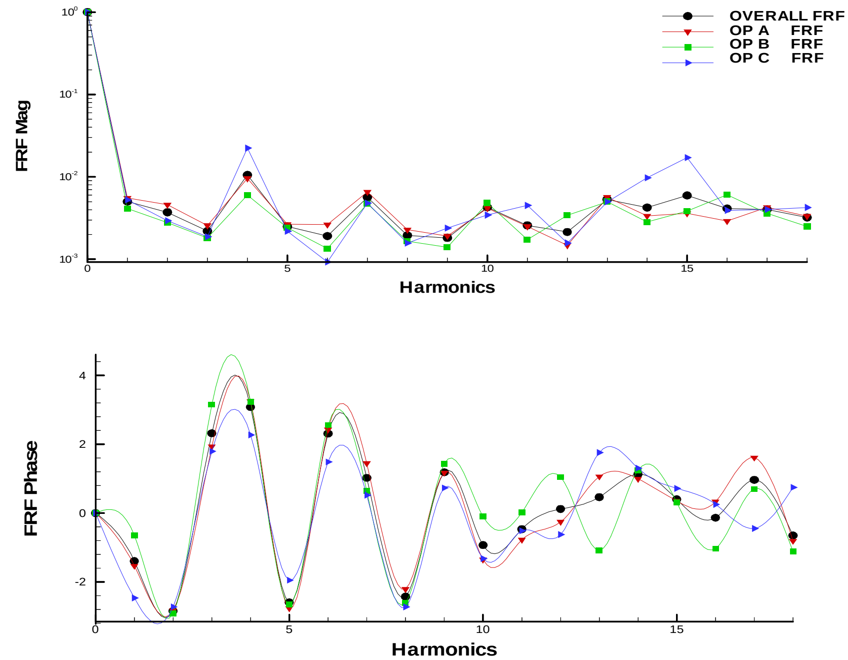

Figure 6.4: Common-Loading Generalized FRF for AOA vs. Exit P_t

The generalized frequency response functions for inlet total pressure versus exit total pressure are also very intriguing in the way that they collapse onto each other. Figures 6.5, 6.6, and 6.7 show the common span, loading, and distortion level generalized FRF's respectively.

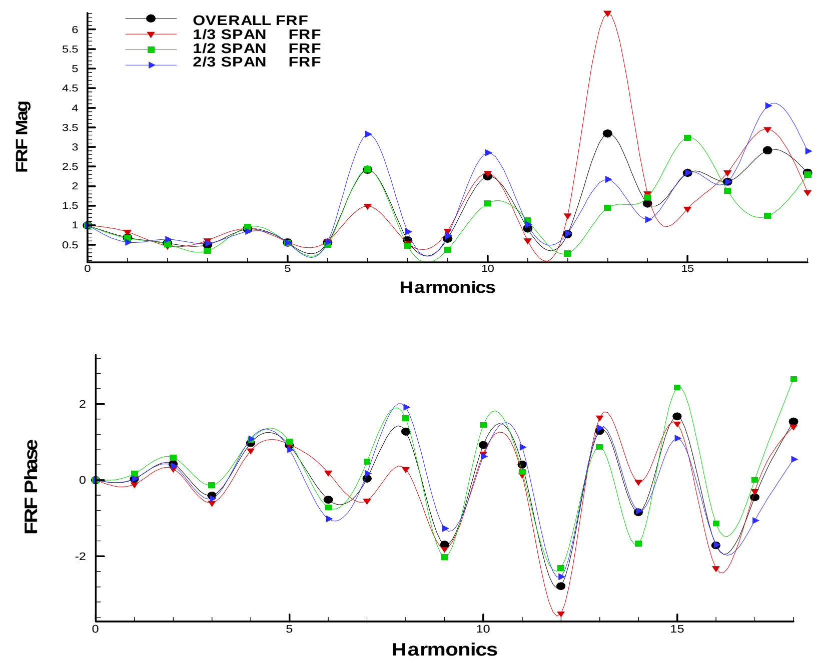

Figure 6.5: Common-Span Generalized FRF for Inlet P_t vs. Exit P_t

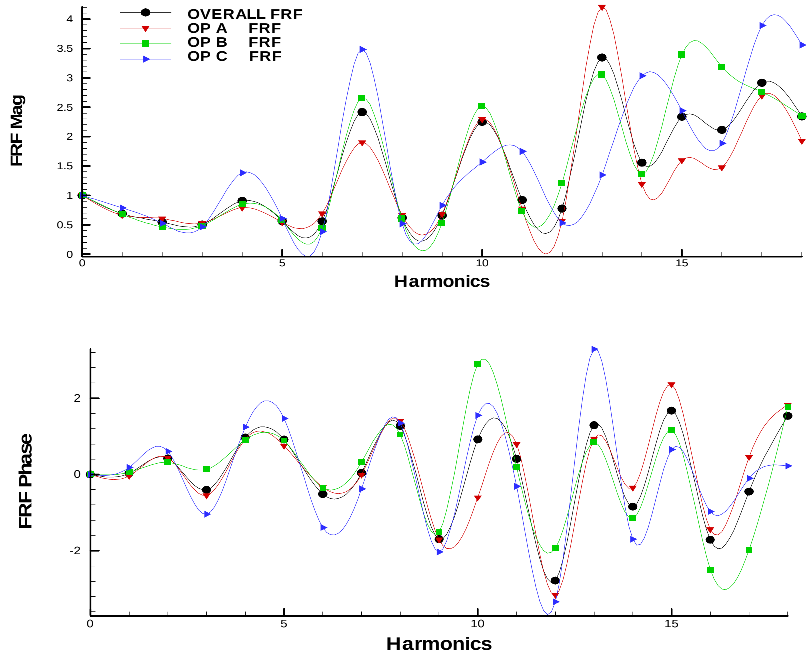

Figure 6.6: Common-Loading Generalized FRF for Inlet P_t vs. Exit P_t

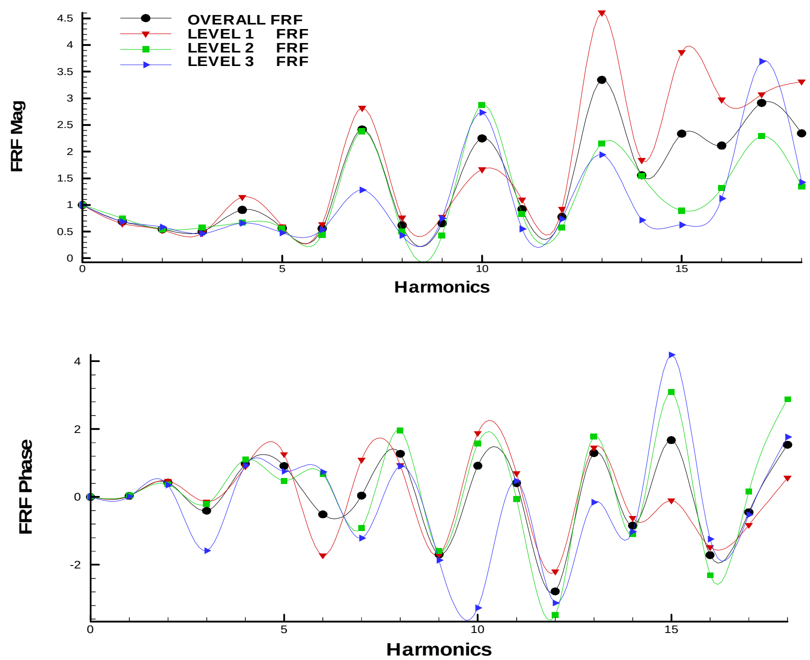

Figure 6.7: Common-Level Generalized FRF for Inlet P_t vs. Exit P_t

These series of graphs indicate that the generalized frequency response functions are very similar no matter how they are averaged for both inlet/exit parameter combinations.

However, this does not necessarily indicate how they will predict the exit total pressure profiles.

6.2.4 Comparing Exit Total Pressure Profile Predictions

Each of these generalized FRF's was applied to their respective inlet data sets. For example, the common-load FRF for operating point B was applied to the inlet parameters that were originally measured at operating point B (i.e. cases: S1B13, S1B12, S1B23, S2B13, S2B12, and S2B23) and likewise for OP C (i.e. cases: S1C13, S1C12, and S1C23). The same thing was done for the common-span and common-level FRF's. Obviously, the overall generalized FRF was applied to all eighteen combinations of span, operating point, and distortion level.

The next step was to determine which FRF or series of FRF's performed the best in predicting the exit total pressure profile behind the rotor. Figure 6.8 shows one of the better predicted responses by FRF's derived from AOA versus inlet P_t.

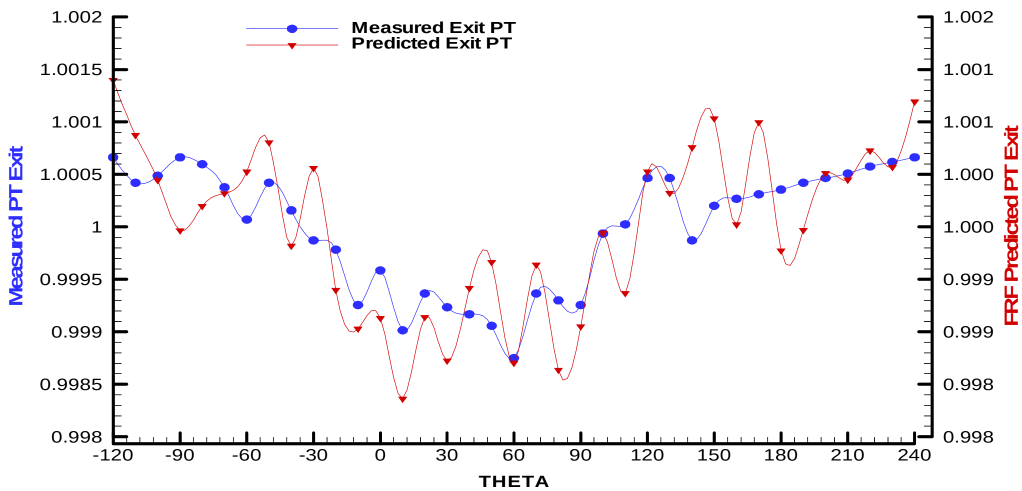

Figure 6.8: Predicted Exit P_t Using AOA vs. Exit P_t FRF

This is a prediction for Level 1, OP C, at 1/3 Span using the 'common-loading' generalized FRF for operating point C. It is accurate in predicting the overall shape of the profile, however, it fluctuates a good deal. As mentioned, this is one of the better predictions, and is in no way 'typical' for the FRF's derived from the AOA versus exit P_t relationship.

The frequency response functions derived from inlet P_t versus exit P_t predict the actual exit total pressure profiles very well. Figure 6.9 shows a typical predicted response plotted against the actual profile.

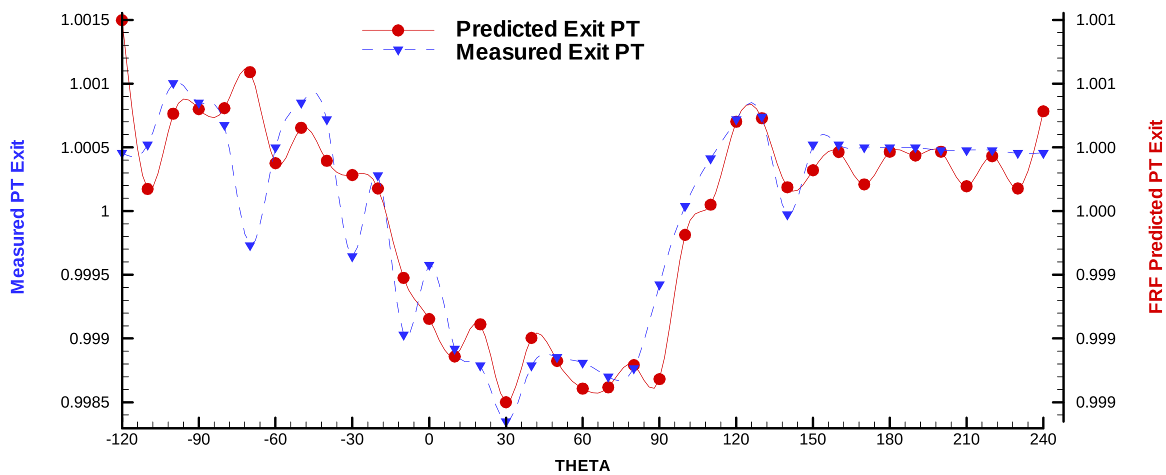

Figure 6.9: Predicted Exit P_t Using Inlet P_t vs. Exit P_t FRF

This is a prediction for Level 2, OP A, at 2/3 Span. By a mere visual inspection, it was determined that the frequency response functions derived from the inlet P_t versus exit P_t did the best job of predicting the response, as can be seen by these two preceding figures (6.8, 6.9).

Just as the magnitude and phase of the generalized FRF's did not change much when averaged in different ways (common-span, etc.), the resulting predicted responses did not vary much either. A visual inspection to determine the best FRF or series of FRF's was not sufficient. Therefore, cross-correlation coefficients were used to make this decision.

Figure 6.10 presents the correlation coefficients for the predictions using frequency response functions derived from the P_t versus P_t relationship.

Case	Overall	Common-Loading	Common-Span	Common-Level
S1A13	0.8362	0.8445	0.8031	0.8087
S1A12	0.8529	0.8408	0.8584	0.8941
S1A23	0.5944	0.6069	0.6124	0.5587
S1B13	0.7935	0.8462	0.8010	0.7861
S1B12	0.8923	0.9050	0.9185	0.8919
S1B23	0.8350	0.8246	0.8395	0.8320
S1C13	0.9088	0.8857	0.8896	0.8550
S1C12	0.8235	0.8869	0.9043	0.8095
S1C23	0.8622	0.9205	0.8313	0.8373
S2A13	0.8594	0.8701	0.9149	0.9018
S2A12	0.8878	0.8742	0.9139	0.9350
S2A23	0.8879	0.8814	0.8749	0.9095
S2B13	0.9156	0.9050	0.9450	0.9420
S2B12	0.8994	0.8761	0.9080	0.9539
S2B23	0.8560	0.8179	0.8404	0.9092
S3A13	0.7838	0.8053	0.8662	0.8191
S3A12	0.8369	0.8492	0.8545	0.8790
S3A23	0.8750	0.8608	0.8888	0.8755
mean	0.8445	0.8501	0.8591	0.8555
median	0.8594	0.8701	0.8749	0.8790
std dev	0.0725	0.0683	0.0737	0.0890

Figure 6.10: Correlation Coefficients for Exit P_t Predictions

The mean, median, and standard deviation provide a good indication of the accuracy of each series of FRF's in predicting the actual response. Notice how similar the mean coefficients are for each series of FRF's. There is no distinct advantage in using one series of FRF's over another when comparing the correlation coefficients. (It is interesting to note that the correlation coefficient for the predicted response in Figure 6.8 (AOA vs P_t FRF) is 0.81; this is lower than each of the mean coefficients in Figure 6.10. Therefore, the elimination of the FRF's derived from AOA vs. P_t by visual inspection, is justified by the correlation coefficients.) However, it was decided that the common-loading generalized FRF's would be used for three reasons: 1) as aerodynamic loading changes, the physics of the flow change, and 2) the standard deviation of the coefficients for this case was the smallest indicating that it is more consistent in predicting the response accurately. Using an FRF for each operating regime also helps to maintain the assumption that the blade row response is linear for small regions of operation, thus allowing the use of frequency response functions. The 'common-loading' FRF's are presented in Appendix C along with all of the exit total pressure profile predictions.

It was decided that the chosen FRF's predict the exit total pressure profile with sufficient accuracy for possible use in predicting the dynamic stage characteristics.

Figure 6.11 shows some more predicted responses by these generalized frequency response functions.

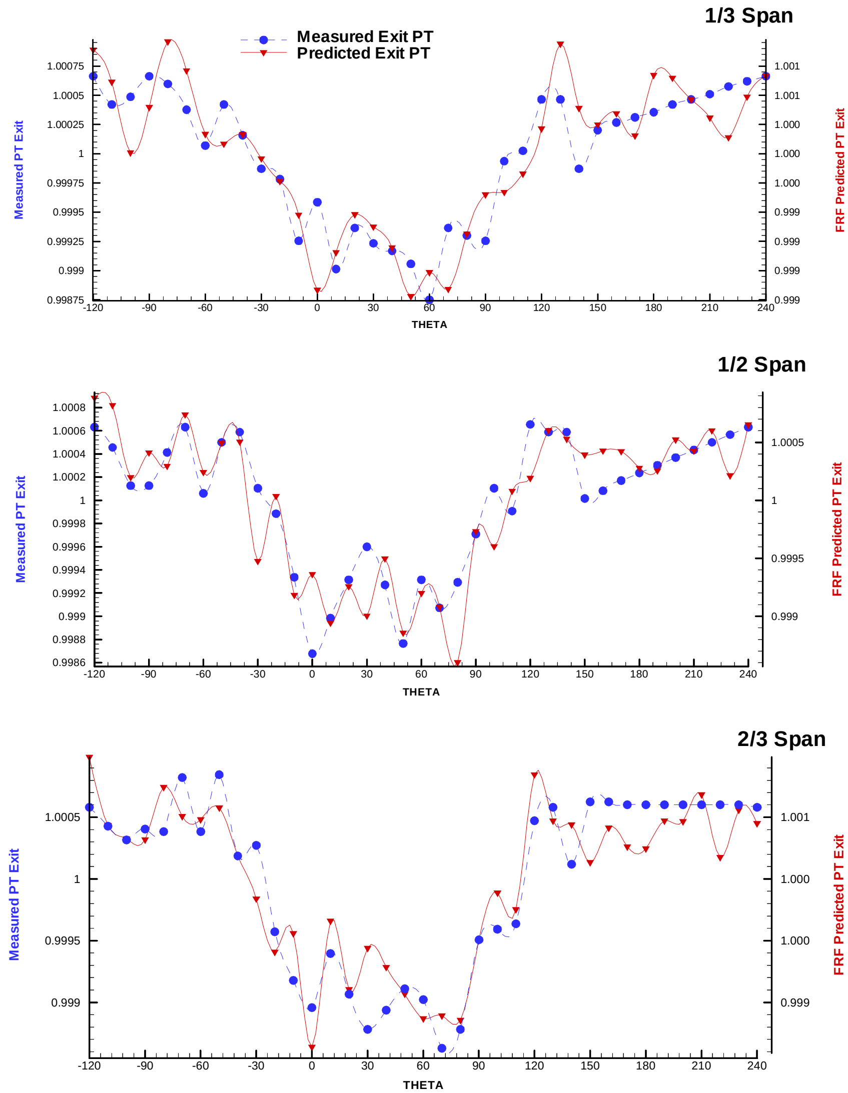

Figure 6.11: Predicted Exit Total Pressure Profiles

These predictions are for Level 1, OP C, for all three measurement spans. There are some differences between the predicted and actual responses, as expected. However, these differences are not very significant when considering their application in the attempted method for predicting dynamic stage characteristics, as described in the next section.

6.2.5 Theory Underlying the Attempted Prediction Method

To create a stage characteristic, both a mass flow and a pressure rise value are needed. The proposed method discretizes the annulus area into three concentric rings using the midpoint between each span radius as the dividing 'ring'. Each ring is then divided into 10° sections circumferentially, resulting in a total of 108 areas, as shown in Figure 6.12.

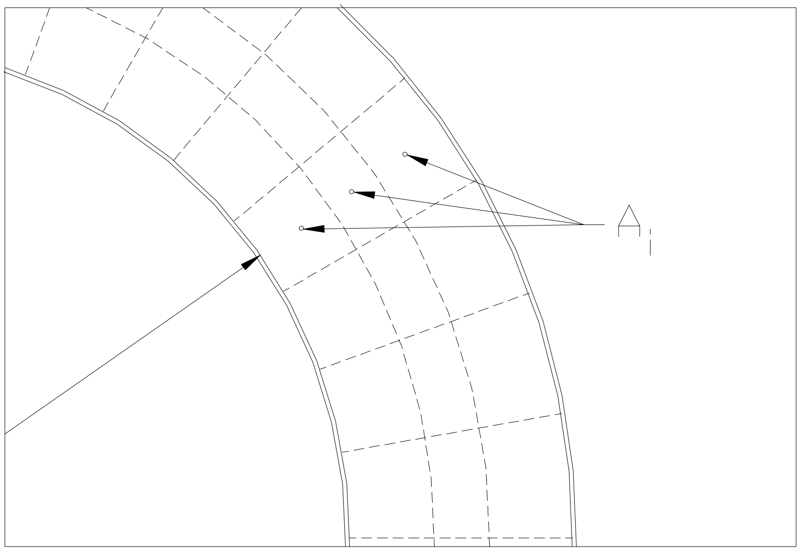

Figure 6.12: Discrete Areas of Annulus

Each area corresponds to each position circumferentially at all three spans, where data were measured. Therefore, each area, A_i, has its own inlet total and static pressure. By assuming the inlet velocity to be nearly axial (no IGV), the axial velocity can be calculated using the definition of total pressure in Equation 6.14.

$$V = \sqrt{2(P_t - P_s)/\rho} \qquad \textbf{Equation 6.14}$$

The density was assumed to have a constant value of 1.225 lbm/ft^3. The inlet axial velocity was assumed to be equal to that at the exit of the rotor; this is a common assumption in turbomachinery, especially when the annulus area is constant. The mass flow rate for each area can then be calculated using Equation 6.15

$$\dot{m} = \rho \cdot V \cdot A_{\text{i}} \qquad \textbf{Equation 6.15}$$

where V is the axial velocity. The mass flow values for each area are then summed to produce the total mass flow through the machine.

To determine the pressure rise across the machine, the predicted exit total pressure profiles are used. These profiles are normalized, so a scaling factor was needed. This scaling factor was obtained by taking the average value of the true exit P_t profiles. The basic relationship of the total pressure behind the rotor to the plenum pressure is represented in Equation 6.16.

$$\int P_{ti} \cdot \mathrm{d}\dot{m}_i - \mathrm{LOSSES} = \dot{m}_{TOT} \cdot P_{t\ PLENUM} \qquad \textbf{Equation 6.16}$$

Equation 6.16 can be converted to the summation in Equation 6.17 when neglecting losses.

$$\sum_i \dot{m}_i P_{ti} = \dot{\mathrm{m}}_{\mathrm{TOT}} P_{t\ PLENUM} \qquad \textbf{Equation 6.17}$$

The plenum total pressure is not merely going to be the average value of the rotor exit total pressure profile. The mass carrying component of the flow, as well as the area in question, will have a sizeable influence on the resulting back pressure in the plenum. Therefore, weighting the total pressure with the mass flow rate at each discrete area will account for these influences. These mass-flow/total-pressure products can then be summed and divided by the total mass flow through the machine to obtain the predicted plenum total pressure (Equation 6.17). Note that for the low speed flow in question, the total and static plenum pressures are assumed equal.

6.3 Dynamic Stage Characteristic Prediction Results

The proposed method was applied to the isolated rotor used in the experimental investigation to see if it could reproduce the rotor performance map in the initial attempt at predicting dynamic stage characteristics. Figure 6.13 shows the predicted points plotted against the actual stage characteristic.

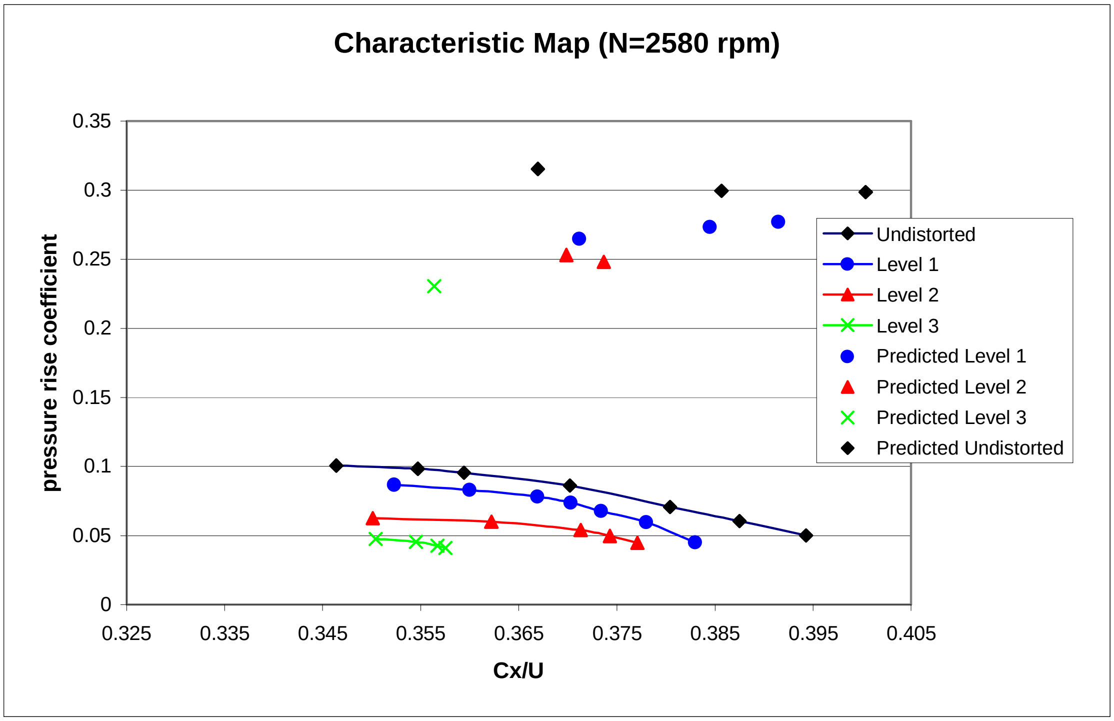

Figure 6.13: Predicted Stage Characteristic vs. Actual Characteristic

It is evident that the mass flow prediction is fairly accurate. This was expected, since the true inlet total and static pressure profiles were used to calculate the axial velocities. It is interesting to note that the values used for the discrete areas, A_i, have a significant influence on the resulting mass flow rate values.

Although the predicted pressure rise values are very high (about a factor of 3.3), their relation to one another is reasonably good. The prediction method does not account for losses, resulting in these notably high pressure rise values. These results show that the mixing losses between the rotor and plenum chamber of an isolated rotor are quite significant. This is attributed to the fairly high tangential velocity and uncontrolled diffusion behind the rotor. In addition, there is uncontrolled expansion of the flow as it enters the plenum from the annulus. Due to the poor diffusion recovery, the flow is essentially losing most of the velocity term of Equation 6.18.

$$P_t = P_s + \frac{1}{2}\rho V^2 \qquad \textbf{Equation 6.18}$$

Since the static pressure is quite small, the overall losses appear to be larger. If the static pressure were higher, the poor recovery of the flow kinetic energy would not be as significant. Therefore, the total pressure exiting the rotor is not going to fully contribute to the plenum pressure. This was evident in the experimental investigation. A typical plenum pressure was around 175 Pa, while a typical corresponding exit total pressure value behind the rotor was about 550 Pa. This is about the same factor of three between the two pressures as seen in the predicted stage characteristic of Figure 6.12. If a stator row existed behind the rotor to turn the flow back in the axial direction and a properly designed diffuser were applied, the losses would be expected to be much lower.

The current method was also applied when using the actual exit total pressure profiles. The results were identical, to three significant figures, due to the accuracy of the FRF-predicted total pressure profiles. The summation scheme used is very similar to numeric integration. Therefore, the differences between the predicted and actual total pressure profiles were not significant as mentioned previously. In other words, the area under the curves was very similar despite fluctuations in the predicted and actual rotor responses.

To summarize, the proposed method for predicting dynamic stage characteristics was applied to the isolated rotor used in the experimental investigation with mixed results. The mass flow predictions were reasonably accurate while the pressure rise predictions were very high due to the negligence of mixing losses behind the rotor. With continued work (i.e. use of loss factors), it is hoped that this method can be very beneficial to the dynamic compressor modeling community.

7 Conclusions

The following conclusions can be made from this investigation:

Experimental

- The overall qualitative behavior (shape) of the blade response to an inlet pressure distortion was not found to be a function of distortion level, operating point, or span. However, in quantitative detail, the magnitudes of the responses were expressed as functions of distortion level, operating point, and span.
- The angle of attack and wake depth parameters increase, while the inlet velocity and wake width decrease, as the span increases from hub to tip.
- The angle of attack and inlet static pressure both increase, while the inlet velocity decreases, as the aerodynamic loading increases.
- As the distortion level increases, the angle of attack, wake depth, and wake width increase, while the inlet total and static pressures, and exit total pressure decrease within the distorted region only.
- The exit total pressure response often leads both input drivers (inlet P_t and AOA), especially the AOA. The wake parameters typically lag both input drivers slightly.
- At higher machine speeds, the blade wakes tend to thin and elongate.
- The correlation between the inlet total pressure profile and that of the exit total pressure is the highest (0.83), followed by the AOA versus exit total pressure relationship (0.70).

Analytical

- By assuming the blade row response to be linear for small changes in operating region, frequency response functions (FRF) derived from the experimental data can be successfully averaged in the frequency domain for use in predicting exit flow parameters.
- A preliminary method for predicting dynamic stage characteristics using FRF-predicted rotor exit total pressure profiles was presented.

8 Recommendations

The following recommendations are submitted with respect to future work in measuring and predicting the dynamic response of compressors:

Experimental

- Perform similar dynamic rotor response experiments using a more current blade profile and/or with a stator row behind the rotor to help control the diffusion.
- Instrument the test rig so that both inlet and outlet measurements can be taken simultaneously, thus retaining the maximum amount of dynamic information in the data sets.
- Instrument the test rig so that the exit velocity triangle can be determined.

Analytical

- Evaluate the performance of the generalized frequency response functions when predicting multiple-per-rev inlet distortions, as well as other inlet profiles.
- Continue work on the proposed method so that it accounts for mixing losses (loss factors). Once the predicted pressure rise is more accurate, work toward limiting the amount of experimental data needed in order to apply the method to different compressors.
- Investigate some non-linear methods of predicting blade response, since turbomachinery is non-linear by nature.

9 List of References

Cited Works

Adamczyk, J.J., 1974, "Unsteady Fluid Dynamic Response of an Isolated Rotor with Distorted Inflow," AIAA Paper No. 74-49.

Boller, S.M., "One-Dimensional Dynamic Wake Response in an Isolated Rotor Due to Inlet Total Pressure Distortion," M.S. Thesis, Virginia Polytechnic Institute & State University, Blacksburg, Virginia, 1998.

Braithwaite, W.M., Graber Jr., E.J., Mehalic, C.M., "The Effect of Inlet Temperature and Pressure Distortion on Turbojet Performance." AIAA Paper No. 73-1316, AIAA/SAE 9th Proplusion Conference, November 5-7, 1973, Las Vegas, Nevada.

Burden, R.L., Faires, J.D. Numerical Analysis, 6th ed. Brooks/Cole. Pacific Grove. 1997.

Calogeras, J.E., Mehalic, C.M., Burstadt, P.L., "Experimental Investigation of the Effect of Screen-Induced Total-Pressure Distortion on Turbojet Stall Margin." NASA TMX-2239, March 1971.

Carta, F.O., "Analysis of Unsteady Aerodynamic Effects on Axial Flow Compressor Stage with Distorted Inflow." Project Squid – Techn. Rep. UARL – A – UP, 1972.

Cherrett, M.A., Bryce, J.D., and Ginder, R.B. "Unsteady Three-Dimensional Flow in a Single-Stage Transonic Fan: Part I – Unsteady Rotor Exit Flow Field." ASME Journal of Turbomachinery, Vol. 117, October 1995, pp. 506-513.

Colpin, J. Kool, P. "Experimental Study of an Axial Compressor Rotor Transfer Function with Non-Uniform Inlet Flow." ASME Paper No. 78-GT-69, Gas Turbine Conference and Products Show, April 9-13, 1978 London, England.

Cousins, W.T., "Techniques for the Analysis of Unsteady Pressure Measurements in an Axial-Flow Compressor." M.S. Thesis, Virginia Polytechnic Institute & State University, Blacksburg, Virginia, 1979.

Cousins, W.T., "The Dynamics of Stall and Surge Behavior in Axial-Centrifugal Compressors," Ph.D. Dissertation, Virginia Polytechnic Institute & State University, Blacksburg, Virginia, 1997.

Cousins, W.T., and O'Brien, W.F., "Axial-Flow Compressor Stage Post-Stall Analysis," AIAA Paper No. 85-1349, 1985.

Dancy, B.B. "Performance and Stalling Behavior of an Axial Flow Compressor With Circumferential Inlet Flow Distortion." M.S. Thesis, Virginia Polytechnic Institute & State University, Blacksburg, Virginia, 1976.

Drost, U. "An Experimental Investigation of the Corner Stall Behaviour of a Linear Compressor Cascade at High Angles of Attack." Diploma Project, Swiss Federal Institute of Technology – Lausanne, February, 1994.

Fox, R.W., McDonald, A.T. Introduction to Fluid Mechanics, Ed. 4. John Wiley and Sons, Inc. New York. 1992.

Gauden, W.H. "Performance and Stalling Behavior of an Axial-Flow Compressor Subjected to Three Circumferential Inlet Distortion Levels." M.S. Thesis, Virginia Polytechnic Institute & State University, 1977.

Henderson, R.E., and Horlock, J.H., "An Approximate Analysis of the Unsteady Lifts on Airfoils in a Cascade." ASME Paper No. 72-GT-5, 1972.

Henderson, R.E., Shen, I.C. "The Influence of Unsteady Rotor Response on a Distorted Flow Field." ASME Paper No. 81-GT-185, International Gas Turbine Conference and Products Show, March 9-12, 1981 Houston, Texas.

Hetherington, R., and Moritz, R.R., "Influence of Unsteady Flow Phenomena on the Design and Operation of Aero Engines." AGARD CP 177, 1975.

Hill, P.G., and Peterson, C.R., Mechanics and Thermodynamics of Propulsion, Ed. 2. Addison-Wesley Publishing Company, New York, 1992.

Howard, J.S., "Improved Methods for Modeling Dynamic Stage Characteristics," M.S. Thesis, Virginia Polytechnic Institute & State University, Blacksburg, Virginia, 1999.

Kerrebrock, J.L., Epstein, A.H., Haines, D.M., and Thompkins, W.T. "The M.I.T. Blowdown Compressor Facility." ASME Journal of Engineering for Power, October, 1974 pp. 394-406.

Kimzey, W.F. "An Analysis of the Influence of Some External Disturbances on the Aerodynamic Stability of Turbine Engine Axial Flow Fans and Compressors." AEDC-TR-77-80, August 1977.

Kline, S.J., McClintock, F.A., "Describing Uncertainties in Single Sample Experiments." Mechanical Engineering, January 1953, pg. 3.

Lakshminarayana, B., Govindan, T.R., Reynolds, B. "Effects of Rotation and Blade Incidence on the Properties of the Turbomachinery Rotor Wake." AIAA Paper No. 81-0054, AIAA 19th Aerospace Sciences Meeting, January 12-15, 1981 St. Louis, Missouri.

Mazzawy, R.S., "Multiple Segment Parallel Compressor Model for Circumferential Flow Distortion." AGARD CP 177, 1975.

Mazzawy, R.S. "Multiple Segment Parallel Compressor Model for Circumferential Flow Distortion." ASME Journal of Engineering for Power, April, 1977.

McCarthy, J.H. "Steady Flow Past Non-Uniform Wire Grids." Journal of Fluid Mechanics, Vol. 19, 1964.

Melick, H.C., "Analysis of Inlet Flow Distortion and Turbulence Effects on Compressor Stability." NASA CR 114577, 1973.

Melick, H.C., and Simpkins, W.E., "A Unified Theory of Inlet/Engine Compatability," AIAA Paper No. 72-1115, 1972.

Mikolajczak, A.A., and Pfeffer, A.M., "Methods to Increase Engine Stability and Tolerance to Distortion," AGARD Lecture Series No. 72, Sect. 7, 1974.

Mokelke, H., "Prediction Techniques," AGARD Lecture Series No. 72, Sect. 5, 1974.

Muhlemann, E. "Experimentelle Untersuchungen an einer axialen Geblasestufe," Mitteilungen Aus Dem Institut fur Aerodynamik, No. 12, 1946.

Nagano, S., and Takata, H., "Nonlinear Analysis of Rotating Stall," Institute of Space and Aeronautical Science, University of Toyko, Report No. 449, 1970.

Neal, T.E. "The Lift Response of a Rotating Blade of an Axial-Flow Compressor to Inlet Flow Distortion." M.S. Thesis, Virginia Polytechnic Institute & State University, Blacksburg, Virginia, 1975.

Ng, W.F., Epstein, A.H. "Unsteady Losses in Transonic Compressors." ASME Journal of Engineering for Gas Turbines and Power, Vol. 107, 1985, pp. 345-353.

Pearson, H., McKenzie, A., "Wakes in Axial Compressors." *Journal of Royal Aeronautical Society*, Vol. 63, July, 1959.

Ravindranath, A., Lakshminarayana, B. "Mean Velocity and Decay Characteristics of the Near and Far-Wake of a Compressor Rotor Blade of Moderate Loading." ASME Journal of Engineering for Power, Vol. 102, pp. 535-548, July 1980.

Reid, C. "The Response of Axial Flow Compressors to Intake Flow Distortion." ASME Paper No. 69-GT-29, 1969.

Reynolds, B. and Lakshminarayana, B. "Characteristics of Lightly Loaded Fan Rotor Blade Wakes." NASA CR-3188, October, 1979.

Reynolds, B., Lakshminarayana, B., and Ravindranath, A. "Characteristics of the Near Wake of a Compressor Rotor." AIAA Paper No. 78-1141, AIAA 11th Fluid and Plasma Dynamics Conference, July 10-12, 1978 Seattle, Washington.

Roberts, F., Plourde, G.A., Smakula, F. "Insights into Axial Compressor Response to Distortion." AIAA Paper No. 68-565, 1968.

SAE Aerospace Recommended Practice, ARP-1420. "Gas Turbine Engine Inlet Flow Distortion Guidelines." March, 1978.

Schmidt, D.P., Okiishi, T.H. "Detailed Measurements of the Periodically Unsteady Flow Produced by Rotor and Stator Wake Interaction in a Multi-stage Turbomachine." AIAA Paper No. 77-202, AIAA 15th Aerospace Sciences Meeting, January 24-26, 1977 Los Angeles, California.

Sexton, M.R. "An Investigation of the Dynamic Stalling Characteristics of Rotating Axial-Flow Compressor Blades." Ph.D. Dissertation, Virginia Polytechnic Institute & State University, Blacksburg, Virginia, 1980.

Sexton, M.R., and O'Brien, W.F., "A Model for Dynamic Loss Response in Axial-Flow Compressors," ASME Paper, 1980.

Shreeve, R.P., Dodge, F.J., Hawkins, W.R., and Larson, V.J. "Probe Measurements of Velocity and Losses From a Small Axial Transonic Rotor." AIAA Paper No. 79-1198, AIAA 11th Fluid and Plasma Dynamics Conference, July 10-12, 1978 Seattle, Washington.

Shreeve, R.P., Neuhoff, F. "Measurements of the Flow From a High-Speed Compressor Rotor Using a Dual Probe Digital Sampling (DPDS) Technique." ASME Journal of Engineering for Gas Turbines and Power, Vol. 106 pp. 366-375, April 1984.

Shreeve, R.P., Simmons, J.M., West, J.C., and Winters, K.A. "Determination of Transonic Compressor Flow Field by Synchronized Sampling of Stationary Fast Response Transducers." Nonsteady Fluid Dynamics Proceedings of the Winter Annual Meeting, pp. 91-101, December 10-15, 1978 San Francisco, California.

Soeder, R.H., Bobula, G.A. "Effect of Steady-State Pressure Distortion on Flow Characteristics Entering a Turbofan Engine." NASA TM 79134, April, 1979.

Tesch, W.A., and Steenken, W.G., "Blade Row Dynamic Digital Compressor Program, Vol II," NASA-CR-134953, and private communication, Steenken, W.G., 1981, General Electric Company, Cincinnati, Ohio.

Treaster, A.L., Yocum, A.M. "The Calibration and Application of Five-hole Probes." ISA Transactions, Vol. 18, No. 3, 1979 pp. 23-34.

Ufer, H. “Analysis of the Velocity Distribution at the Blade Tips of Axial-Flow Compressors,” Technische Mitteilungen Krupp (Forschung Sberichte), Vol. 26, No. 2, 1968, pp. 33-45, English Translation, NASA TTF-16 366.

Yocum, A.M. “An Experimental and Numerical Investigation of the Performance of Compressor Cascades with Stalled Flow.” Ph.D. Dissertation, Virginia Polytechnic Institute & State University, Blacksburg, Virginia, 1988.

Uncited Works

Beckwith, T.G., Marangoni, R.D., and Lienhard, J.H., Mechanical Measurements, Ed. 5. Addison-Wesley Publishing Company, New York, 1992.

Bendat, J.S., Piersol, A.G., Random Data: Analysis and Measurement Procedures. John Wiley &Sons, Inc., New York, 1971.

Boytos, J.F. “State-of-the-Art Review: Aircraft Gas Turbines – Inlet Distortion Indices.” NAPTC-PE-95, March 1977.

Edgington, E.S., Randomization Tests, 3rd Ed. Marcel Dekker, Inc., New York, 1995.

Hale, A.A., “A 3D Turbine Engine Analysis Compressor Code (TEACC) for Steady-State Inlet Distortion.” Ph.D. Dissertation, Virginia Polytechnic Institute & State University, 1996.

Korn, J.A., “Estimated Effect of Circumferential Distortion on Axial Compressors Using Parallel Compressor Theory and Dynamic Stall Delay.” AIAA Paper No. 74-233, 1974.

Lakshminarayana, B. “Techniques for Aerodynamic and Turbulence Measurements in Turbomachinery Rotors.” *Measurement Methods in Rotating Components of Turbomachinery*. ASME Joint Fluids Engineering Gas Turbine Conference and Products Show, March 10-13, 1980.

Stearns, S.D., and David, R.A., Signal Processing Algorithms in Fortran and C, Prentice Hall, Englewood Cliffs, New Jersey, 1993.

Verdesoto, G.A. “An Experimental Study of Rotating Stall in an Axial-Flow Compressor.” M.S. Thesis, Virginia Polytechnic Institute & State University, 1977.

10 Appendix A

Experimental Inlet Distortion Rotor Response Data

Location of Experimental Data

Distortion Level	Operating Point	Page Location
Undistorted	OP's A, B, & C	p. 100
Level 1	OP A	pp. 101-102
Level 1	OP B	pp. 103-104
Level 1	OP C	pp. 105-106
Level 2	OP A	pp. 107-108
Level 2	OP B	pp. 109-110
Level 3	OP A	pp. 111-112

Figure A.1: Location of Experimental Data

Undistorted Inlet and Exit Flow Parameters

OPERATING POINT A	1/3 Span	1/2 Span	2/3 Span
Angle of Attack (AOA)	9.7	10.3	11.8
Pitch Angle	13.2	10.9	9.6
Inlet Total Pressure (non-dim)	-0.031	-0.033	-0.076
Inlet Static Pressure (non-dim)	-0.207	-0.203	-0.1821
Exit Total Pressure (non-dim)	0.223	0.296	0.375
Wake Depth (non-dim)	-0.1814	-0.228	-0.285
Wake Width (non-dim)	0.1285	0.1018	0.1299
Suction Side Jet Magnitude (non-dim)	0.095	0.1177	0.1243
Suction Side Jet Width (non-dim)	0.084	0.097	0.1217

OPERATING POINT B	1/3 Span	1/2 Span	2/3 Span
Angle of Attack (AOA)	6.7	8	8.5
Pitch Angle	13.6	8.3	5.8
Inlet Total Pressure (non-dim)	-0.035	-0.036	-0.038
Inlet Static Pressure (non-dim)	-0.225	-0.218	-0.218
Exit Total Pressure (non-dim)	0.203	0.287	0.31
Wake Depth (non-dim)	-0.1624	-0.1996	-0.299
Wake Width (non-dim)	0.1384	0.1092	0.1306
Suction Side Jet Magnitude (non-dim)	0.084	0.1264	0.1541
Suction Side Jet Width (non-dim)	0.101	0.096	0.089

OPERATING POINT C	1/3 Span	1/2 Span	2/3 Span
Angle of Attack (AOA)	6.2	6.3	7.6
Pitch Angle	11.6	10.4	5.8
Inlet Total Pressure (non-dim)	-0.037	-0.038	-0.039
Inlet Static Pressure (non-dim)	-0.235	-0.244	-0.234
Exit Total Pressure (non-dim)	0.203	0.278	0.359
Wake Depth (non-dim)	-0.1627	-0.1928	-0.285
Wake Width (non-dim)	0.1288	0.1077	0.091
Suction Side Jet Magnitude (non-dim)	0.089	0.1289	0.1465
Suction Side Jet Width (non-dim)	0.1036	0.099	0.096

Figure A.2: Table of Undistorted Inlet and Exit Parameters

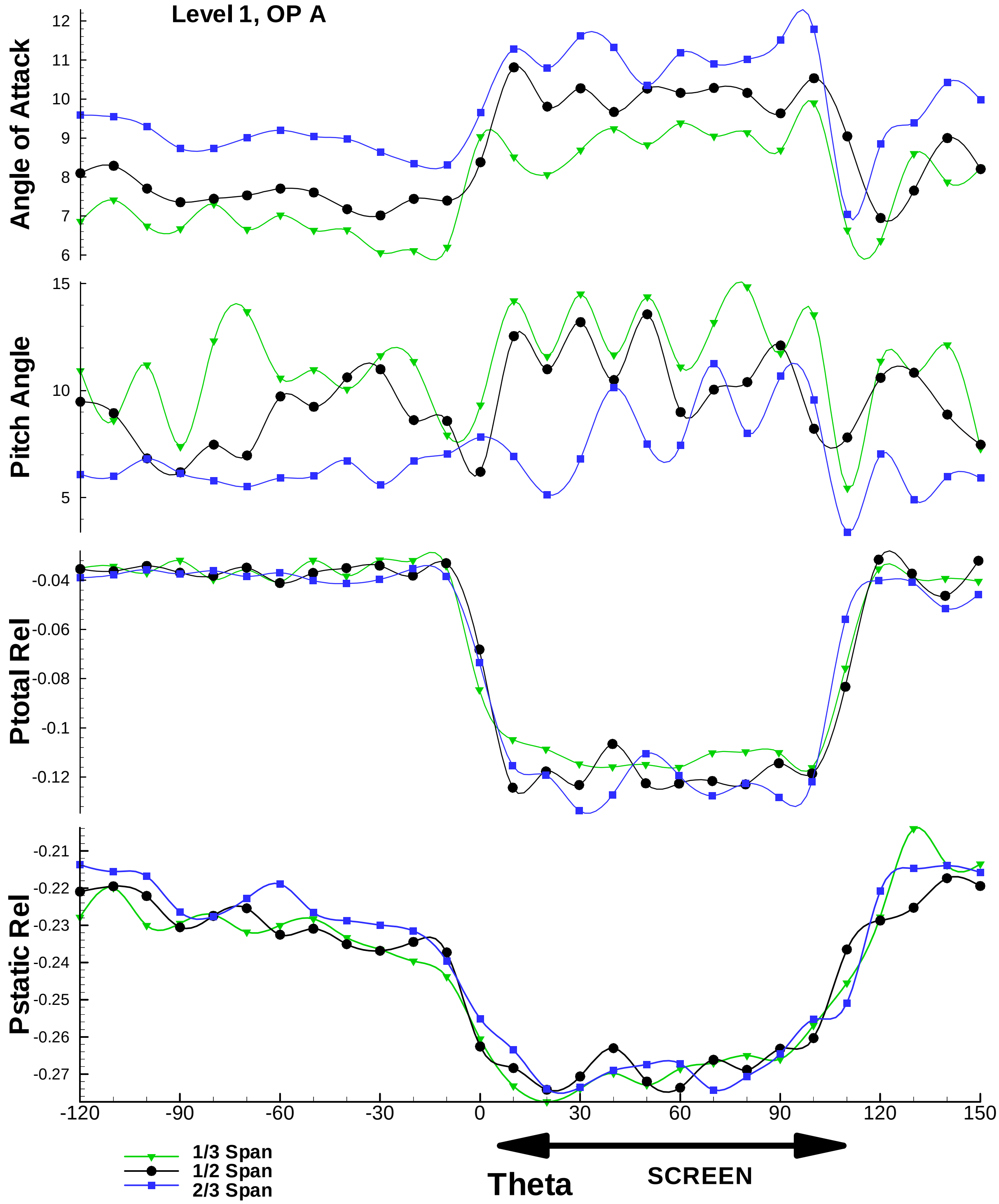

Figure A.3: Inlet Parameters for Level 1 Distortion, Operating Point A

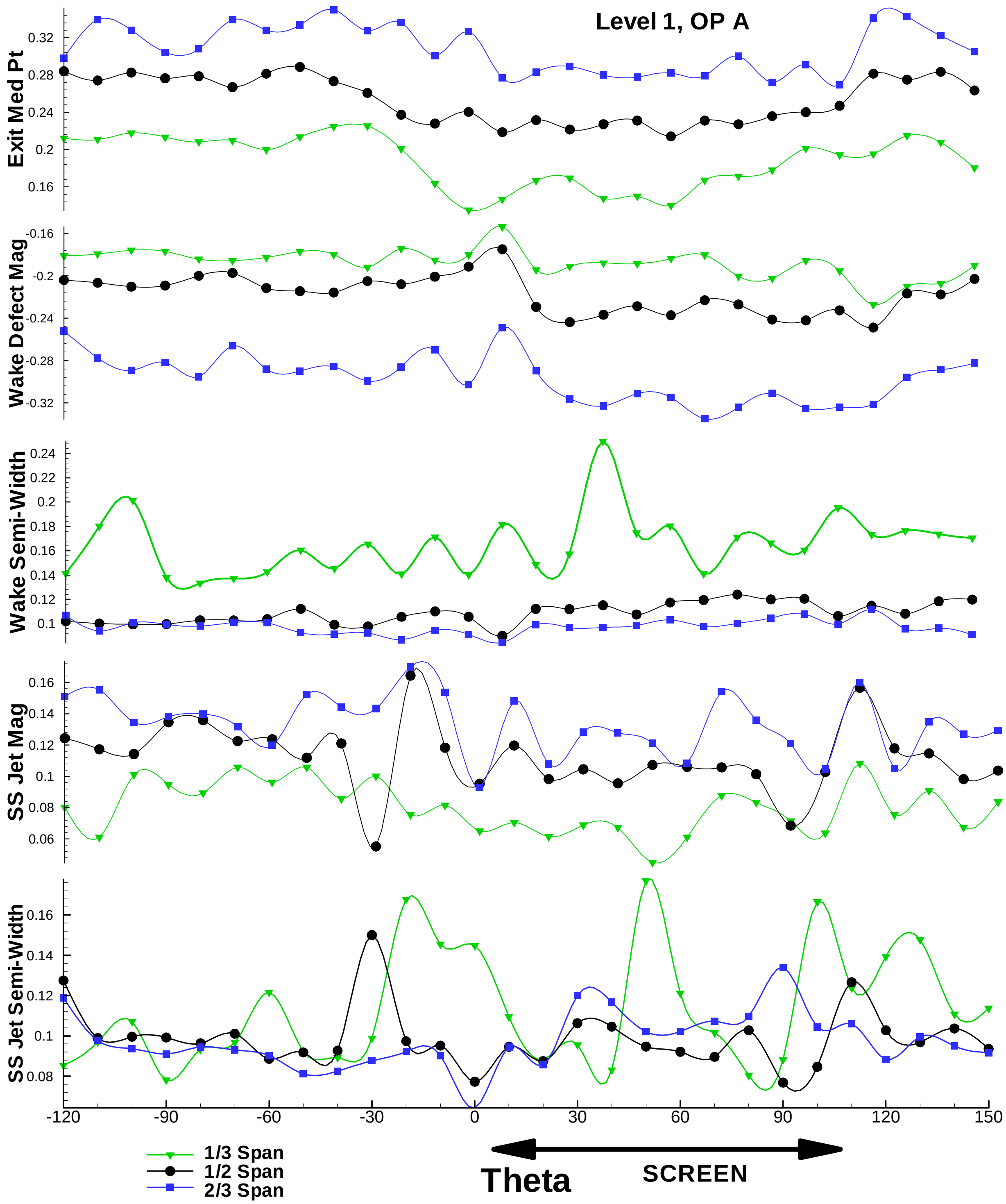

Figure A.4: Exit Parameters for Level 1 Distortion, Operating Point A

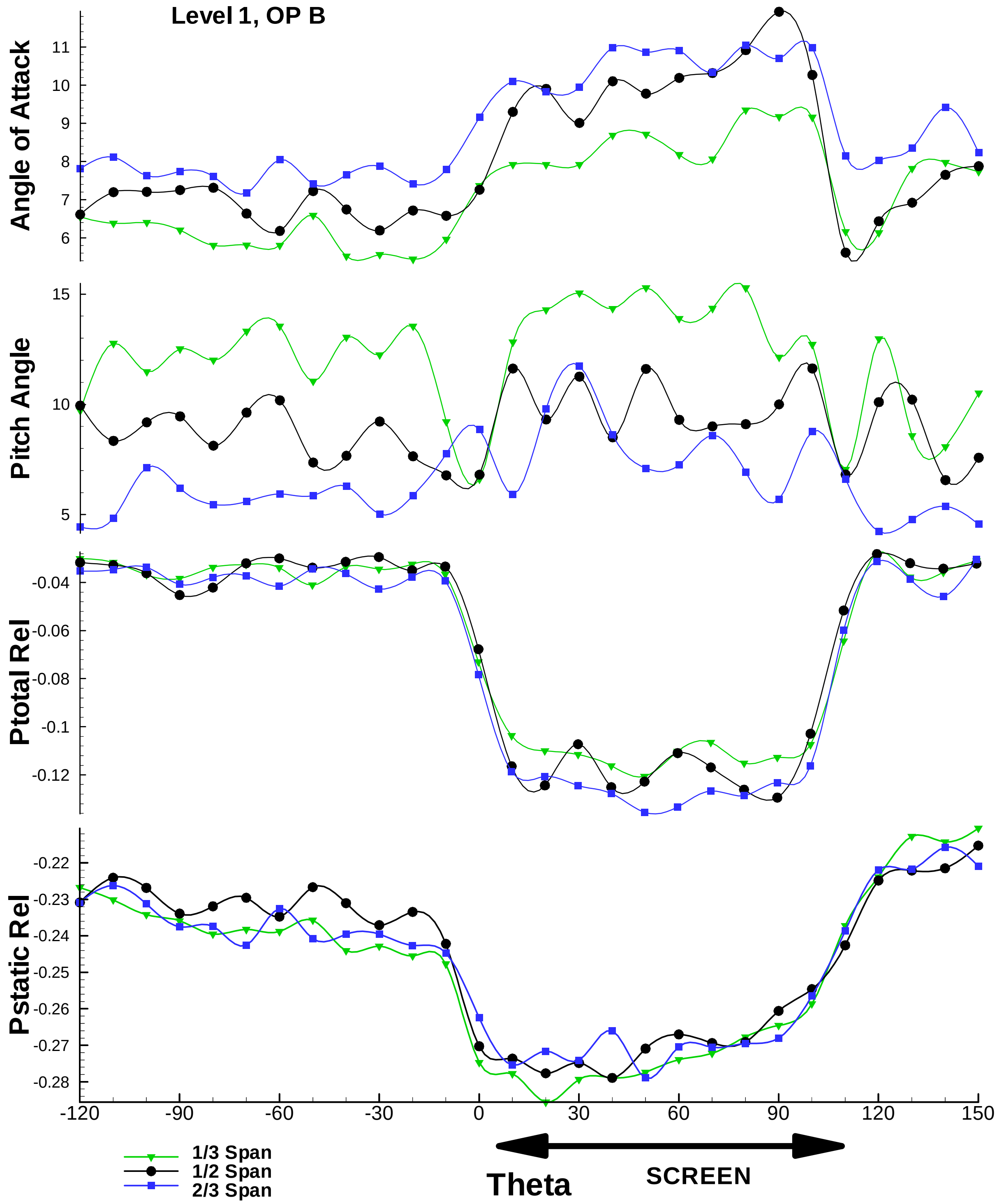

Figure A.5: Inlet Parameters for Level 1 Distortion, Operating Point B

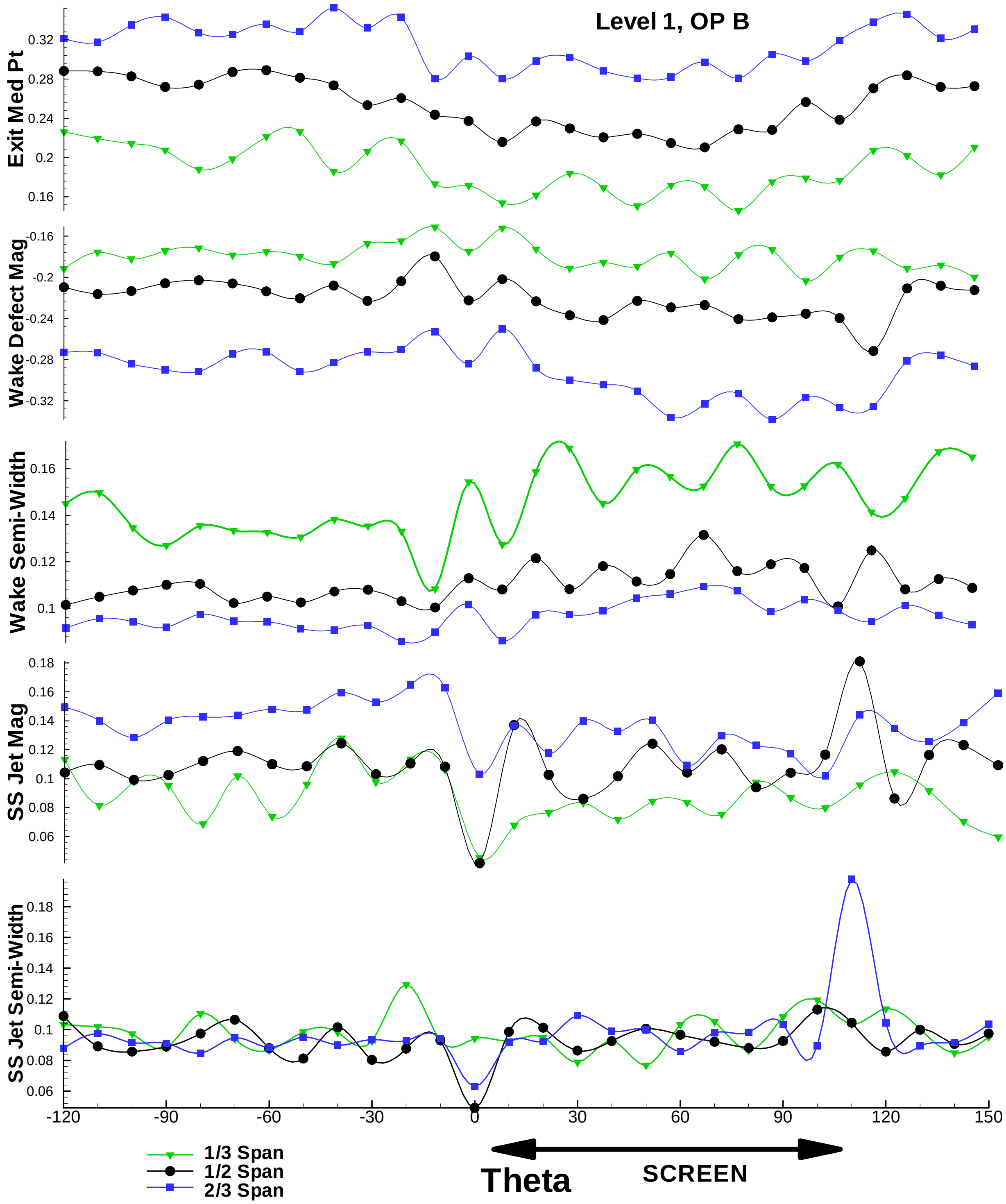

Figure A.6: Exit Parameters for Level 1 Distortion, Operating Point B

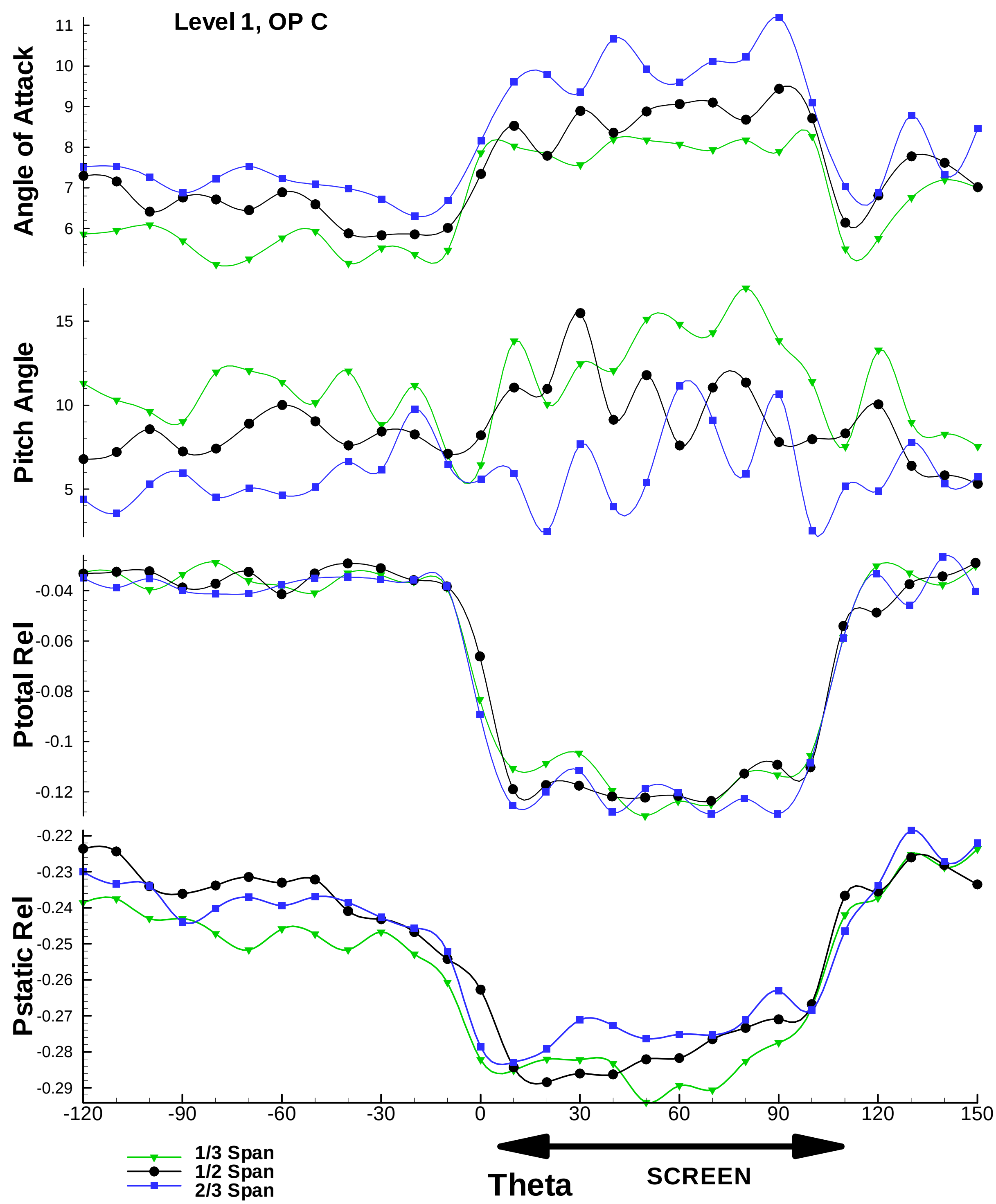

Figure A.7: Inlet Parameters for Level 1 Distortion, Operating Point C

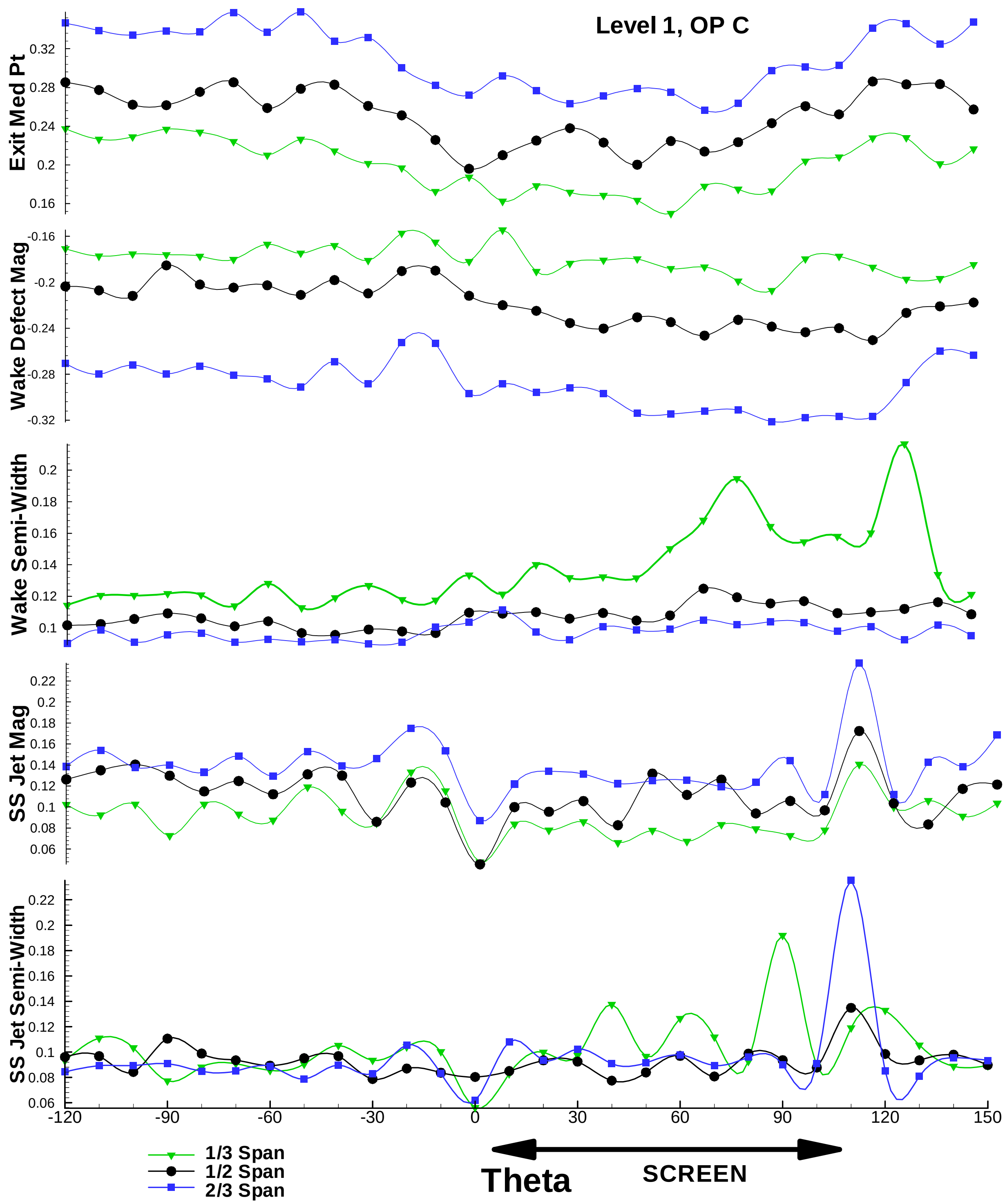

Figure A.8: Exit Parameters for Level 1 Distortion, Operating Point C

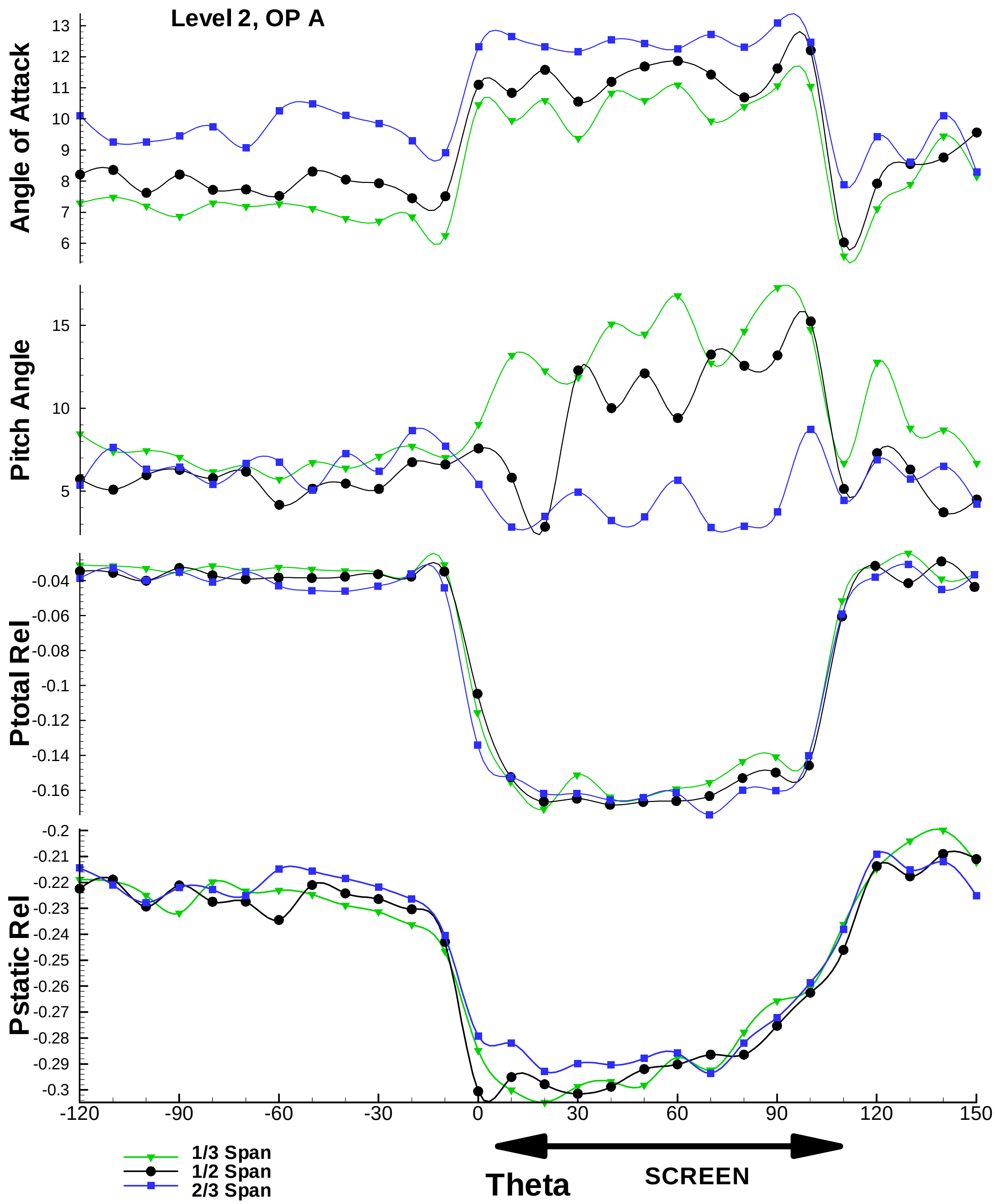

Figure A.9: Inlet Parameters for Level 2 Distortion, Operating Point A

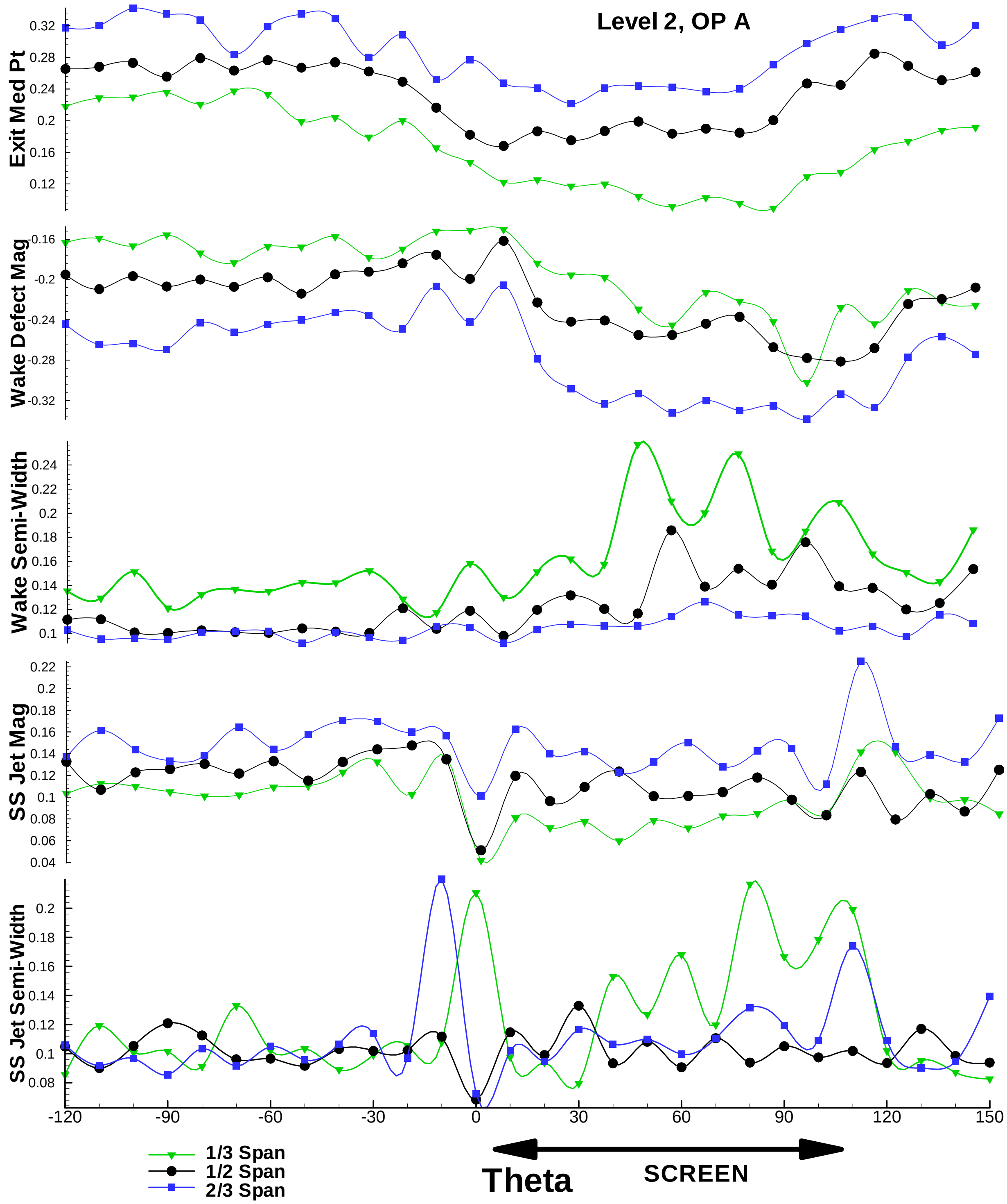

Figure A.10: Exit Parameters for Level 2 Distortion, Operating Point A

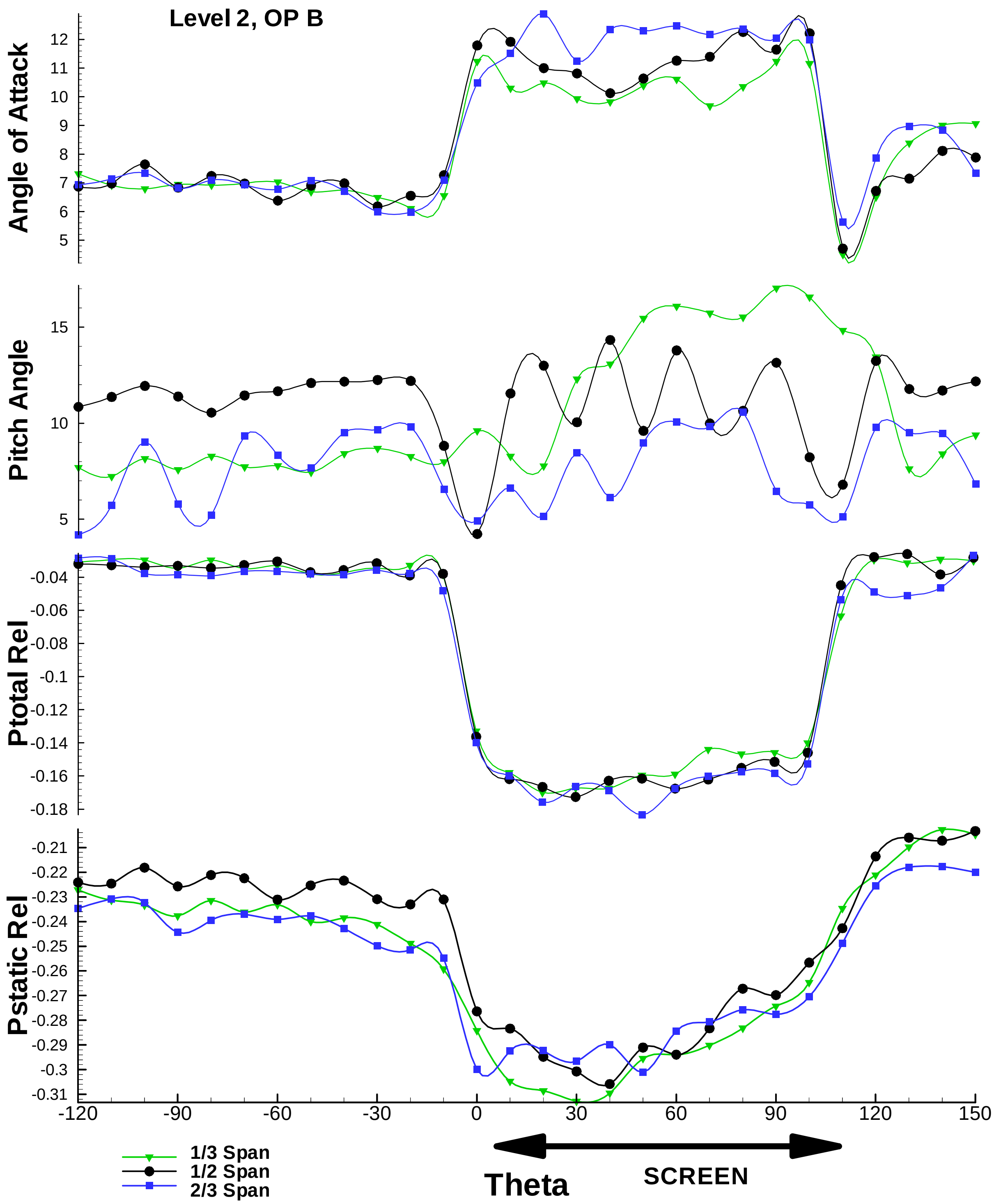

Figure A.11: Inlet Parameters for Level 2 Distortion, Operating Point B

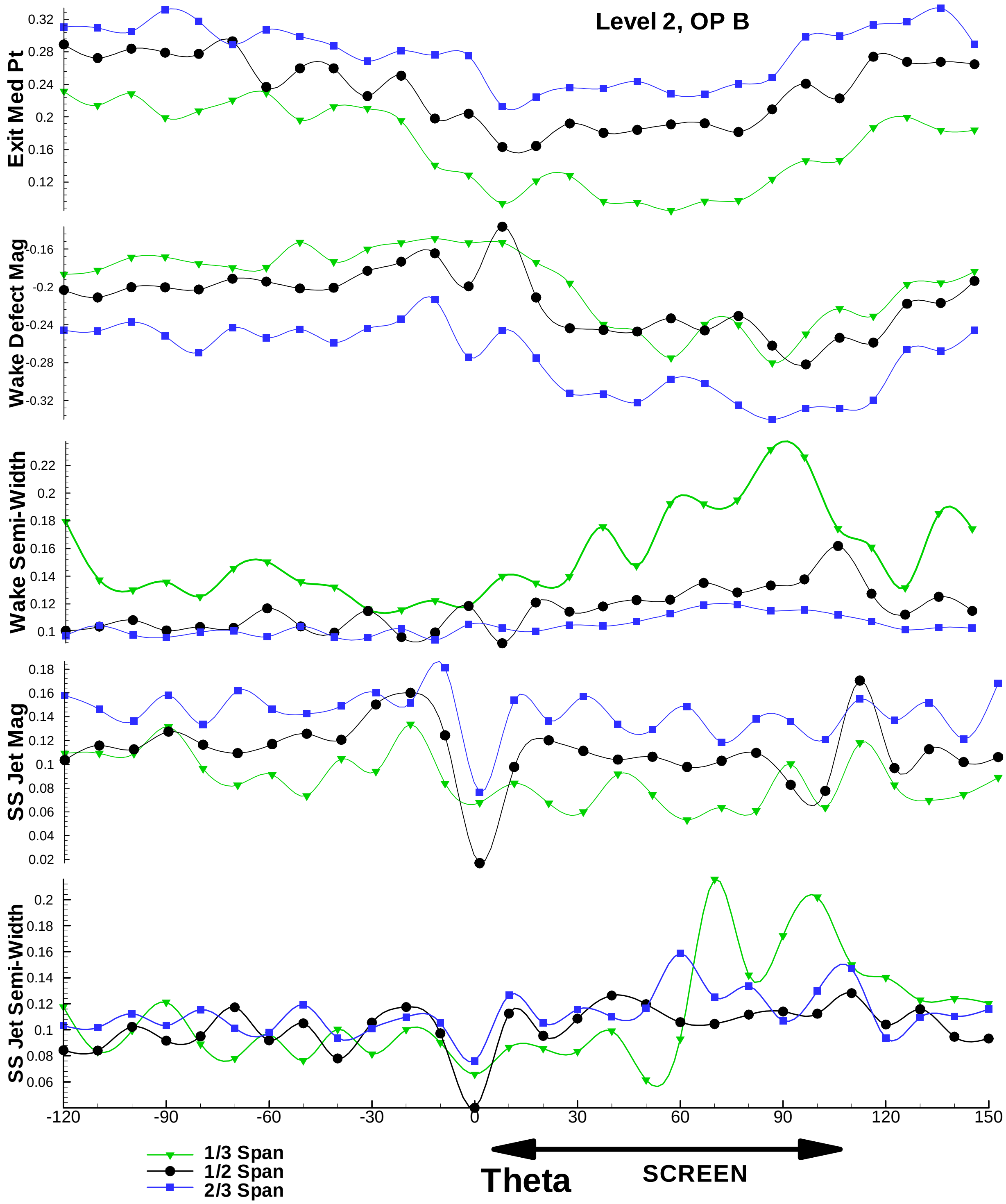

Figure A.12: Exit Parameters for Level 2 Distortion, Operating Point B

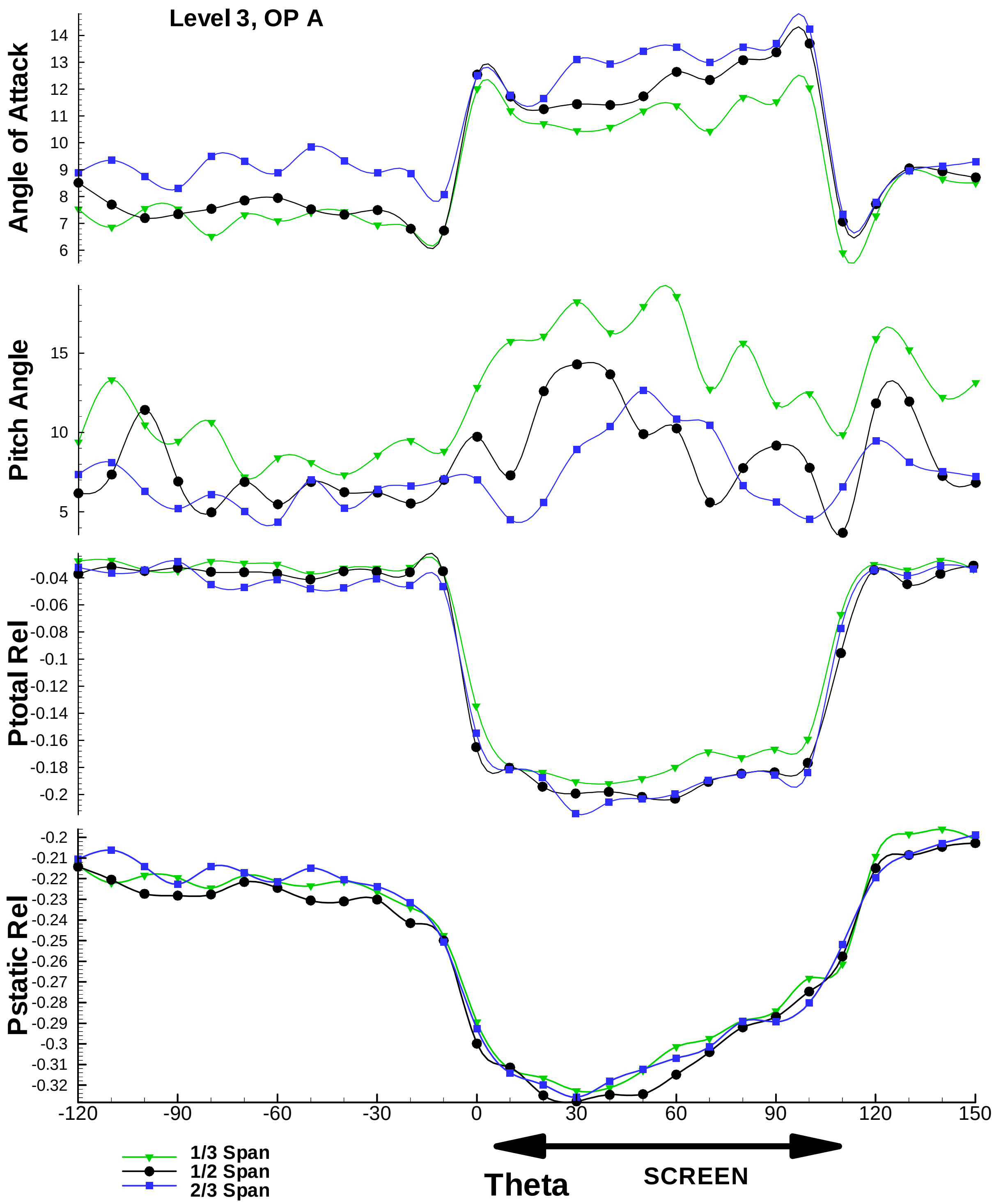

Figure A.13: Inlet Parameters for Level 3 Distortion, Operating Point A

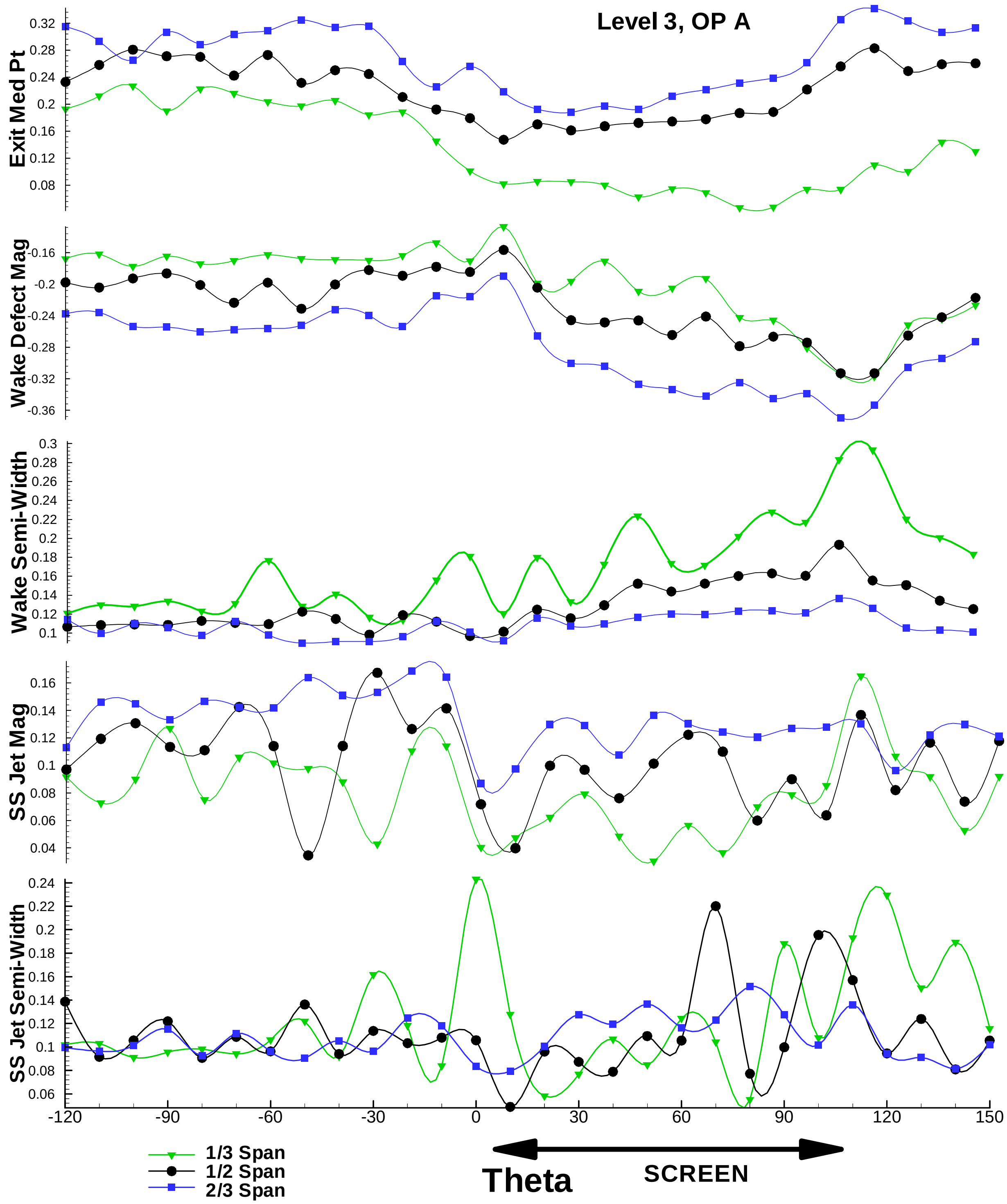

Figure A.14: Exit Parameters for Level 3 Distortion, Operating Point A

11 Appendix B

Frequency Response Functions Based on Inlet Total Pressure Versus Exit Total Pressure

Location of Frequency Response Functions (FRF)

Distortion Level	Operating Point	Span	Page Location
Level 1	OP A	1/3, 1/2, 2/3	pp. 115-117
Level 1	OP B	1/3, 1/2, 2/3	pp. 118-120
Level 1	OP C	1/3, 1/2, 2/3	pp. 121-123
Level 2	OP A	1/3, 1/2, 2/3	pp. 124-126
Level 2	OP B	1/3, 1/2, 2/3	pp. 127-129
Level 3	OP A	1/3, 1/2, 2/3	pp. 130-132

Figure B.1: Location of Frequency Response Functions (FRF)

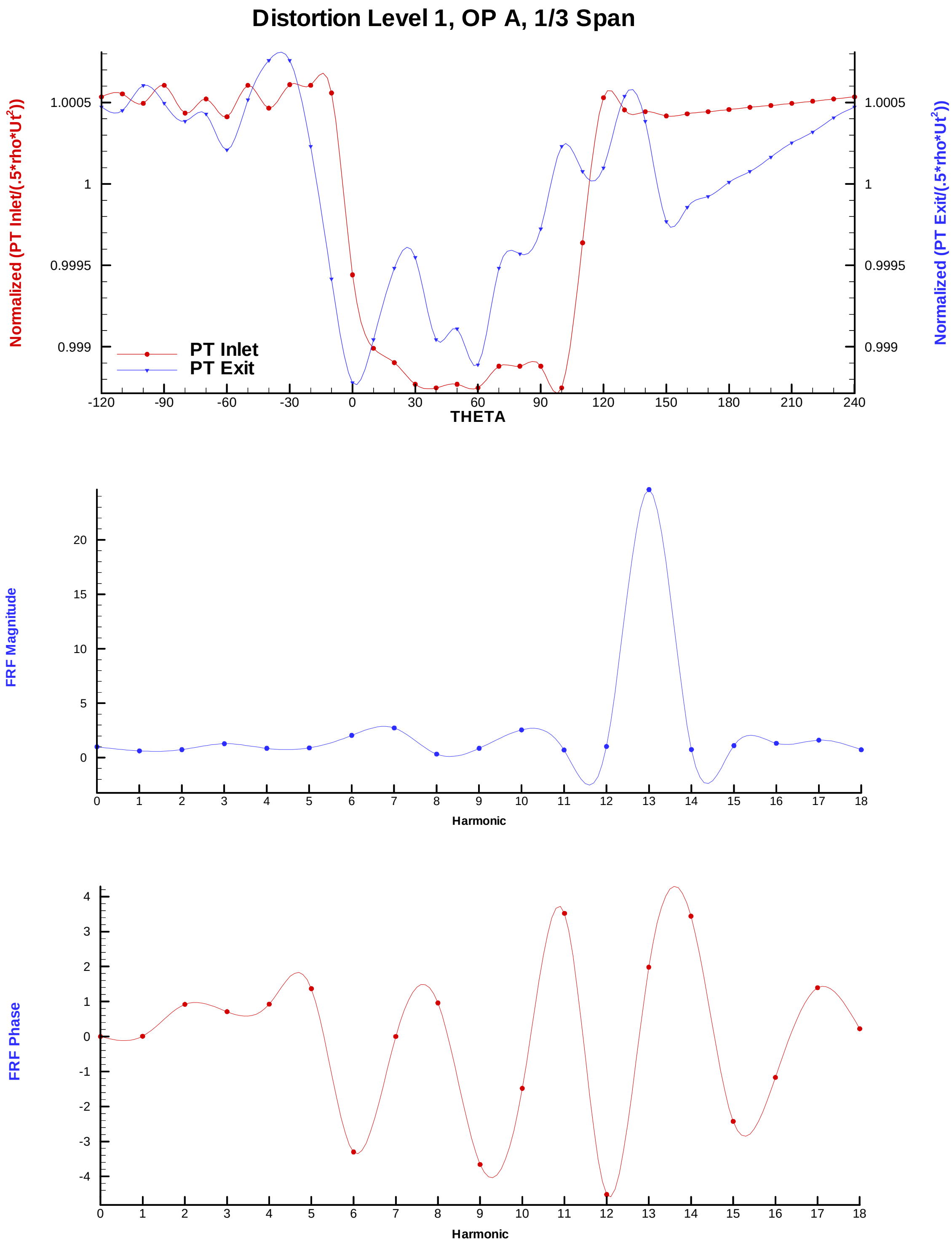

Figure B.2: FRF for Level 1 Distortion, Operating Point A, at 1/3 Span

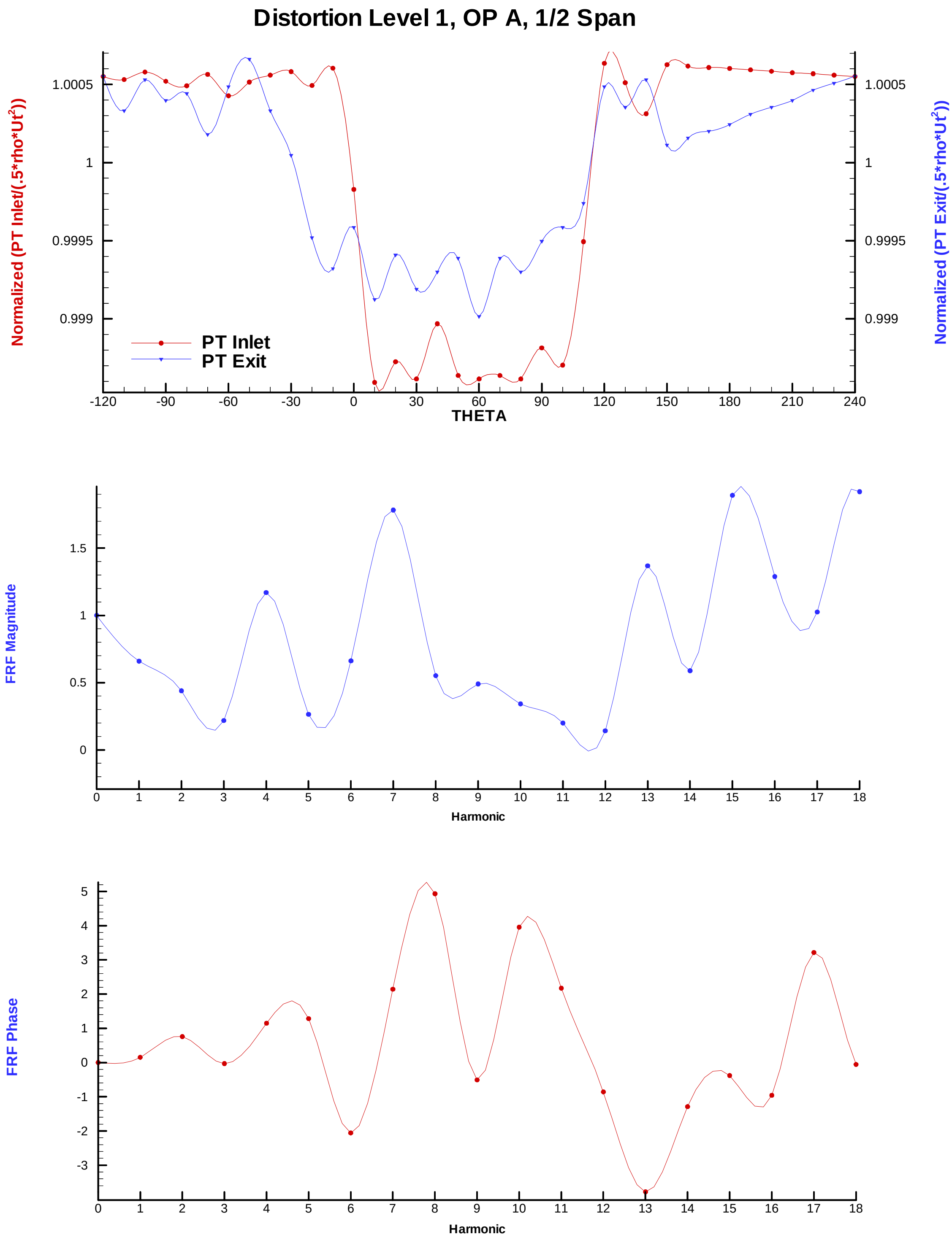

Figure B.3: FRF for Level 1 Distortion, Operating Point A, at 1/2 Span

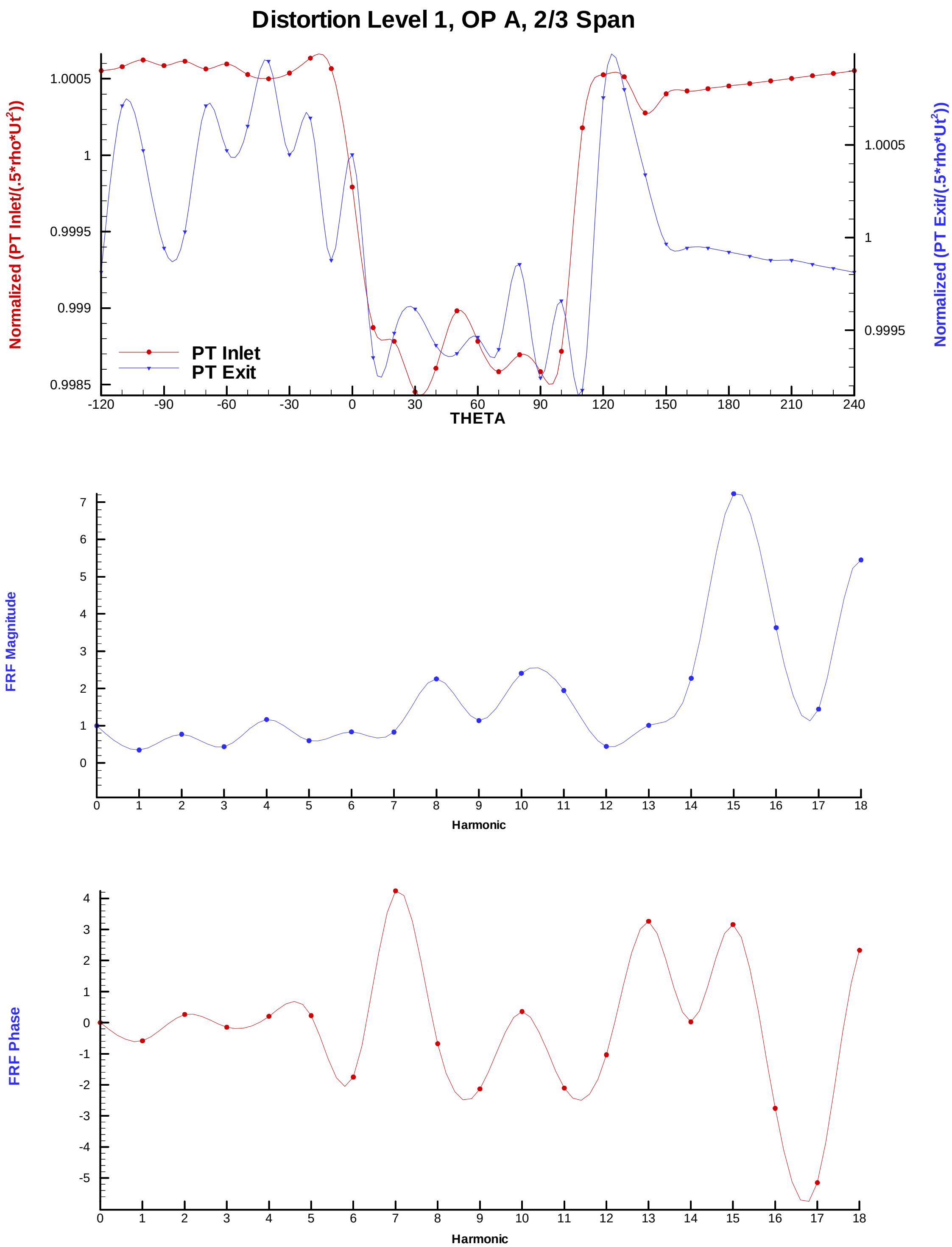

Figure B.4: FRF for Level 1 Distortion, Operating Point A, at 2/3 Span

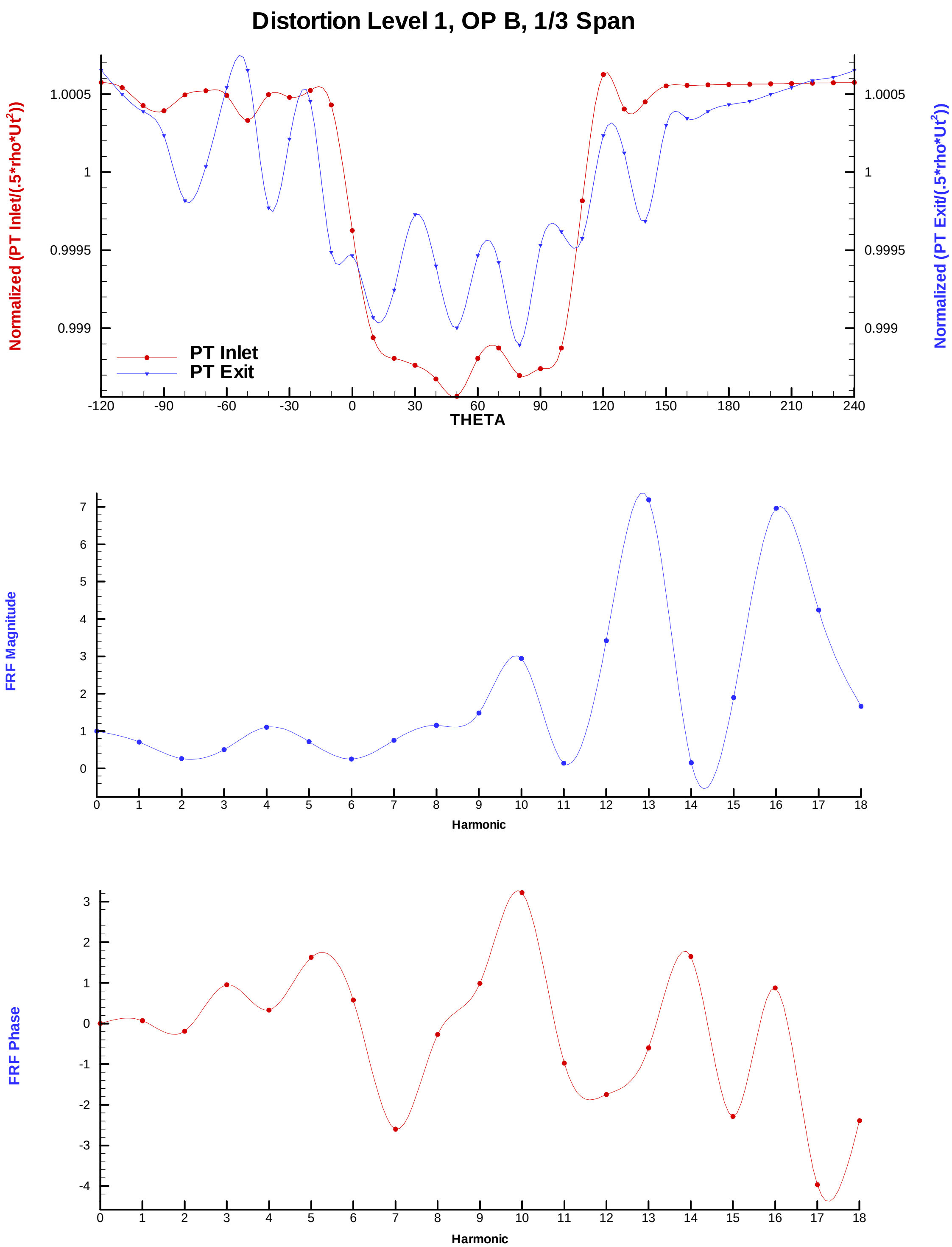

Figure B.5: FRF for Level 1 Distortion, Operating Point B, at 1/3 Span

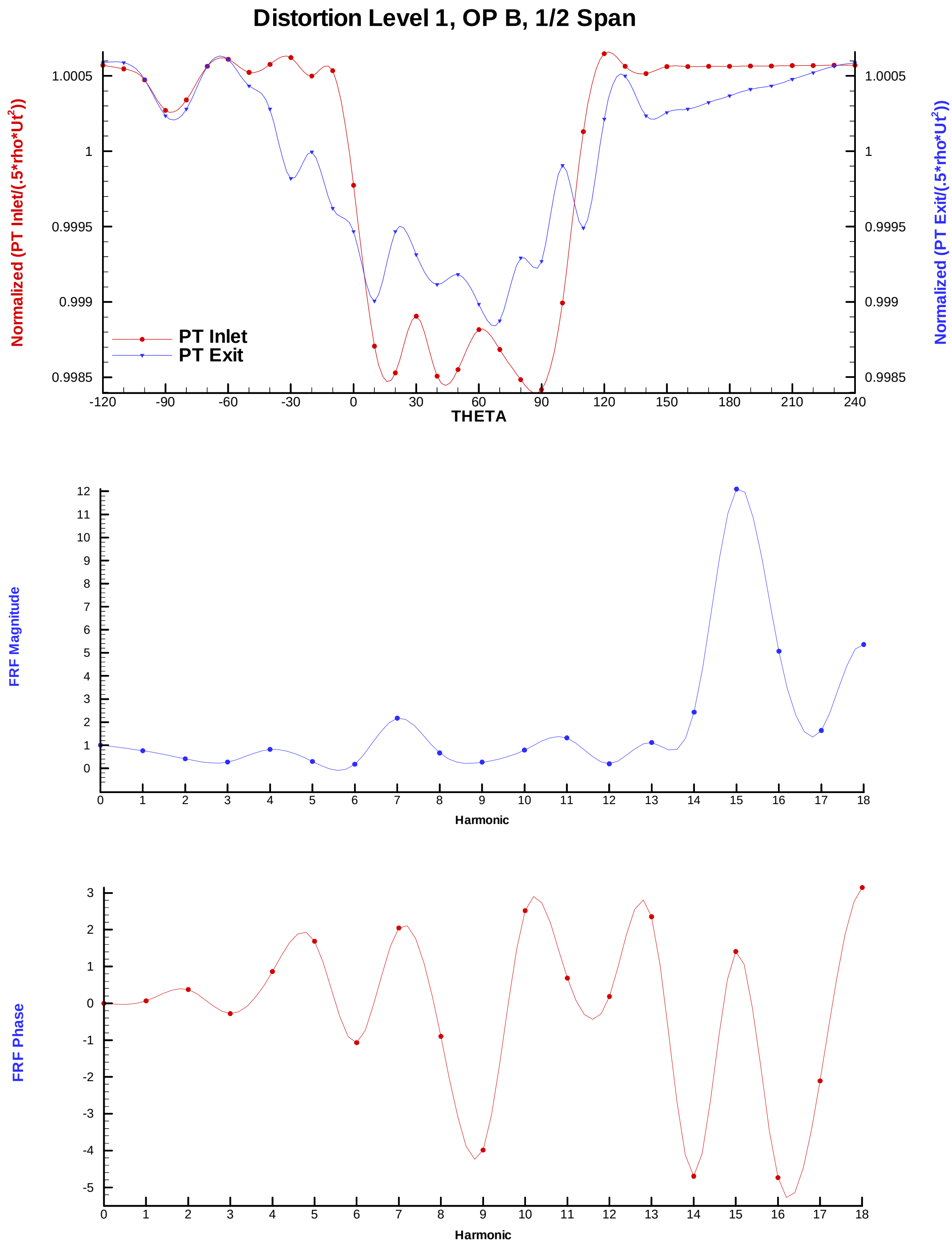

Figure B.6: FRF for Level 1 Distortion, Operating Point B, at 1/2 Span

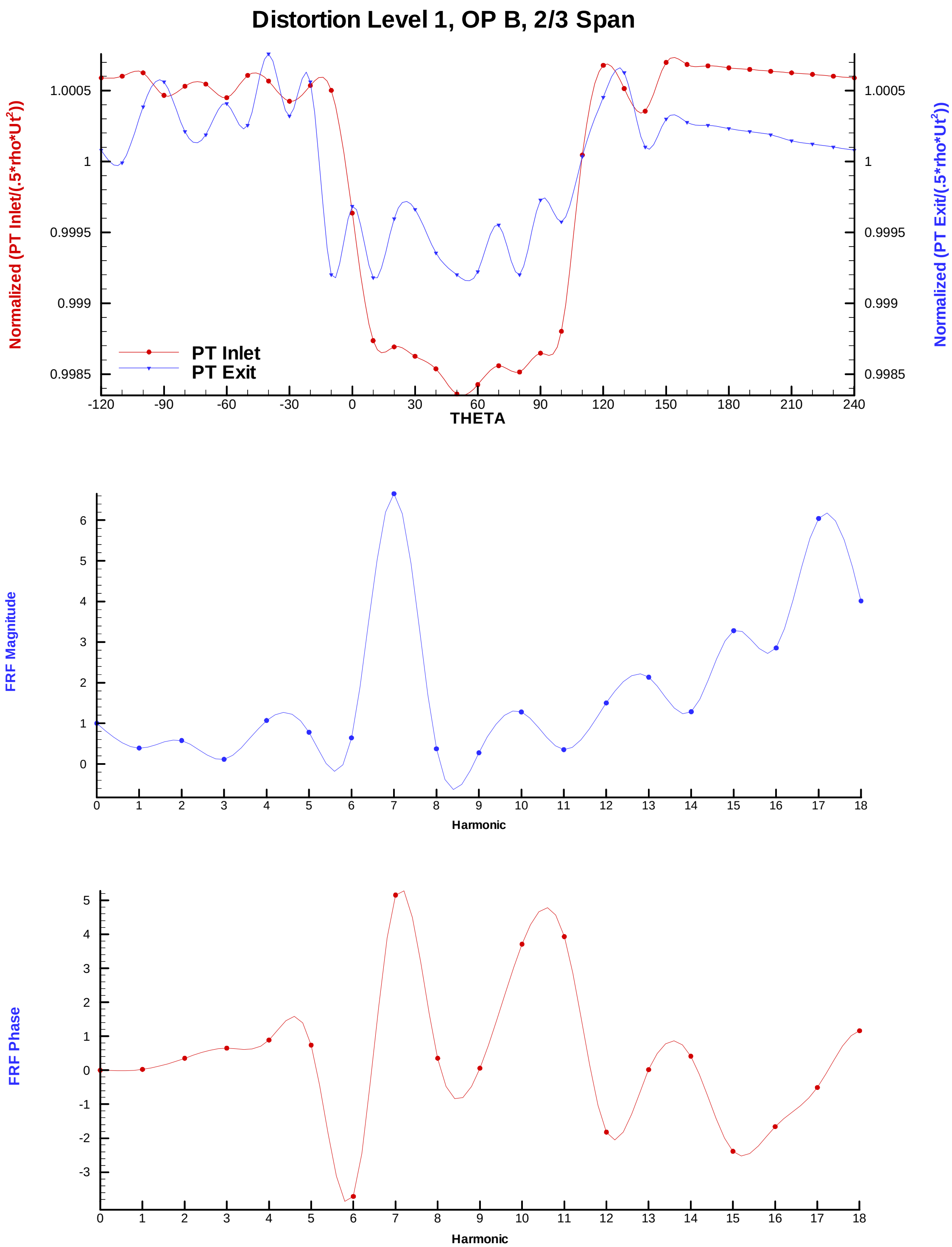

Figure B.7: FRF for Level 1 Distortion, Operating Point B, at 2/3 Span

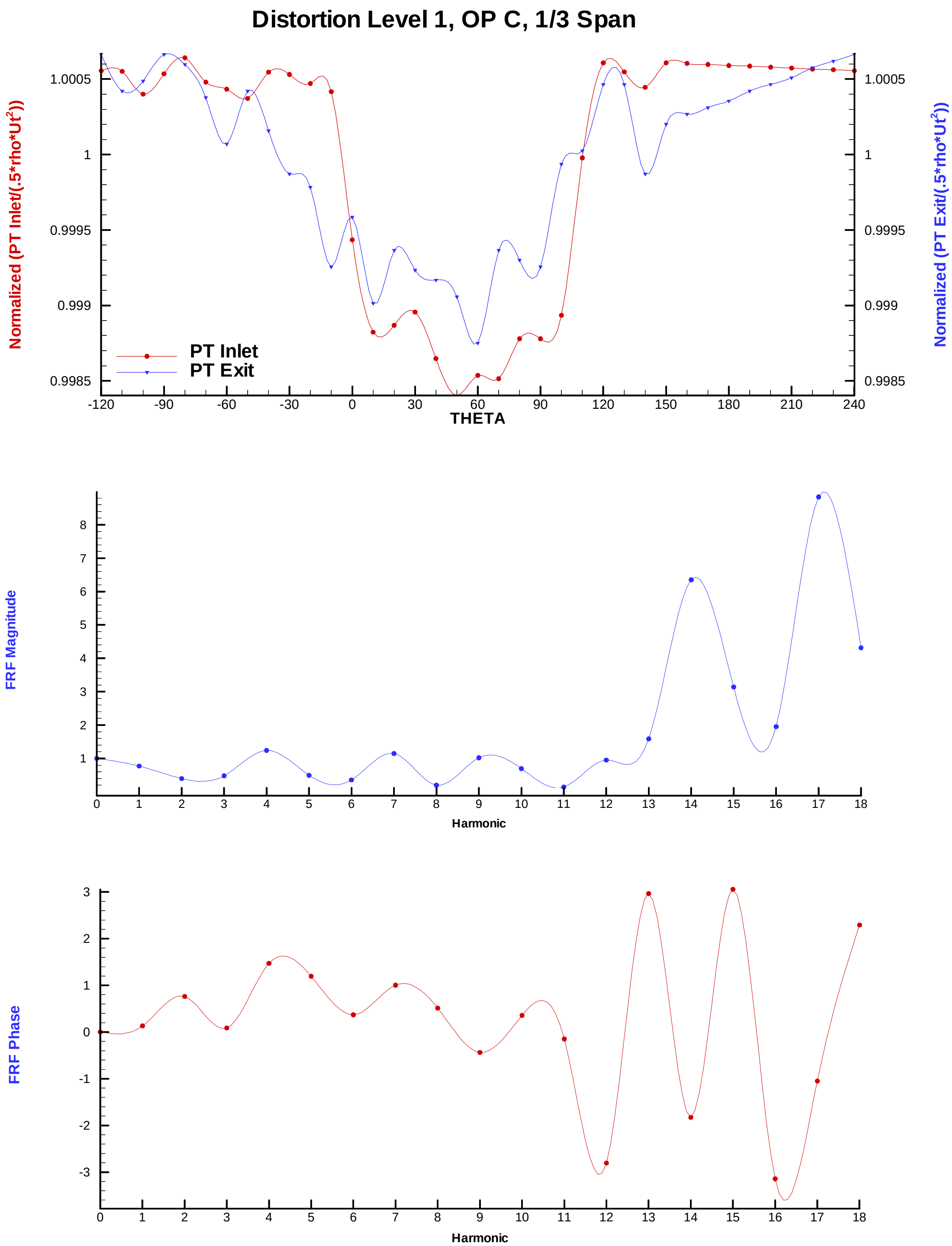

Figure B.8: FRF for Level 1 Distortion, Operating Point C, at 1/3 Span

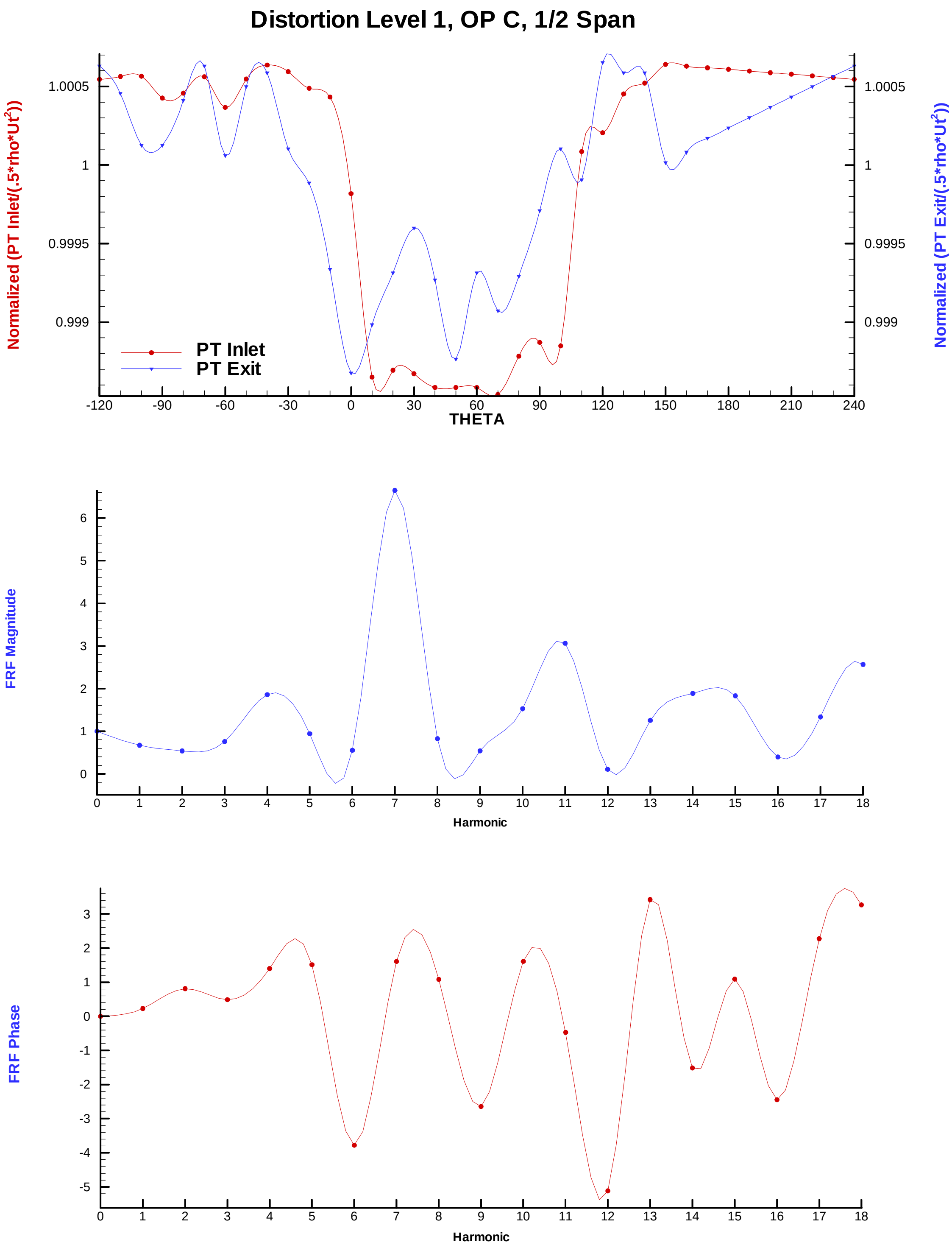

Figure B.9: FRF for Level 1 Distortion, Operating Point C, at 1/2 Span

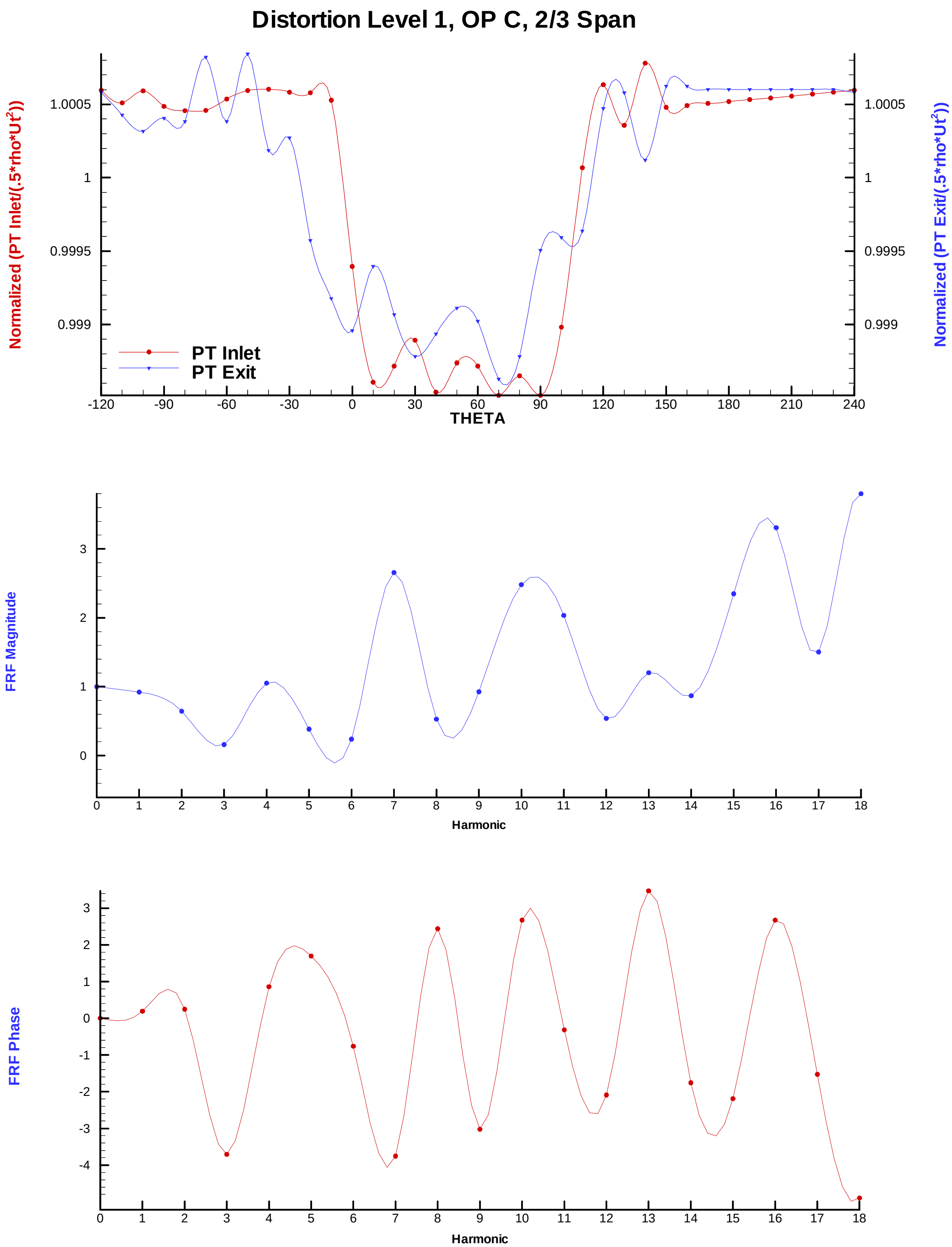

Figure B.10: FRF for Level 1 Distortion, Operating Point C, at 2/3 Span

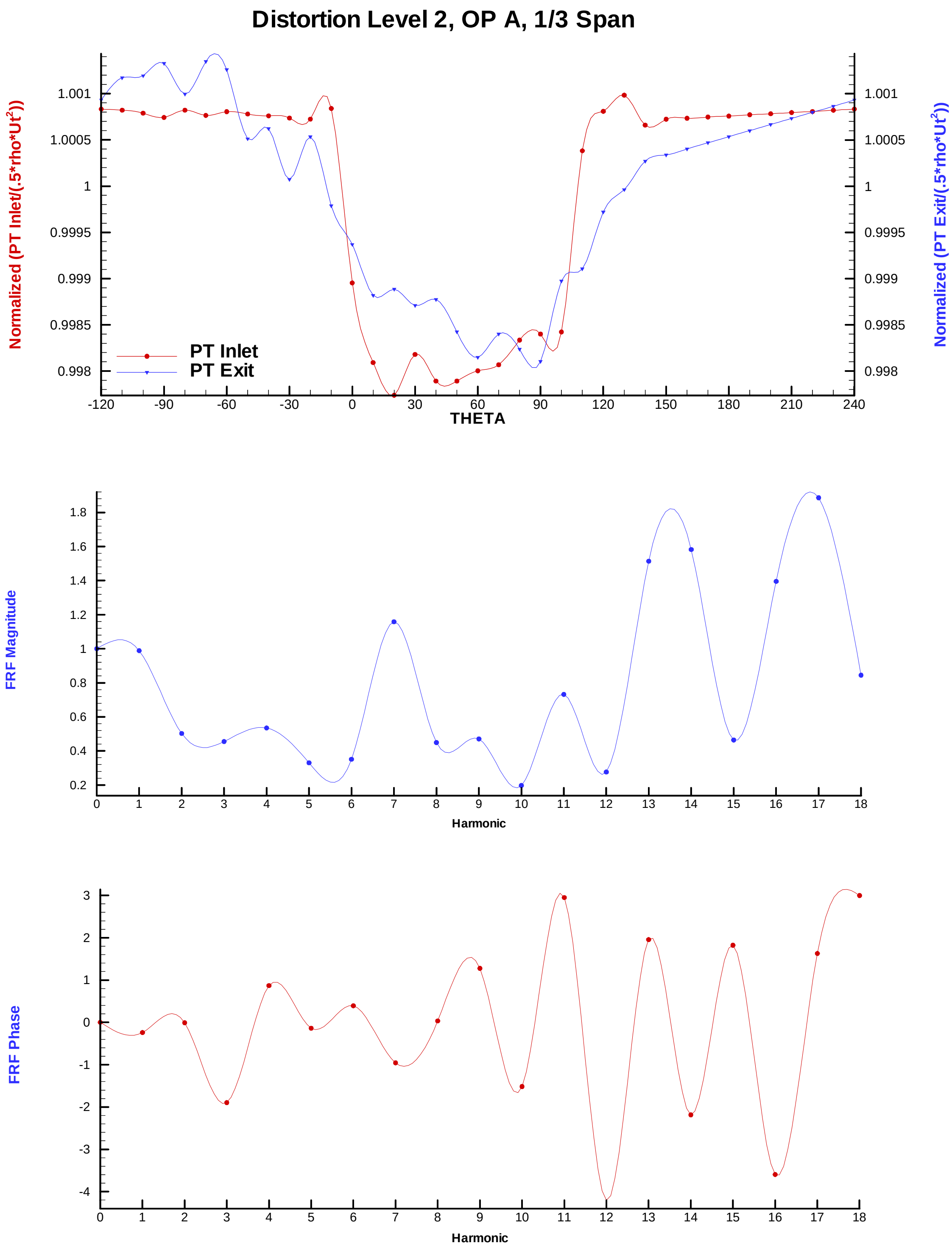

Figure B.11: FRF for Level 2 Distortion, Operating Point A, at 1/3 Span

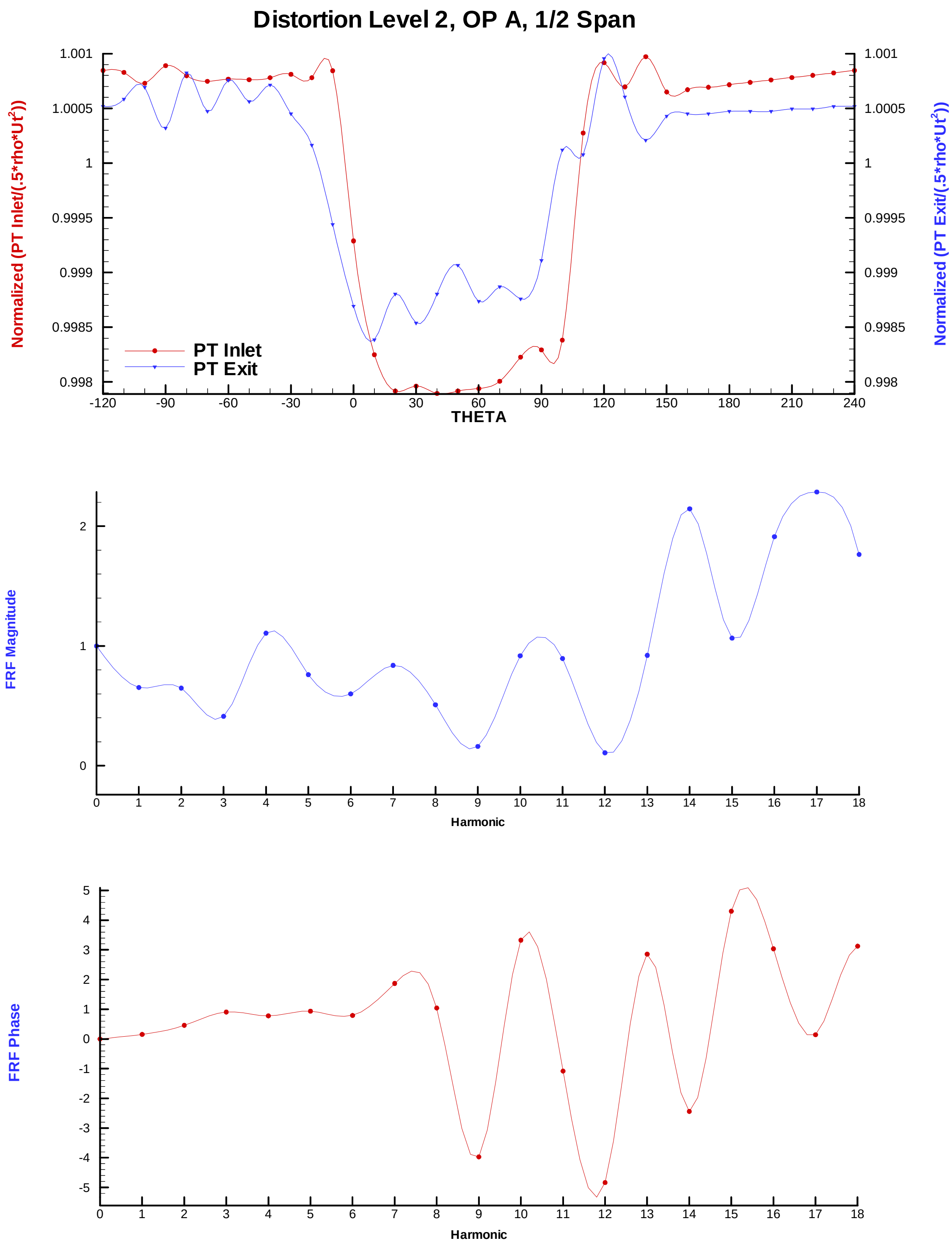

Figure B.12: FRF for Level 2 Distortion, Operating Point A, at 1/2 Span

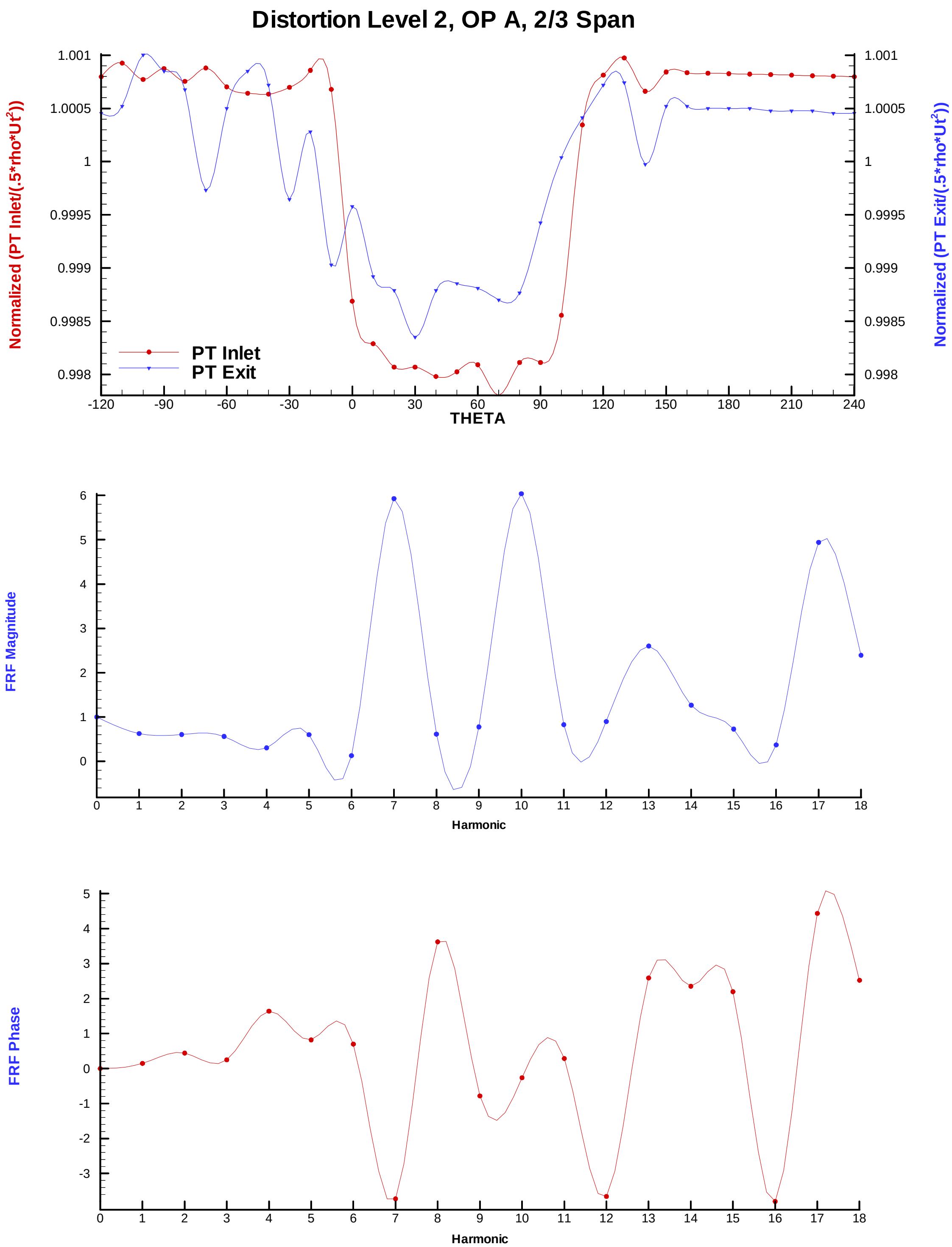

Figure B.13: FRF for Level 2 Distortion, Operating Point A, at 2/3 Span

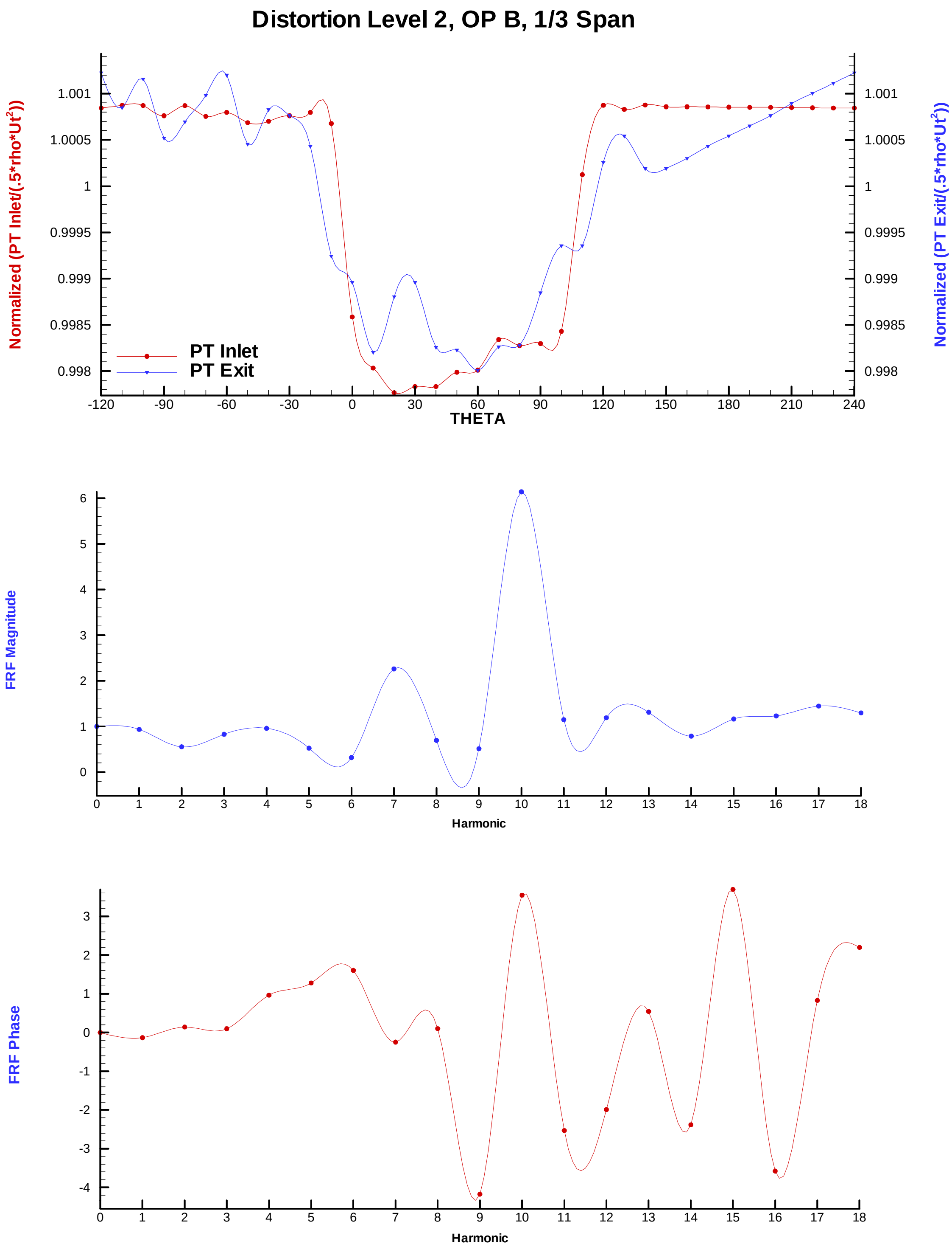

Figure B.14: FRF for Level 2 Distortion, Operating Point B, at 1/3 Span

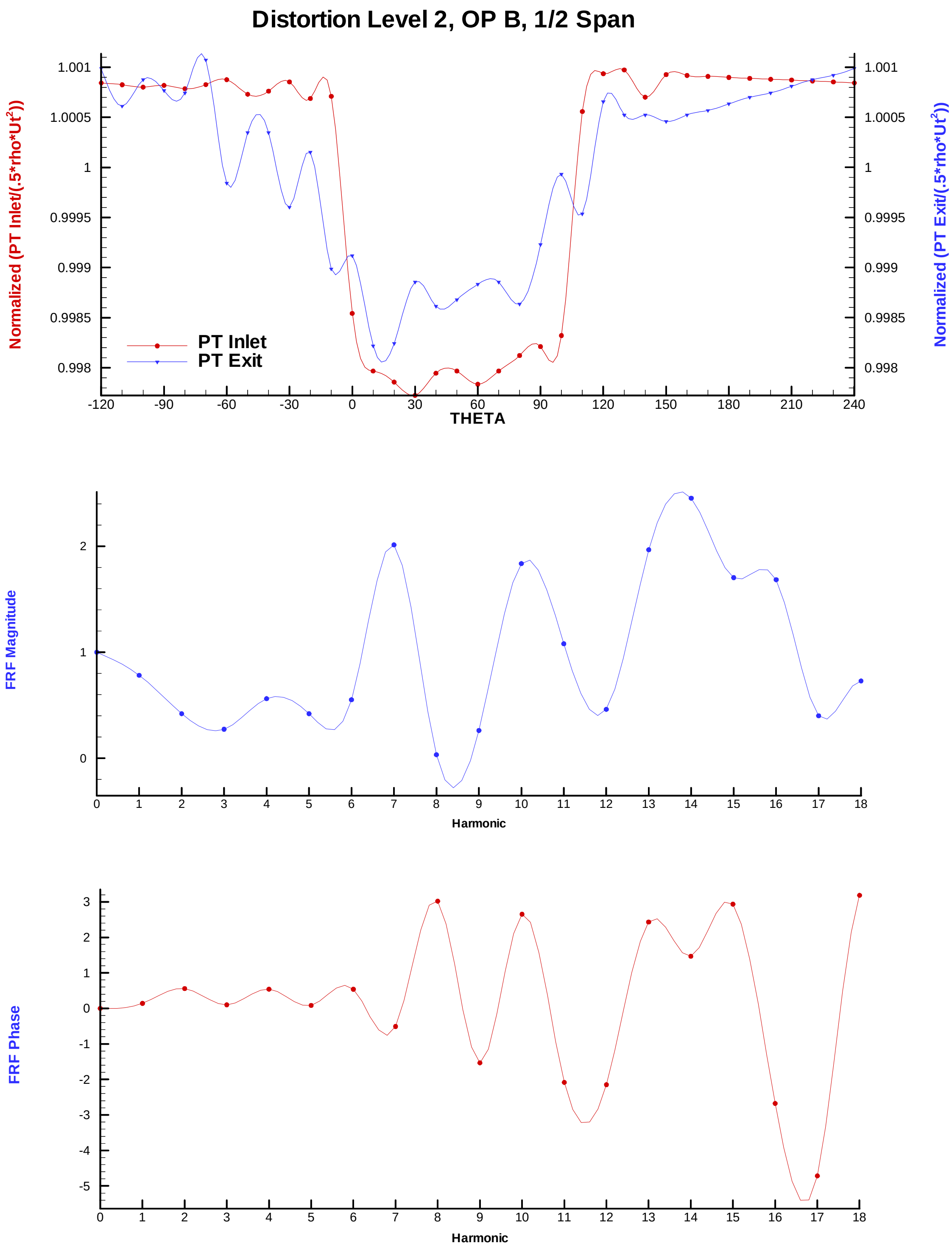

Figure B.15: FRF for Level 2 Distortion, Operating Point B, 1/2 Span

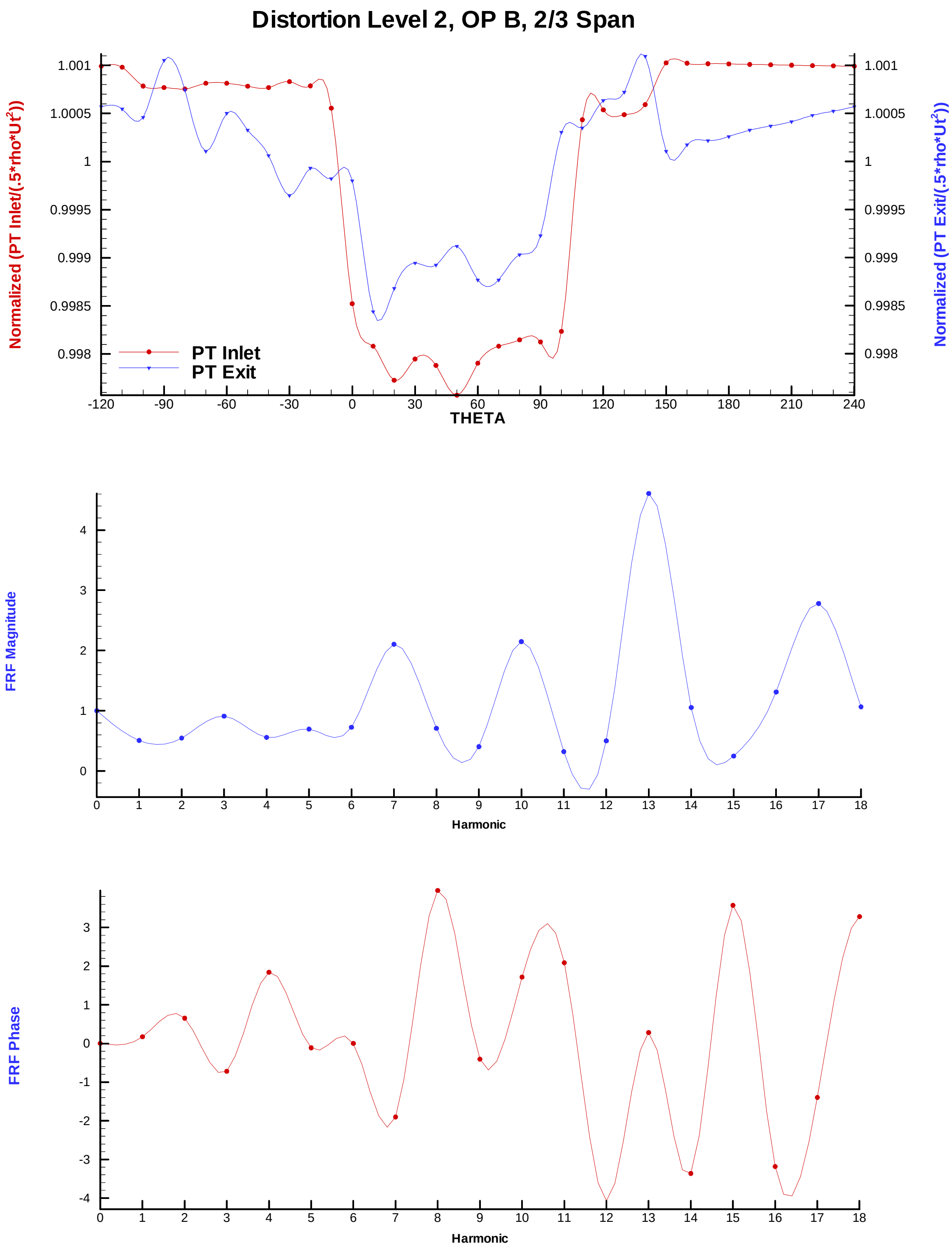

Figure B.16: FRF for Level 2 Distortion, Operating Point B, at 2/3 Span

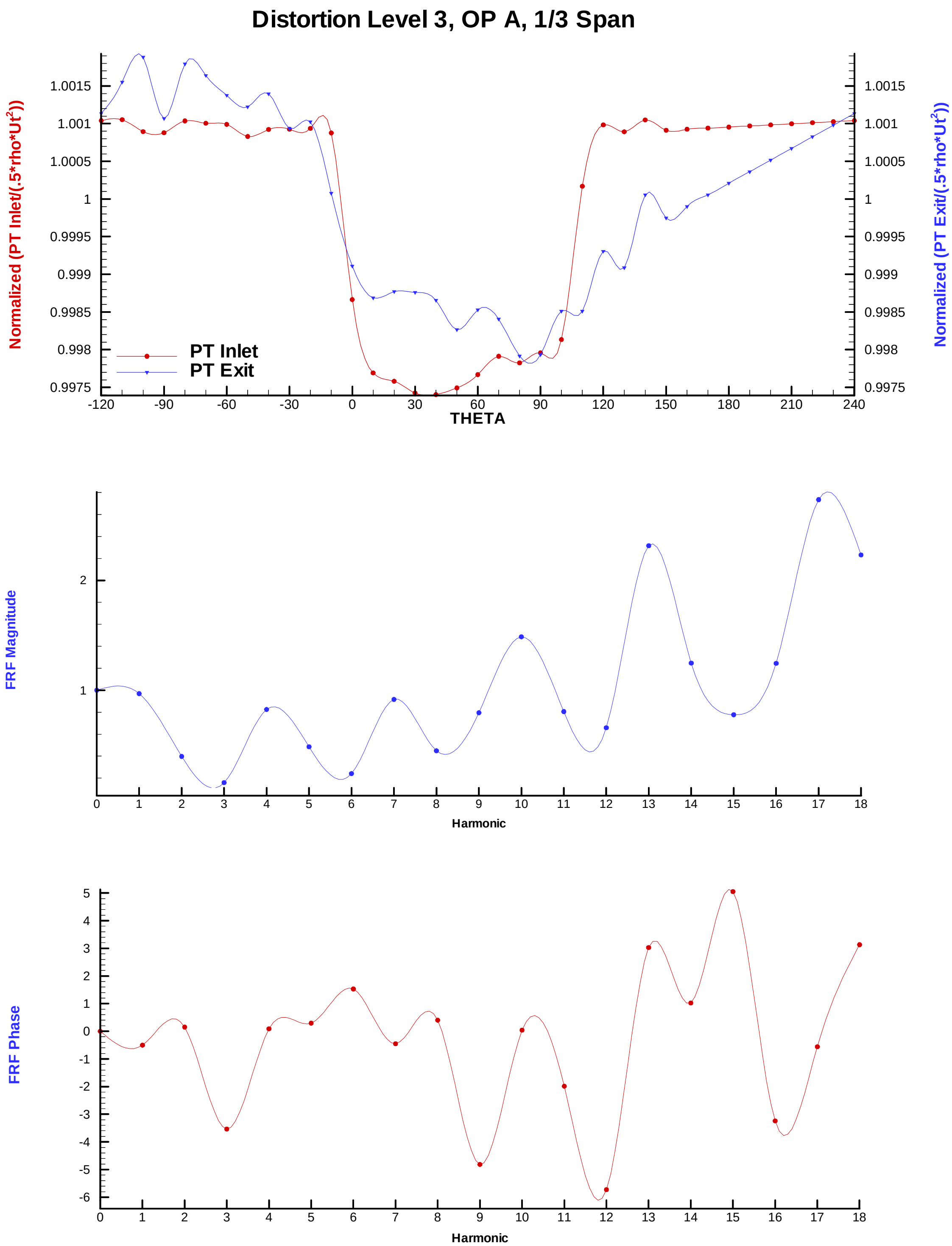

Figure B.17: FRF for Level 3 Distortion, Operating Point A, at 1/3 Span

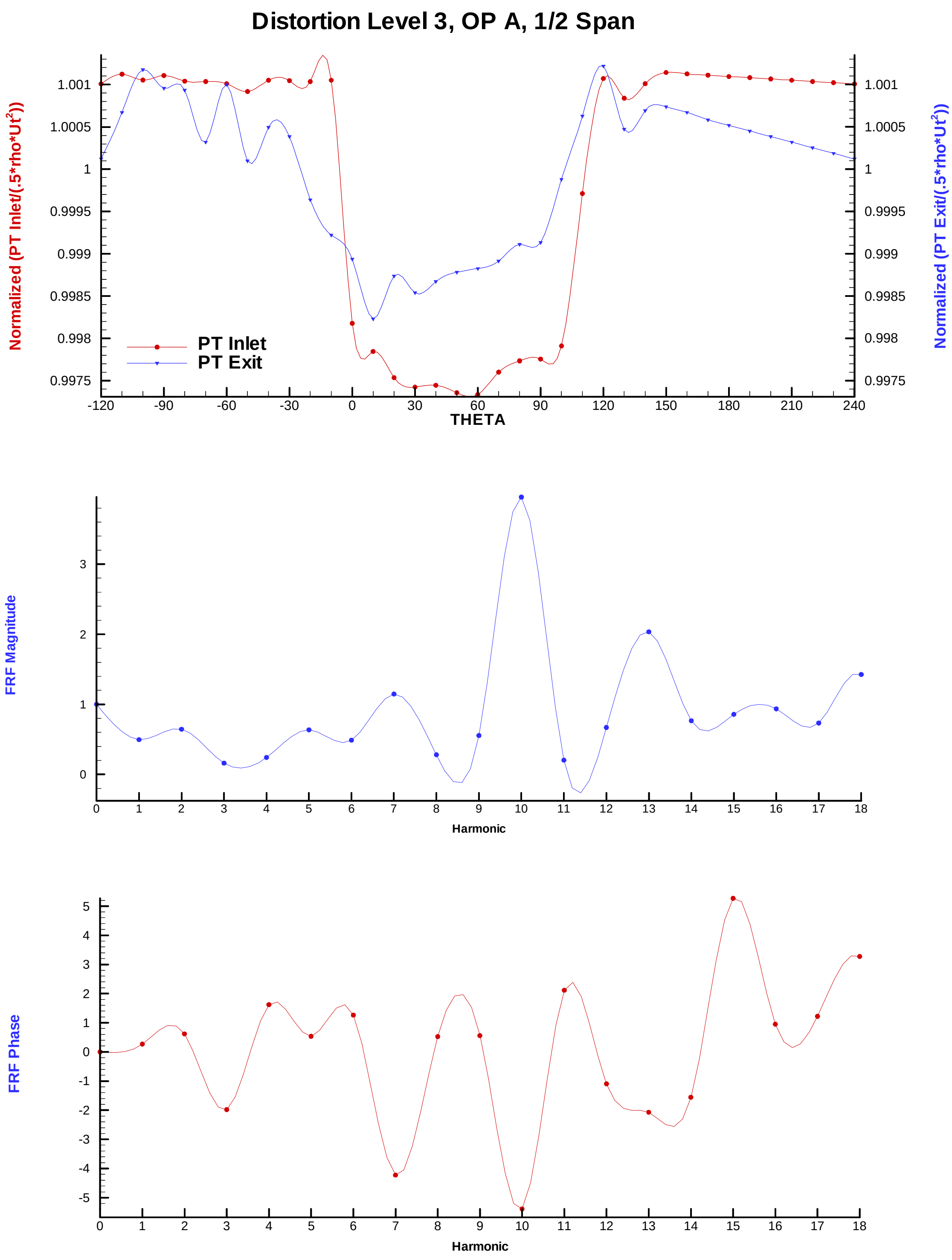

Figure B.18: FRF for Level 3 Distortion, Operating Point A, at 1/2 Span

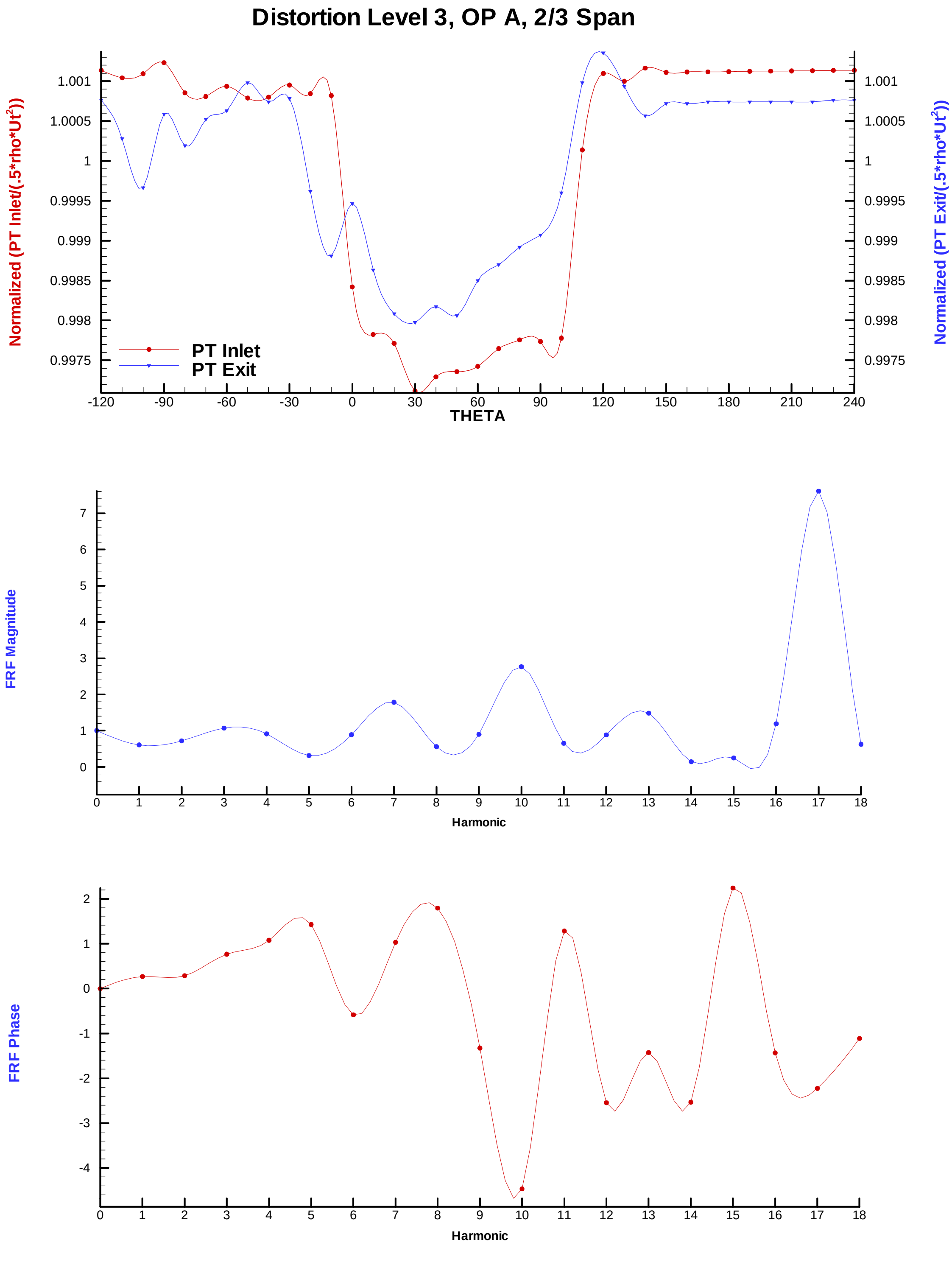

Figure B.19: FRF for Level 3 Distortion, Operating Point A, at 2/3 Span

12 Appendix C

'Common-Loading' Frequency Response Functions and Resulting Exit P_t Predictions

Common-Loading FRF's:

Exit Total Pressure Predictions:

Figure C.1: Location of FRF's and Exit P_t Predictions

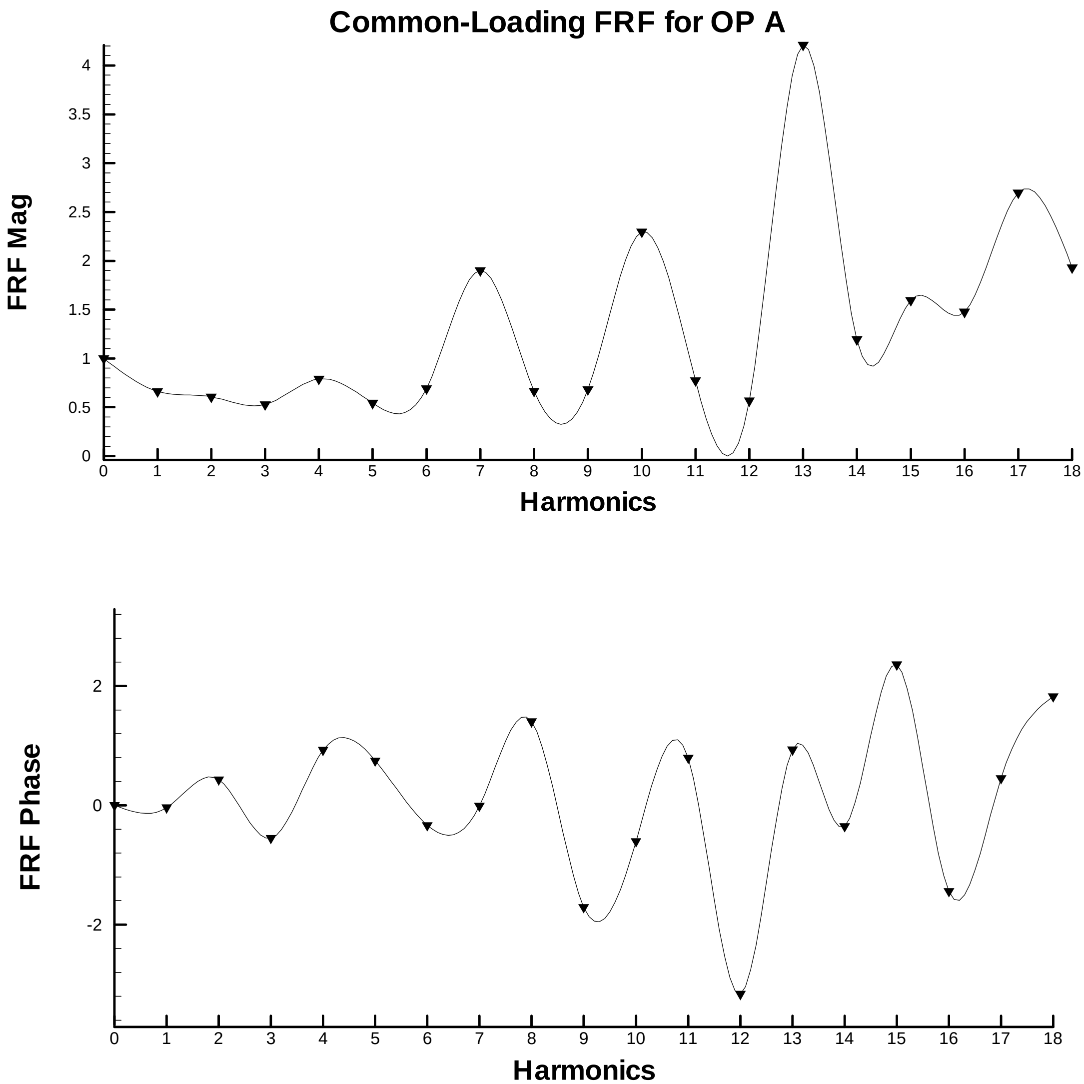

Figure C.2: Common-Loading FRF for Operating Point A

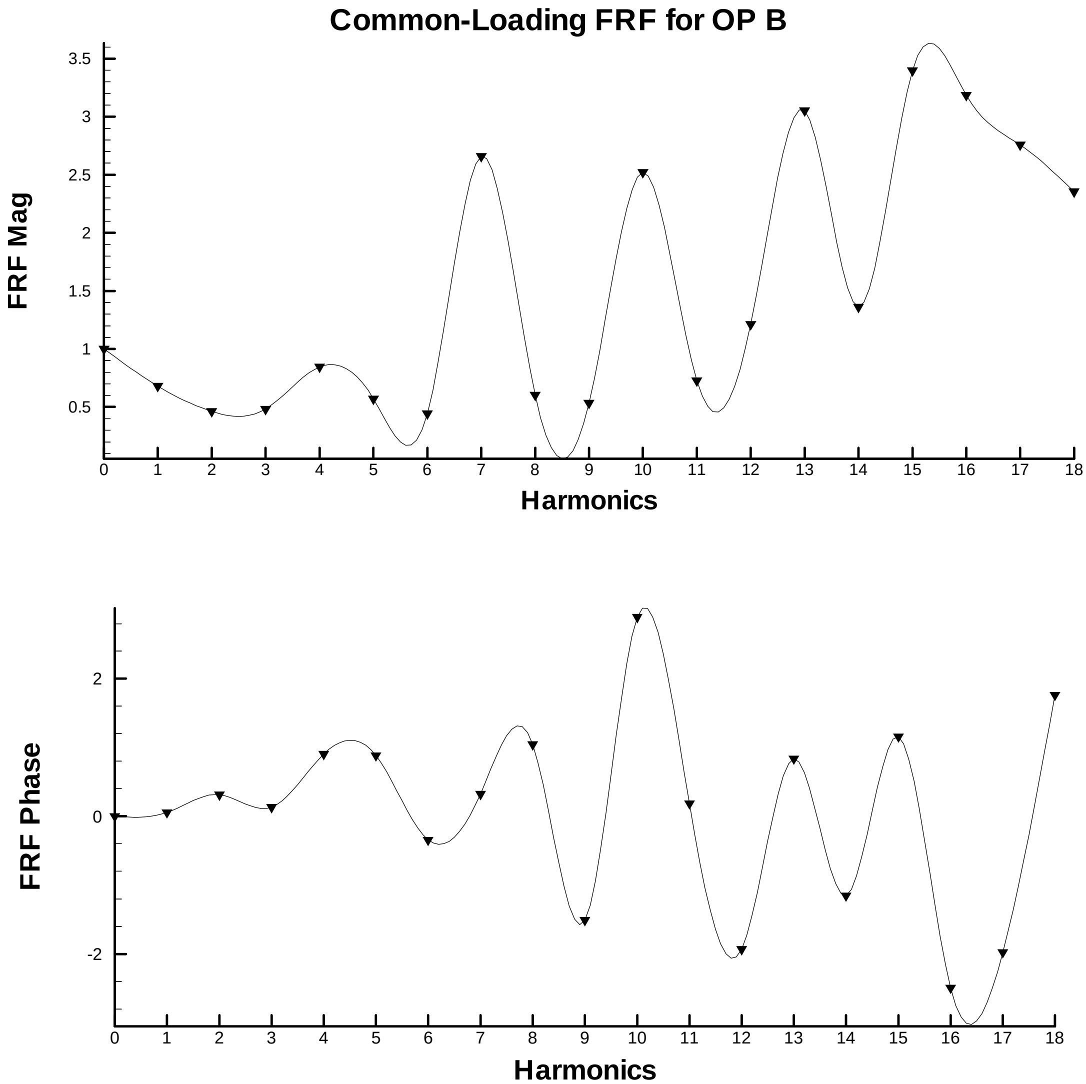

Figure C.3: Common-Loading FRF for Operating Point B

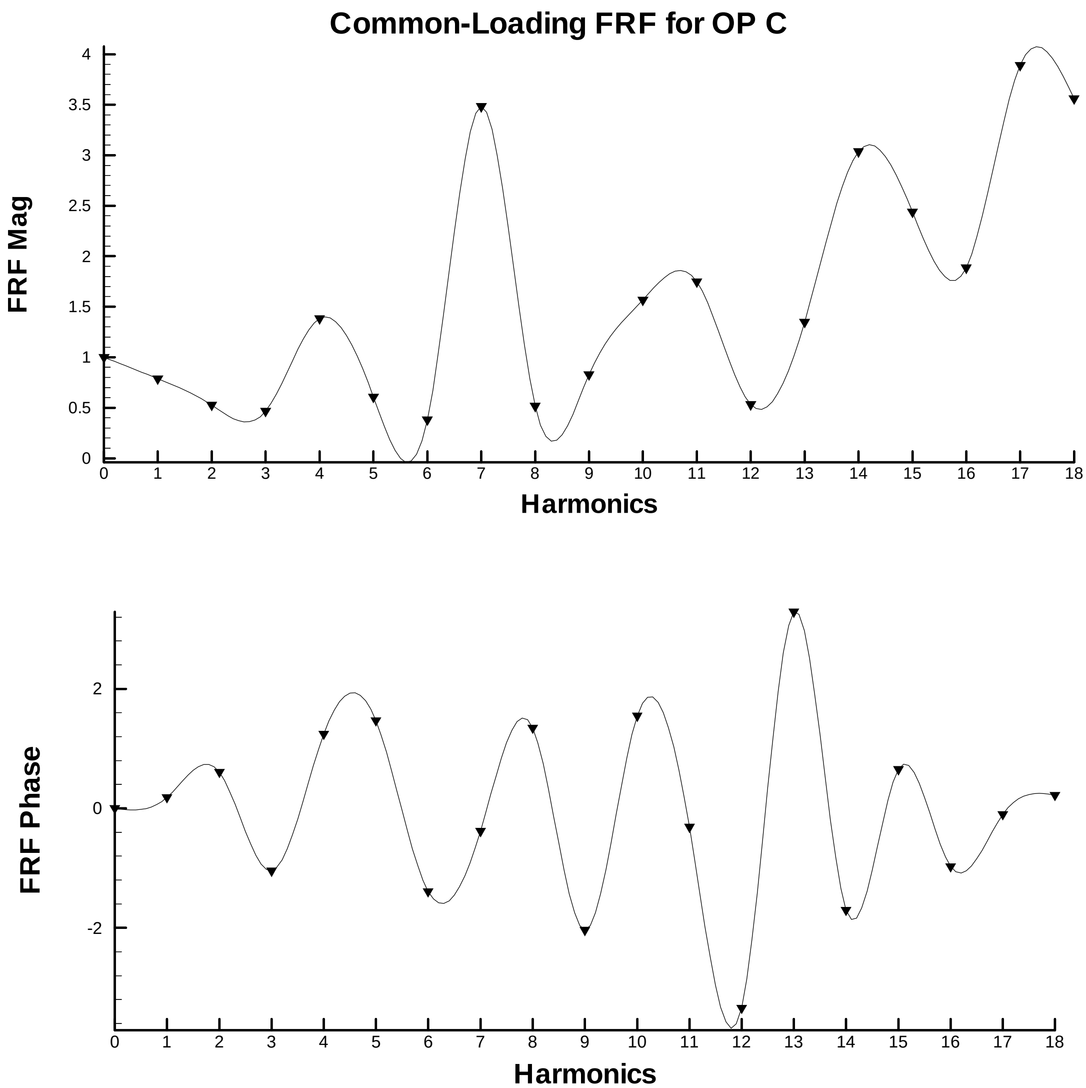

Figure C.4: Common-Loading FRF for Operating Point C

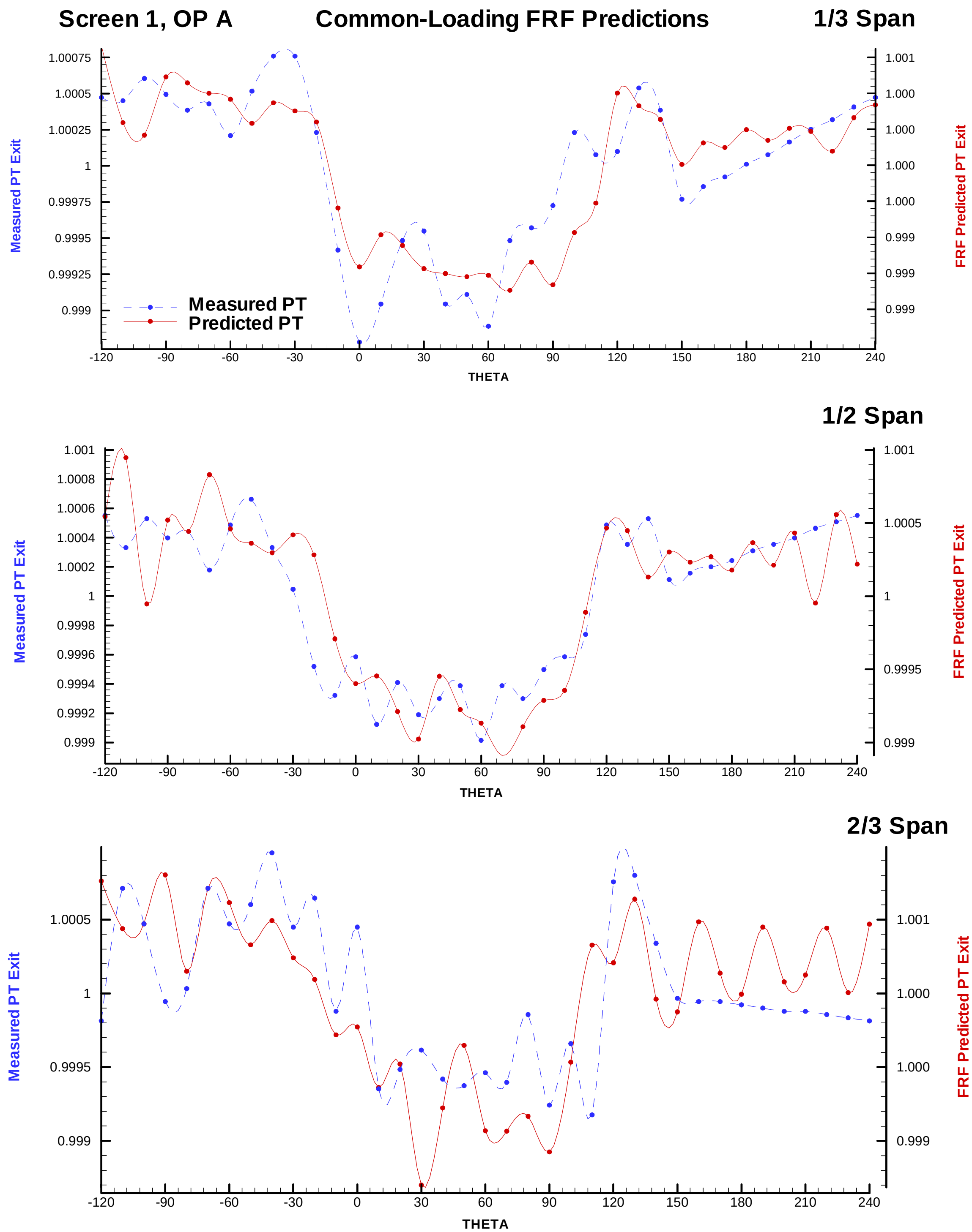

Figure C.5: FRF-Predicted Exit Total Pressure for Level 1 Distortion, Operating Point A, All Spans

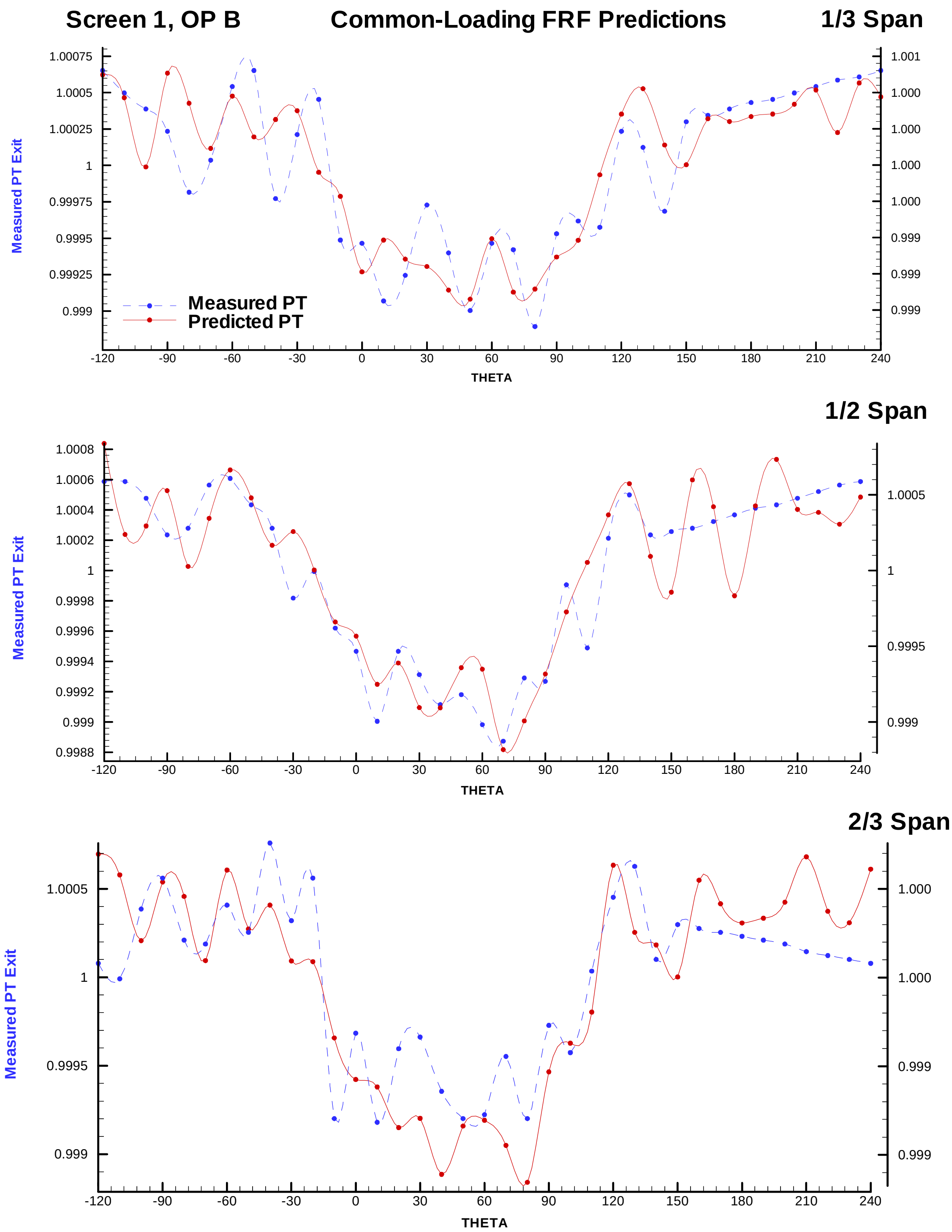

Figure C.6: FRF-Predicted Exit Total Pressure for Level 1 Distortion, Operating Point B, All Spans

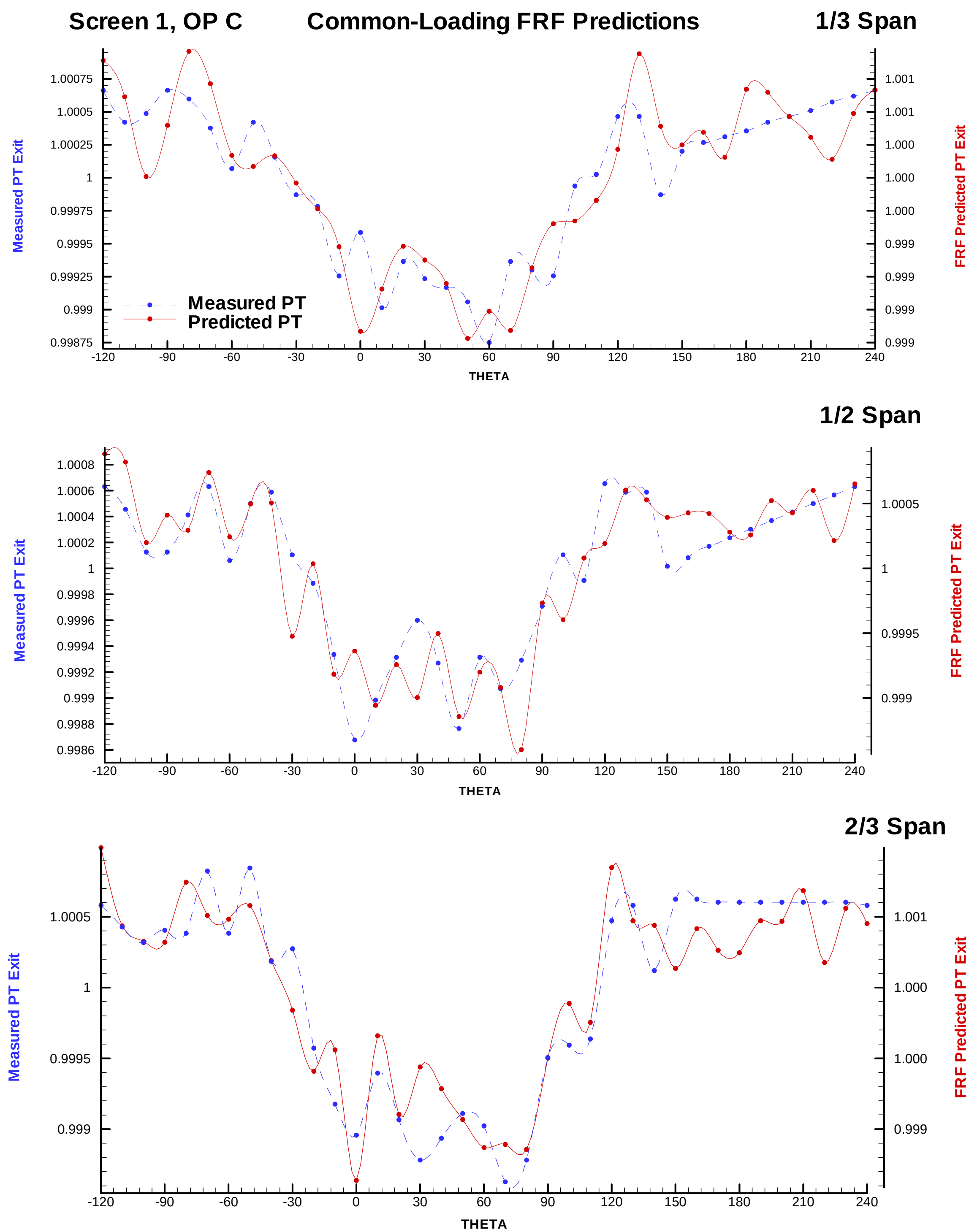

Figure C.7: FRF-Predicted Exit Total Pressure for Level 1 Distortion, Operating Point C, All Spans

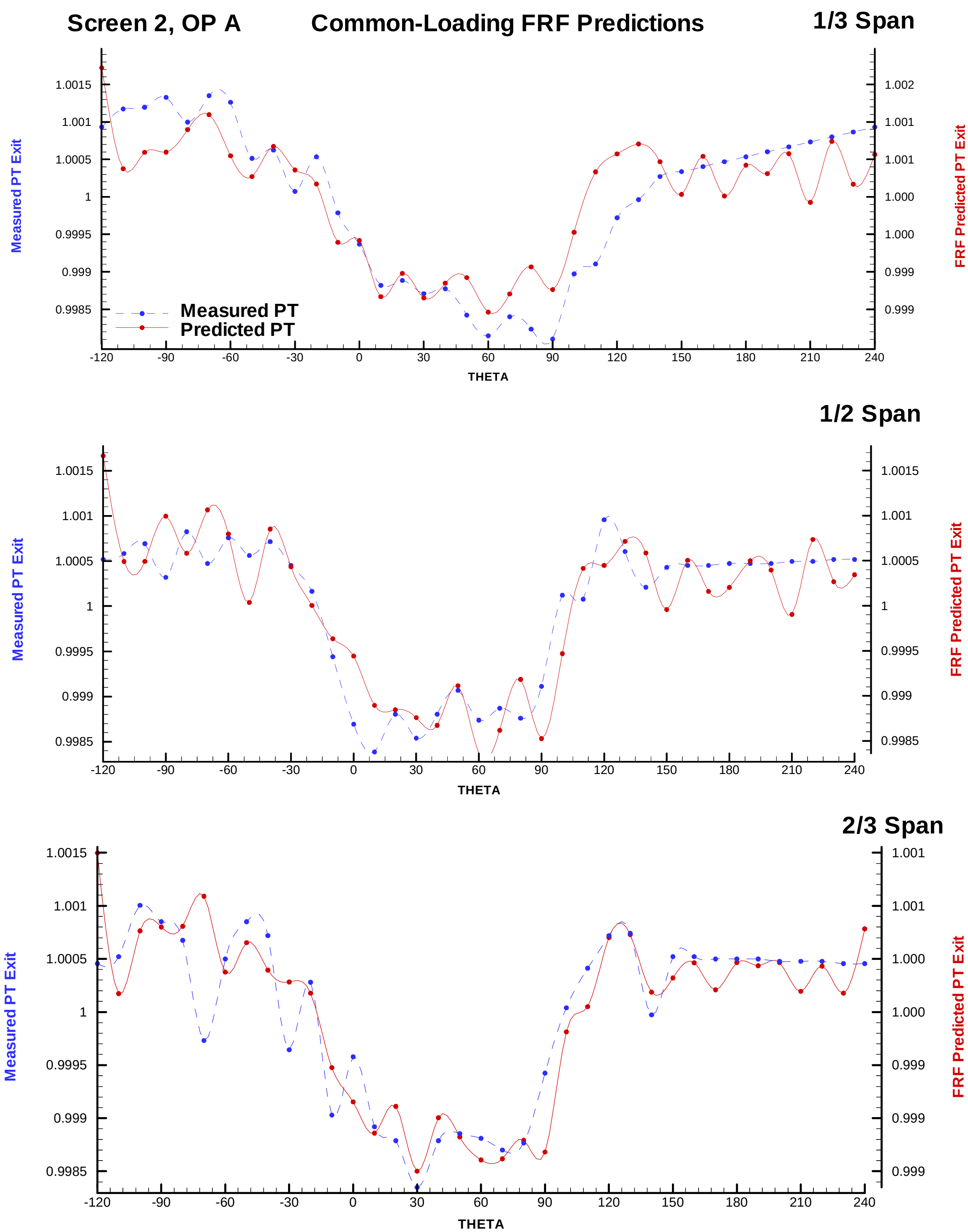

Figure C.8: FRF-Predicted Exit Total Pressure for Level 2 Distortion, Operating Point A, All Spans

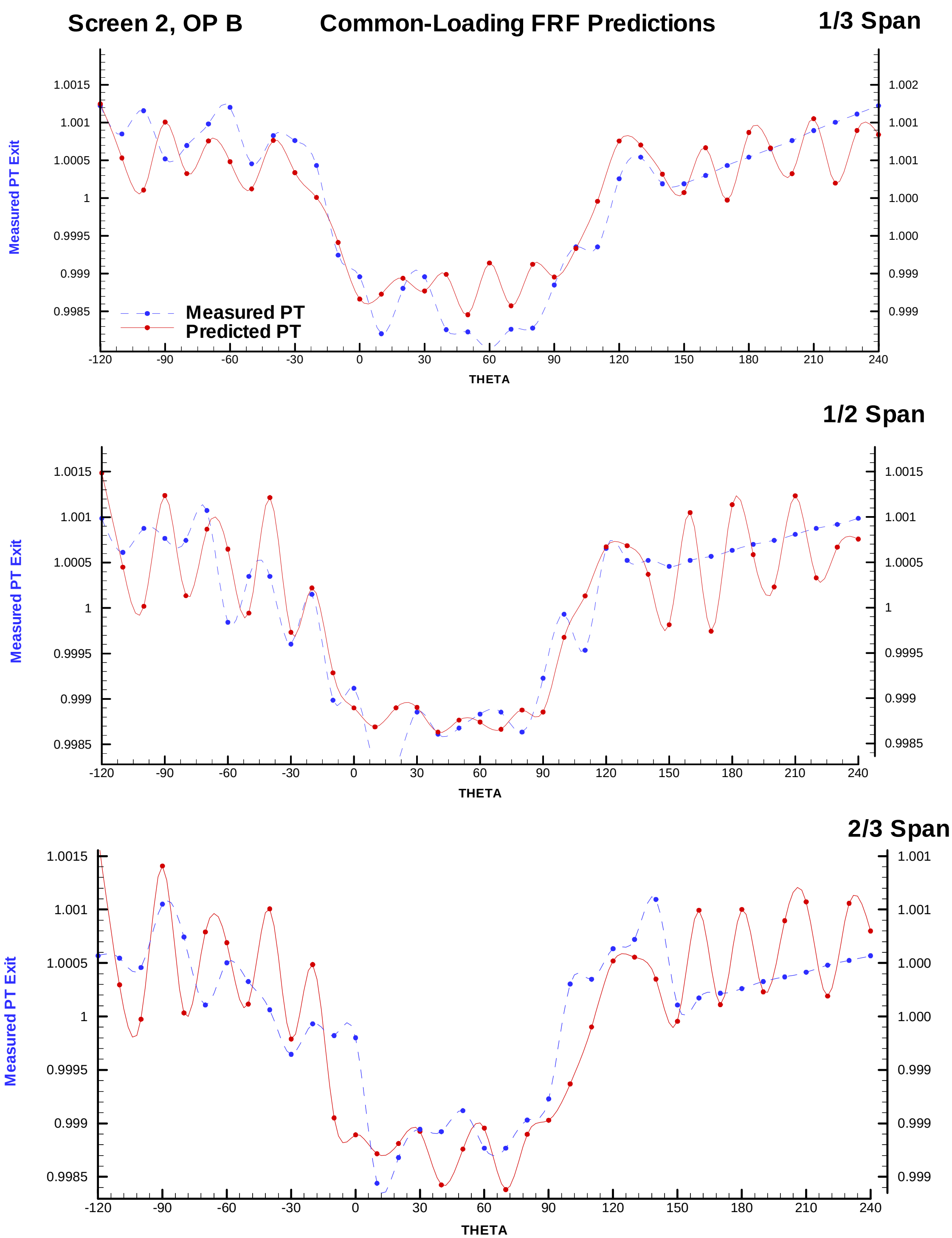

Figure C.9: FRF-Predicted Exit Total Pressure for Level 2 Distortion, Operating Point B, All Spans

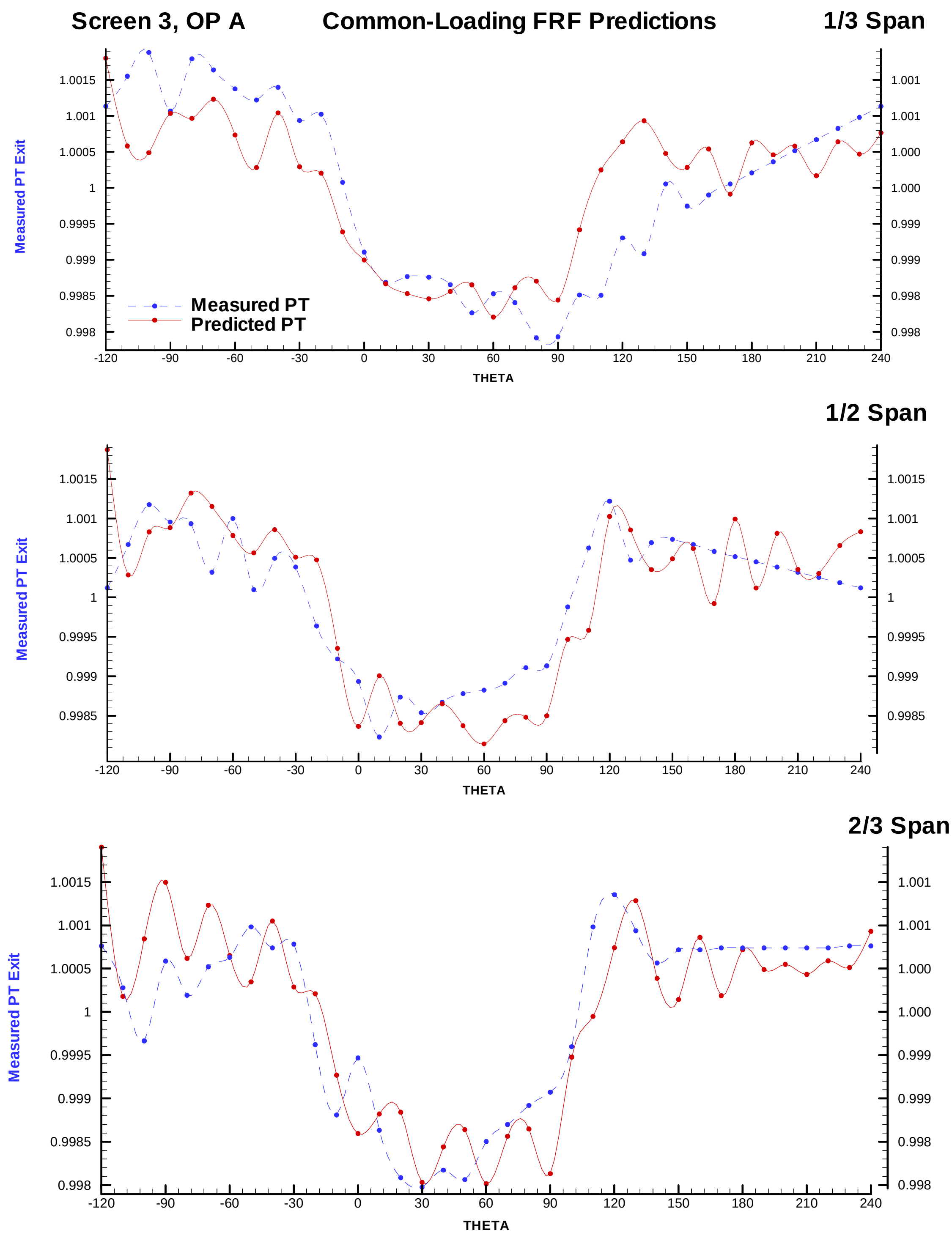

Figure C.10: FRF-Predicted Exit Total Pressure for Level 3 Distortion, Operating Point A, All Spans

13 APPENDIX D

Measurement Uncertainty Analysis

This appendix presents an analysis of the measurement uncertainty for the inlet and exit flow measurements using the procedure of Kline and McClintock (1953), and is presented as Boller (1998) described with applicable changes made to fit the current work. This approach estimates experimental value uncertainty by summing the squares of the contributions of error from measured quantities and taking the square root of the sum to provide the final uncertainty of the experimental value (propagation of uncertainty).

Uncertainty in Five-Hole Probe Measurements

The uncertainty calculations for the five-hole probe are identical to those of Drost (1994). The magnitude of the velocity is calculated according to the equation

$$V = \sqrt{\frac{2}{\rho}(p_1 - \bar{p})(1 + Cp_{static} - Cp_{total})} \qquad \textbf{(D.1)}$$

and the uncertainty of the velocity is given by

$$W_v = \sqrt{(\frac{\partial V}{\partial \rho}W_\rho)^2 + (\frac{\partial V}{\partial p_1}W_{p_1})^2 + (\frac{\partial V}{\partial \bar{p}}W_{\bar{p}})^2 + (\frac{\partial V}{\partial Cp_{static}}WC_{p\,static})^2 + (\frac{\partial V}{\partial Cp_{total}}W_{Cp_{total}})^2}$$

(D.2)

Drost approximated the partial derivatives by perturbing his data reduction program and observing the effects. Partial derivatives were found using the formula

$$\frac{\partial V}{\partial x} = \frac{V(x + \Delta x) - V(x)}{\Delta x} \qquad \textbf{(D.3)}$$

with V as a dependent variable and x an independent variable perturbed in the program. The maximal values were found by entering the following data with large angle variations

$$\frac{\partial V}{\partial \rho} = -10.4755 \frac{m/s}{kg/m^3}$$

$$\frac{\partial V}{\partial p_1} = +0.0696 \frac{m/s}{Pa}$$

$$\frac{\partial V}{\partial \bar{p}} = -0.0687 \frac{m/s}{Pa}$$

$$\frac{\partial V}{\partial Cp_{static}} = +11.0653 m/s$$

$$\frac{\partial V}{\partial Cp_{total}} = -11.0653 m/s$$

Solving Equation **(D.2)** required an estimation of the uncertainties in the measurements of the independent variables. Estimate of the uncertainty in the air density is as follows.

According to the ideal gas equation

$$\rho = \frac{p_a}{R \cdot T_a} \quad \textbf{(D.4)}$$

therefore the uncertainty in the density is

$$W_p = \sqrt{\left(\frac{\partial \rho}{\partial p_a} W_{p_a}\right)^2 + \left(\frac{\partial \rho}{\partial T_a} W_{T_a}\right)^2} \quad \textbf{(D.5)}$$

where the partial derivatives were found by differentiation of Equation **(D.4)** and substituting some typical values.

$$\frac{\partial \rho}{\partial p_a} = \frac{1}{R \cdot T_a} = +0.0000115 \frac{kg/m^3}{Pa}$$

$$\frac{\partial\rho}{\partial T_a} = -\frac{1}{R \cdot T_a{}^2} = -0.0036029\frac{kg/m^3}{K}$$

$W_p = \pm 33.763 Pa$ (0.01 in. H_g)(readability of mercury barometer)

$W_{T\,a} = \pm 0.56 K (\pm 1^\circ F)$ (least readable thermometer)

Substituting the above values into Equation **(D.5)** results in

$$W\rho = 0.00205\frac{kg}{m^3}$$

Assuming a normal distribution about the mean value, an estimate in the measured pressures was made. The uncertainty was expressed in the following manner

$$W = 2\sigma \qquad \textbf{(D.6)}$$

where

$$\sigma = \left(\frac{\sum_{i=1}^{N}(x_i - \bar{x})^2}{N-1}\right)^2 \qquad \textbf{(D.7)}$$

and

x_i = measured value

$\bar{x}$ = mean of measured value

N = number of samples

Using a sample of 100 pressure values for identical flow conditions and evaluating Equation **(D.6)**, the uncertainty in pressure measurements was found to be

$$W_p = W_{p_1} = W_{\bar{p}} = 4.248 Pa$$

The static and total pressure coefficients are functions of both probe yaw angle β and pitch angle α.

$$Cp_{total} = f(\alpha,\beta)$$

$$Cp_{static} = f(\alpha,\beta) \qquad \textbf{(D.8)}$$

The uncertainties for these coefficients are then

$$W_{Cp_{static}} = \sqrt{\left(\frac{\partial Cp_{static}}{\partial \alpha} W_{\alpha}\right)^2 + \left(\frac{\partial Cp_{static}}{\partial \beta} W_{\beta}\right)^2}$$

(D.9)

$$W_{Cp_{total}} = \sqrt{\left(\frac{\partial Cp_{total}}{\partial \alpha} W_{\alpha}\right)^2 + \left(\frac{\partial Cp_{total}}{\partial \beta} W_{\beta}\right)^2}$$

The partial derivatives in these equations are found by inspection of the calibration data and selection of the highest apparent values.

$$\frac{\partial Cp_{static}}{\partial \alpha} = -0.02175 \frac{1}{\deg}$$

$$\frac{\partial Cp_{static}}{\partial \beta} = +0.04042 \frac{1}{\deg}$$

$$\frac{\partial Cp_{total}}{\partial \alpha} = -0.02325 \frac{1}{\deg}$$

$$\frac{\partial Cp_{total}}{\partial \beta} = -0.05312 \frac{1}{\deg}$$

The probe yaw and pitch angles are functions of the five pressures at the probe tip as expressed in terms of yaw and pitch pressure coefficients, the uncertainties of which are found by

$$W_{\alpha} = \sqrt{\left(\frac{\partial \alpha}{\partial Cp_{yaw}} W_{Cp_{yaw}}\right)^2 + \left(\frac{\partial \alpha}{\partial Cp_{pitch}} W_{Cp_{pitch}}\right)^2}$$

(D.10)

$$W_{\beta} = \sqrt{\left(\frac{\partial \beta}{\partial Cp_{yaw}} W_{Cp_{yaw}}\right)^2 + \left(\frac{\partial \beta}{\partial Cp_{pitch}} W_{Cp_{pitch}}\right)^2}$$

The partial derivatives are found in the same manner as mentioned above by inspection of the calibration data.

$$\frac{\partial \alpha}{\partial Cp_{yaw}} = 15.00 \text{ degrees}$$

$$\frac{\partial \alpha}{\partial Cp_{pitch}} = 10.11 \text{ degrees}$$

$$\frac{\partial \beta}{\partial Cp_{yaw}} = 12.41 \text{ degrees}$$

$$\frac{\partial \beta}{\partial Cp_{pitch}} = 9.53 \text{ degrees}$$

Finally, the yaw and pitch pressure coefficients depend on the measured five pressures at the probe tip, which are given by the following relations:

$$Cp_{yaw} = \frac{(P_2 - P_3)}{(P_1 - \bar{P})}$$

$$Cp_{pitch} = \frac{(P_4 - P_5)}{(P_1 - \bar{P})}$$

$$\bar{P} = \frac{(P_2 + P_3 + P_4 + P_5)}{4}$$

As the uncertainty in each of the five pressures was the same, it was the same for the average pressure $\bar{P}$ as well. Therefore, the uncertainty for the yaw and pitch pressure coefficients may be expressed as

$$W_{Cpyaw} = \sqrt{(\frac{\partial Cp_{yaw}}{\partial p_2} W_\rho)^2 + (\frac{\partial Cp_{yaw}}{\partial p_3} W_{p_1})^2 + (\frac{\partial Cp_{yaw}}{\partial p_1} W_p)^2 + (\frac{\partial Cp_{yaw}}{\partial \bar{p}} W_p)^2} \qquad \textbf{(D.12)}$$

$$W_{Cppitch} = \sqrt{(\frac{\partial Cp_{pitch}}{\partial p_4} W_\rho)^2 + (\frac{\partial Cp_{pitch}}{\partial p_5} W_{p_1})^2 + (\frac{\partial Cp_{pitch}}{\partial p_1} W_p)^2 + (\frac{\partial Cp_{pitch}}{\partial \bar{p}} W_p)^2}$$

Where

$Wp = Wp_1 = Wp_2 = Wp_3 = Wp_4 = Wp_5 = W\bar{p} = 4.248$ Pa

The partial derivatives from **(D.12)** were found by perturbing the cubic spline data evaluation program described in Appendix F using input data for a variety of flow angle combinations, with maximal values as follows:

$$\frac{\partial Cp_{yaw}}{\partial p_2} = +0.0047 \frac{1}{Pa}$$

$$\frac{\partial Cp_{yaw}}{\partial p_3} = -0.0091 \frac{1}{Pa}$$

$$\frac{\partial Cp_{yaw}}{\partial p_1} = +0.0184 \frac{1}{Pa}$$

$$\frac{\partial Cp_{yaw}}{\partial \bar{p}} = -0.0200 \frac{1}{Pa}$$

$$\frac{\partial Cp_{pitch}}{\partial p_4} = +0.0041 \frac{1}{Pa}$$

$$\frac{\partial Cp_{pitch}}{\partial p_5} = -0.0047 \frac{1}{Pa}$$

$$\frac{\partial Cp_{pitch}}{\partial p_1} = +0.0014 \frac{1}{Pa}$$

$$\frac{\partial Cp_{pich}}{\partial \bar{p}} = -0.0015 \frac{1}{Pa}$$

Now based on **(D.12)** the yaw and pitch pressure coefficient uncertainties may be obtained:

$$W_{Cp_{yaw}} = 0.04498$$

$$W_{Cp_{pitch}} = 0.02762$$

Using **(D.10)** the uncertainties in yaw and pitch angle are obtained as

$$W_{\beta} = 0.62 \text{ degrees}$$

$$W_{\alpha} = 0.73 \text{ degrees}$$

Therefore, uncertainties in the yaw and pitch angles round off to 0.25 degrees and 0.95 degrees, respectively. However, the accuracy of probe placement within the annulus was assumed to have a ± 3° uncertainty, and this number was deemed adequate for both yaw and pitch angles.

Now from **(D.9)**

$$W_{Cp_{static}} = 0.02967$$

$$W_{Cp_{static}} = 0.03698$$

Therefore, the uncertainty in velocity using **(D.2)** is

$$W_V = 0.6695 \frac{m}{s}$$

or 0.7 meters per second.

Uncertainty in Performance Measurements

Flow density is calculated according to the ideal gas equation of state

$$\rho = \frac{p_a}{R \cdot T_a} \tag{D.4}$$

therefore the uncertainty in the density is as before

$$W_p = \sqrt{\left(\frac{\partial \rho}{\partial p_a} W_{p_a}\right)^2 + \left(\frac{\partial \rho}{\partial T_a} W_{T_a}\right)^2} \tag{D.5}$$

where the partial derivatives were found by differentiation of Equation **(D.4)** and substituting some typical values.

$$\frac{\partial \rho}{\partial p_a} = \frac{1}{R \cdot T_a} = +0.0000115 \frac{kg/m^3}{Pa}$$

$$\frac{\partial \rho}{\partial T_a} = -\frac{1}{R \cdot T_a{}^2} = -0.0036029 \frac{kg/m^3}{K}$$

$W_p = \pm 33.763 Pa$ (0.01 in. H_g)(readability of mercury barometer)

$W_{T\,a} = \pm 0.56 K (\pm 1^\circ F)$ (least readable thermometer)

Substituting the above values into Equation **(D.5)** resulted in

$$W_\rho = 0.00205 \frac{kg}{m^3}$$

The flow at the inlet of the compressor was assumed to be incompressible and velocities from the Pitot rakes and Pitot-static probes were calculated from the reduced Bernoulli equation

$$V = \sqrt{2(P_t - P_s)/\rho} \tag{4.1}$$

where P_t is inlet total pressure, P_s is inlet static pressure, and ρ is flow density at the inlet.

The uncertainty in velocity calculations is then

$$W_V = \sqrt{\left(\frac{\partial V}{\partial \rho} W_\rho\right)^2 + \left(\frac{\partial V}{\partial P_t} W_{P_t}\right)^2 + \left(\frac{\partial V}{\partial P_s} W_{P_s}\right)^2} \qquad \textbf{(D.13)}$$

and the partial derivatives are

$$\frac{\partial V}{\partial \rho} = -\left(\frac{P_t - P_s}{\rho^2}\right)\left(\frac{2}{\rho}(P_t - P_s)\right)^{-1/2}$$

$$\frac{\partial V}{\partial P_t} = \frac{1}{\rho}\left(\frac{2}{\rho}(P_t - P_s)\right)^{-1/2}$$

$$\frac{\partial V}{\partial P_s} = -\frac{1}{\rho}\left(\frac{2}{\rho}(P_t - P_s)\right)^{-1/2}$$

Typical values of total and static pressure at the inlet were

$$P_t = 2130.98 \frac{lb_f}{ft^2}$$

$$P_s = 2129.95 \frac{lb_f}{ft^2}$$

with a typical flow density at the inlet of

$$\rho = .0736 \frac{lb_m}{ft^3}$$

Evaluating the partial derivatives yields

$$\frac{\partial V}{\partial \rho} = -35.94 \frac{ft/\sec}{lb_m / ft^3}$$

$$\frac{\partial V}{\partial P_t} = 2.57 \frac{ft/\sec}{lb_f \ / \ ft^2}$$

$$\frac{\partial V}{\partial P_s} = -2.57 \frac{ft/\sec}{lb_f \ / \ ft^2}$$

With uncertainty for the density measurement known to be

$$W_\rho = 0.00205 \frac{kg}{m^3} = .0001279 \frac{lb_m}{ft^3}$$

and manufacturer uncertainty for static pressure is

$$W_{P_s} = \pm 0.07052 \text{ lb}_\text{f}/\text{ft}^2$$

The uncertainty in pressure as stated by the manufacturer is ± 0.15 % of the measured value. Recall that all pressures were measured relative to atmospheric. Using a typical total pressure value of – 0.1 inches of water based on the rake Pitot tube lowest within the boundary layer of the inlet, the uncertainty in total pressure at the inlet is

$$W_{P_t} = \pm 0.0007803 \frac{lb_f}{ft^2}$$

Substituting these values into Equation **(D.13)** yields

$$W_V = \pm 0.1813 \frac{ft}{\sec} = \pm 0.0553 \frac{m}{\sec}$$

Assuming this to be the error for the Pitot probe and each of the rake Pitot probes, we can use conservation of mass principles to find the error in the flow coefficient C_x/U_{tip}. Continuity yields

$$\rho V_{inlet} A_{inlet} = \rho V_{ann} A_{ann} \qquad \textbf{(D.14)}$$

Where V_{inlet} and A_{inlet} and V_{ann} and A_{ann} are the flow velocities and areas at the inlet duct and annulus in the plane of the rotor, respectively. Knowing the low Mach number flow to be incompressible results in

$$V_{inlet} A_{inlet} = V_{ann} A_{ann} \tag{D.15}$$

with values of

A_{inlet} = 0.1642 m^2
A_{ann} = 0.085 m^2

Knowing V_{ann} to be equal to the average axial velocity C_x through the blade passage yields the error in the axial flow to be

$$W_{C_x} = \pm 0.3502 \frac{ft}{\sec} = \pm 0.1068 \frac{m}{\sec}$$

With rotor rotational speed held constant at 2100 rpm and a blade tip radius of 0.7492 ft (0.228346 m), the uncertainty in the non-dimensional flow coefficient is

$$W_{C_x / U_{tip}} = 0.002127$$

Rotor performance was obtained using the non-dimensional total pressure rise

$$\Psi = \frac{P_{ann} - P_{atm}}{\frac{\rho \cdot U_{tip}^{2}}{2}} \tag{4.5}$$

In this case, P_{ann} refers to the total pressure downstream of the rotor as measured by a Pitot-static probe. As all pressures were measured relative to atmospheric, uncertainty in atmospheric pressure P_{atm} is ignored. Based on Equation **(4.5)** the uncertainty in ψ is

$$W_{\Psi} = \sqrt{\left(\frac{\partial \Psi}{\partial P_{ann}} W_{P_{ann}}\right)^2 + \left(\frac{\partial \Psi}{\partial \rho} W_{\rho}\right)^2} \tag{D.16}$$

The partial derivatives were found by differentiation of Equation **(3.5)** and substituting some typical values.

$$\frac{\partial \Psi}{\partial P_{ann}} = \frac{1}{\frac{1}{2}\rho U_{tip}^{\ 2}} = 0.0006474 \frac{m^2}{N}$$

$$\frac{\partial \Psi}{\partial \rho} = -\frac{\left(P_{ann} - P_{atm}\right)}{\frac{1}{2}\rho^2 U_{tip}^{\ 2}} = 0.2378 \frac{m^3}{kg}$$

From before,

$$W_{\rho} = 0.00205 \frac{kg}{m^3} = .0001279 \frac{lb_m}{ft^3}$$

and assuming the manufacturer's specifications for $\pm 0.0015\,\%$ uncertainty in total pressure measurements gives

$$W_{P_t} = \pm 0.675 \frac{N}{m^2}$$

Substituting these values into Equation **(D.16)** gives the error in the non-dimensional pressure rise coefficient to be

$$W_{\Psi} = \pm 0.0006547$$

Uncertainty in Steady/Unsteady Rotor Exit Flow Measurements

Rotor exit one-dimensional total pressure measurements were obtained using the piggyback steady/unsteady probe described in Ch. 3. Pressure signals from each of the separate steady and unsteady probes were superimposed to provide dynamic measurements in the wake of the rotor.

The uncertainty for the steady component of the piggyback probe is assumed equal to the unsteadiness of the downstream total pressure probe

$$W_{P_t\,steady} = \pm 0.675 \frac{N}{m^2}$$

According to the manufacturer, the uncertainty due to combined non-linearity and hysteresis in the high-response transducer was ± 0.75 %. With a typical total pressure value of 600 N/m^2 relative to atmospheric, the uncertainty in the unsteady total pressure measurement is

$$W_{P_t\,unsteady} = \pm 4.50 \frac{N}{m^2}$$

Superposing the uncertainties of the steady and unsteady one-dimensional total pressure measurements gives the uncertainty for the total pressure of the combination probe as

$$W_{P_t} = \pm 5.175 \frac{N}{m^2}$$

14 APPENDIX E

Instrumentation/Hardware

Computer/Data Acquisition System

Computer

Gateway P166 laptop

64 MB RAM

4.0 GB hard drive

I/O card

National Instruments DAQCard-AI-16E-4

8 differential channels

12 bit, 1 in 4096 resolution

250 kS/sec maximum sampling rate

1024 sample FIFO buffer size

512 word configuration memory size

800 kHz small signal (-3 dB) bandwidth

400 kHz large signal (1% THD) bandwidth

Board

National Instruments SCB-68

Screw terminals for I/O connections

Shielded enclosure

Compressor Control

Rheostat: General Electric 5748472G130

Drive Motor: General Electric KINEMATIC Direct Current Generator 5CD256G38

Compressor: General Electric Fan Unit 7A5-A1

Pressure Transducers

Datametrics Type 590 Integral Barocel Pressure Transducer

General Specifications:

Pressure Range: 10 inches of H_2O

Power Requirements: 18 to 35 Volts DC or 20 to 33 Volts AC at 75 mA. 50-60 Hz

Output Signal: 0 to ±10 Volts DC, 2 mA into 5 K Ω load, floating (Code-4), zero adjustable ± 0.5 %, span adjustable ± 1.0 %.

Leak Rate to Ambient: Viton-sealed model (Code-V) 5E-7 std cc/sec @ 760 Torr
All-welded model (Code-H) 1E-10 std cc/sec @ 760 Torr

Electrical Fittings: MS3102A-16S-1PZ (One mating connector, MS3106A-16S-1 SZ is supplied with each 590 transducer)

Pressure Fittings: 1/8" – 27 NPT (Code-1) standard

Volume: 5.0 cc per side, with zero differential pressure applied, 0.16 cc diaphram displacement with full range pressure applied

Transient Response: 8 msec (to step input of zero to sensor full pressure range pressure, at 1 atm line pressure, with no external tubulation, measured to 63 % f.s.)

Diaphram Resonant Frequency: 3 kHz (nominal)

Overpressure: 1.5 times sensor full range

Ambient Temperature Range: Storage: -45 °C to + 85 °C
Operating: +5 °C to + 70 °C

Calibration: +10 °C to + 50 °C

Temperature Effects: 30 ppm/°C on zero, 300 ppm/°C on slope

Accuracy (zero-based linearity): ± 0.15 % of reading + 0.01 % f.s.

Repeatability: 0.01 % of reading + 0.005 % of maximum applied pressure

Hysteresis Error: ± 0.001 %

Datametrics Type 1400 Electric Manometer

General Specifications:

Display: 3 ½ digits, update twice per second

Power Requirements: 115 Volts AC, 50-60 Hz, 0.2 A

Outputs: 28 Volts DC, capable of powering up to 6 Barocels and one Type 1402 Barocel Selector, 0 to ± 1 Volts DC pressure signal, BCD DTL/T2L compatable

Controls: Power ON/OFF, Zero and Span adjustment, Range switch with X1 and X0.1 scales, and calibrate position

Ambient Temperature: Operating + 10 °C to + 40 °C, storage –45 °C to + 55 °C
Interconnecting Cables: Type 711-15, 15 feet in length

Entran EP Pressure Transducer

Model EPE-541-2P-/R

Sensitivity: 77.5 mV/psig

Input Impedance: 1062 Ω

Output Impedance: 1041 Ω

Range: 2 psig

Burst Pressure: 46 psig

10.0 Volts excitation, gauge reference

Resonant Frequency: 80 kHz nominal, within ± ½ dB to 5 kHz, ± 5 dB to > 20 kHz

Nonlinearity and Hysteresis: 2P & .13 B: ± 1 ½ %, 5P & .35 B: ± 3/4 %; M: ± ½ dB Amp. Lin.

Entran IMV Amplifier

Model IMV-15/10/100A-WW

Voltage Supply: ± 15 Volts DC

Sensor Excitation: 10 Volts DC

Gain: 100 adjustable ± 10 % min.

Base line: Externally adjustable ± 500 mVolts

Full Range Out (12 Volts max.): 12 Volts with 50 Ω load

Operating Temperature: - 29 °C to + 82 °C

Storage Temperature: -40 °C to 120 °C

- 3 dB Bandwidth (nominal): at 50 gain, 80 kHz typ.; at 100 gain, 70 kHz typ.

Nonlinearity & Hysteresis: ± 0.05 %

Output Current (max.): 50 mA with up to 50 Ω load, 25 mA with 500 Ω load

15 APPENDIX F

This Appendix is taken directly out of the Boller (1998) thesis since it applies to this work as well.

Cubic Spline Interpolation

As cubic spline interpolation was used to obtain the steady five-hold probe inlet data as well as the lines interpolating many plots in this document, a brief introduction to cubic spline techniques is in order. The cubic spline procedure described is that set forth by Drost (1994) and Burden and Faires (1997). Figure F.1 depicts an arbitrary function fitted with a cubic spline. The interpolation involves four constants which empower the interpolant to not only be continuously differentiable on the interval but to have a continuous second derivative on the interval as well. The functions are valid between two specific points and their values and slopes correspond to those of the adjacent functions at the connecting points.

The third order approach creates a set of functions

$$S_j(x) = a_j + b_j(x-x_j) + c_j(x-x_j)^2 + d_j(x-x_j)^3 \qquad \textbf{(F.1)}$$

for the number of points j = 0, 1, …, n-1. Each function $S_j(x)$ is valid for the range x_{j-1} to x_j. Since values $S_{j+1}(x_{j+1}) = S_j(x_{j+1})$ and slopes $S'_{j+1}(x_{j+1}) = S'_j(x_{j+1})$ for each j = 0, 1, …, n-2 it is possible to derive a linear system of equations

$$(x_j - x_{j-1})(c_{j-1}) + 2(x_{j+1} - x_{j-1}) + (x_{j+1} - x_j)(c_{j+1}) = (3/(x_{j+1} - x_j))(a_{j+1} - a_j) - (3/(x_j - x_{j-1}))(a_j - a_{j-1}) \qquad \textbf{(F.2)}$$

for each j = 1, 2, …, n-1. The Drost program **spline.bas** performs a Gauss-Seidel iteration on this linear system to numerically solve for the unknown constants.

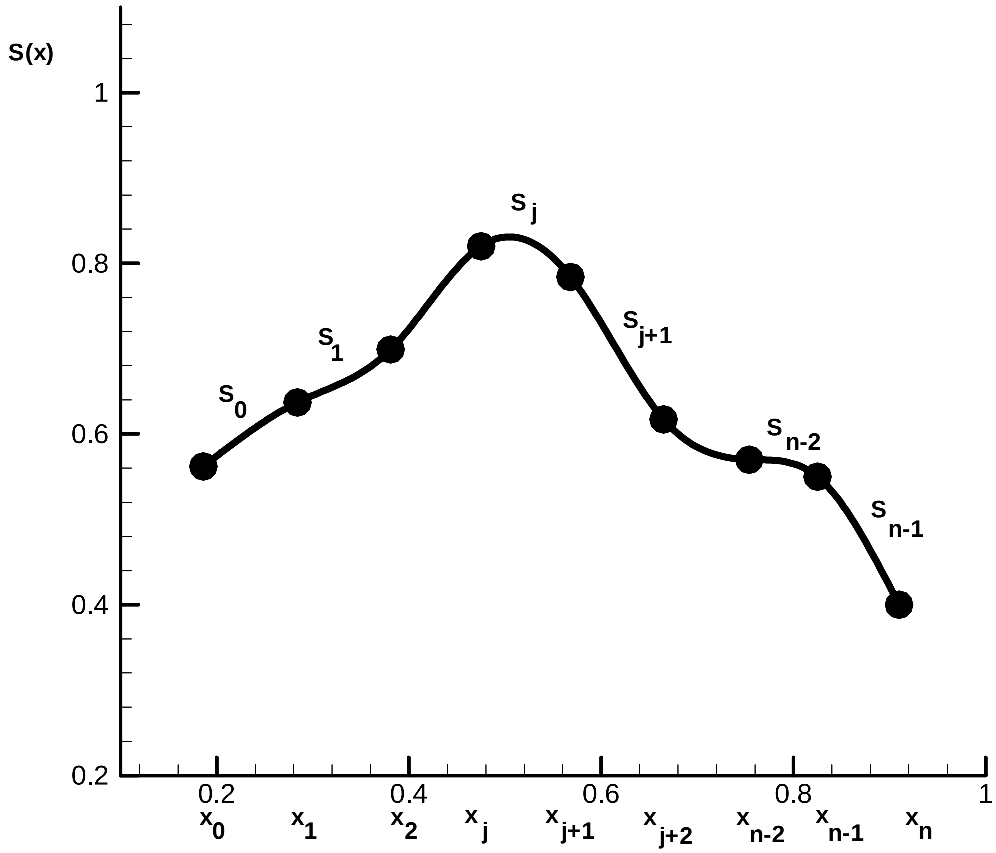

Figure F.1: Graphic of Cubic Spline Interpolation Technique (Boller, 1998)

Vita

The author, Jeffrey R. Schwartz, son of M. Patricia and Roland F. Schwartz, Jr., was born on April 9, 1976 in Baltimore, Maryland. He attended elementary, middle, and high school in Bel Air, MD. He attended Virginia Tech as an undergraduate where he was a member of the Men's Volleyball team, while studying mechanical engineering. He graduated Magna Cum Laude in May 1998 receiving his Bachelor of Science degree in mechanical engineering. Over those four summers, he worked at AAI Corporation in Hunt Valley, MD in the Electro-Mechanical Department. He is a member of Tau Beta Pi, ASME, and AIAA. He is registered Engineer-in-Training in the state of Virginia. Upon graduation, he will begin working for Northrup Grumman (ESSS), Oceanic Systems Division in Annapolis, MD as a mechanical design engineer.